The direct scattering study of the parametrically driven nonlinear Schrödinger equation

Carel Petrus Olivier

Dissertation presented for the degree of Doctor of Philosophy at the

Department of Mathematics and Applied Mathematics

University of Cape Town

February 2013

Supervisor: Dr. N. A. Alexeeva

Plagiarism declaration

I know the meaning of plagiarism and declare that all of the work in the dissertation, save for that which is properly acknowledged, is my own

Signed:

Date:

Declaration of Free License

I hereby:

(a) grant the University free license to reproduce the above thesis in whole or in part, for the purpose of research;

(b) declare that:

(i) the above thesis is my own unaided work, both in conception and execution, and that apart from the normal guidance from my supervisor, I have received no assistance except as stated below;

(ii) neither the substance nor any part of the thesis has been submitted in the past, or is being, or is to be submitted for a degree at this University or any other University, except as stated below.

I am now presenting the thesis for examination for the Degree of PhD.

Abstract

The term "direct scattering study" refers to a numerical tool used to analyze solitons in non-integrable equations. The direct scattering study amounts to the calculation and analysis of the discrete eigenvalues of the Zakharov-Shabat (ZS) eigenvalue problem. For this purpose, a fast and accurate numerical method is of paramount importance. Hill's method is an elegant numerical scheme that combines Fourier theory, Floquet theory and Hill's equation, and can be used to calculate the spectrum of the ZS eigenvalue problem for periodic potentials. In order to study decaying potentials defined on the entire real line we analyzed the limit of the period $L \to \infty$. Numerical results revealed an optimal choice of the Floquet exponent that ensures accurate results with no spurious eigenvalues. The reduction of Hill's method to a single Floquet exponent also results in a much faster calculation of the discrete spectrum of the ZS eigenvalue problem.

The direct scattering study was applied to time-dependent oscillating solitons that arise as attractors in the parametrically driven nonlinear Schrödinger equation. The driving strength and damping coefficient were treated as parameters. We identified four different types of attractors within the parameter space, each with a unique soliton content. The different types of attractors are the result of larger radiation emissions that are associated with larger driving strengths. The soliton content was also used to study the impact of the period-doubling route to temporally chaotic soliton attractors. We showed that the increase in driving strength responsible for the period-doubling bifurcations weakens the energy of the soliton. This weakening effect may be responsible for the loss of stability of the oscillating

soliton associated with increased driving strengths.

In the small damping regime the zero attractor occupies a large part of the parameter space. The oscillating solitons appear as transients in this region. The direct scattering study revealed that the radiation emissions of the soliton transients increase when the driving strength is increased. This indicates that increased driving sustains the soliton transient, and that larger radiation emissions are necessary to destabilize the soliton. In some cases increased driving can lead to the restabilization of the oscillating soliton, although it mostly leads to the formation of spatio-temporal chaos.

Excessive driving strengths lead to the formation of spatio-temporal chaos for any damping coefficient. Oscillating solitons also appear as transients in the spatio-temporally chaotic region of the parameter space. The direct scattering study revealed that radiation plays an essential role in the formation of spatio-temporal chaos. The way in which the radiation leads to chaos depends on the damping regime. For smaller damping coefficients a solitary radiation wave can become unstable due to the driving strength. For larger damping coefficients an unstable radiation tail are formed from radiation waves that is emitted over a large period of time.

Contents

Acknowledgements

I am grateful for the wonderful support of so many people during my studies. I firstly want to thank my Creator for His grace, goodness and provision. I am greatly indebted to my supervisor, Dr. Nora Alexeeva, for her enthusiasm, helpfulness and patience throughout this project. I particularly want to thank her for fast and diligent corrections to earlier drafts of the thesis. I want to thank UCT's High Performance Computing Team, and particularly Andrew Lewis for providing excellent service and support. I am grateful to Prof. Igor Barashenkov who supported me since the beginning of my Master's degree. I also want to thank Prof. Ben Herbst and Dr. Maxim Molchan for many fruitful discussions.

I want to thank my parents for their unyielding love and support. Your example of goodness, honesty and integrity has been a guiding light throughout my life. I particularly want to thank my mother for hours of proofreading. I want to thank Zaria for bringing much-needed balance to my life, and whose music always served as inspiration. I also want to thank her parents for their hospitality and many delicious meals.

I want to thank the National Institute of Theoretical Physics (NITheP) for providing funding, and the UCT Postgraduate Funding Office for partial financial support.

Chapter 1

Introduction

The parametrically driven nonlinear Schrödinger (PDNLS) equation describes resonant phenomena in a large variety of physical systems, including nonlinear Faraday resonance in oscillating water tanks [74, 104, 106], spin waves in easy-plane ferromagnets [15, 33, 112], parametric amplification of light pulses in optical fibers [42, 66, 72, 76, 86, 89, 92] and mechanical resonators in microelectromechanical and nanoelectromechanical systems [59, 95]. A remarkable aspect of the PDNLS equation is that fact that it admits a large class of soliton solutions [15, 16, 18, 75].

Solitons are localized waves that propagate through nonlinear media with a constant velocity while maintaining their shape. The development of the inverse scattering transform (IST) method [4, 46, 113] resulted in the development of soliton theory that describes the role of solitons in the dynamics of integrable equation. Numerical calculations played an important role in the development of soliton theory [43, 111], and remain an indispensible tool in contemporary studies of solitons. In order to keep up with the growing computational demands of solitons, it is important that the accuracy and efficiency of numerical methods are improved. The improvement of numerical techniques is one of the aims of the present thesis.

Another central theme of the thesis is the interaction between solitons and radiation.

Radiation arises in the form of dispersive wave trains with small amplitudes. In idealized conditions, solitons are unaffected by interactions with radiation. However, when other factors such as higher-order nonlinearities, nonlocalities, external driving and dissipation are taken into account, these interactions play a crucial role in soliton dynamics. While our study is concentrated on the PDNLS equation, our methods can be applied more generally to investigate the interaction between solitons and radiation in non-integrable equations.

1.1 Development of soliton theory

Solitons were first reported by John Scott Russell [88] in 1844. The circumstances of the discovery are best described in his own words:

> "I was observing the motion of a boat which was rapidly drawn along a narrow channel by a pair of horses, when the boat suddenly stopped - not so the mass of water in the channel which it had put in motion; it accumulated round the prow of the vessel in a state of violent agitation, then suddenly leaving it behind rolled forward with great velocity, assuming the form of a large solitary elevation, a rounded, smooth and well-defined heap of water, which continued its course along the channel apparently without change of form or diminution of speed. I followed it on horseback, and overtook it still rolling on at a rate of some eight or nine miles an hour, preserving its original figure some thirty feet long and a foot to a foot and a half in height. Its height gradually diminished, and after a chase of one or two miles I lost it in the windings of the channel. Such, in the month of August 1834, was my first chance interview with that singular and beautiful phenomenon which I have called the Wave of Translation, ..."

At the time Russell's "Wave of Translation", later called a solitary wave, contradicted the shallow-water wave theory of Airy [10], as was pointed out by Stokes [93] in 1847. However Russell was adamant to prove the existence of these waves, leading him to generate solitary

waves in water tank experiments. It was left to Boussinesq [27] and Rayleigh [87] to resolve this issue in the 1870's. They showed that the combination of dispersion and nonlinearity can lead to the formation of solitary waves. Prior to this, the models for shallow water waves ignored the effects of dispersion. In 1895 Korteweg and De Vries [63] derived a model for shallow water waves that combines dispersion and nonlinearity. Their model, known as the Korteweg-deVries (KdV) equation, admits solitary wave solutions that fit the description of Russell's solitary waves.

During the sixty years that followed the derivation of the KdV equation, interest in the study of solitary waves faded. Solitary waves may have been regarded as a rare occurence, restricted to shallow water waves. However, an unexpected result reported by Fermi, Pasta and Ulam [43] in 1955 renewed interest in the subject. They conducted an experiment of heat transfer in a lattice, consisting of uniform masses that are connected with nonlinear springs. They expected the heat energy to spread evenly across all modes of the lattice. To their surprise the energy spread only to a few nearby modes. More surprising was the fact that the majority of the energy returned to the originally excited mode periodically. They confirmed this near recurrence through numerical simulations. Zabusky and Kruskal studied the same heat conduction problem by using a continuum approximation, resulting in the KdV equation. Using numerical simulations, they found that the solitary waves pass through each other without alteration of the speed or shape. They called these waves *solitons* to emphasize the fact that these special solitary waves have photon-like collision properties.

In 1967 Gardner, Greene, Kruskal and Miura [46] developed an analytical method to solve the KdV equation analytically. Their method, the inverse scattering transform (IST) method, was used to show that any initial disturbance results in the formation of solitons accompanied by a dispersive radiation tail. This discovery marked the birth of soliton theory. In 1968 Lax [65] introduced an elegant reformulation of the IST method. He showed that the KdV equation arises as the compatibility condition of two linear operators, commonly referred to as the Lax pair. The idea of the Lax pair was used by Zakharov and Shabat [113]

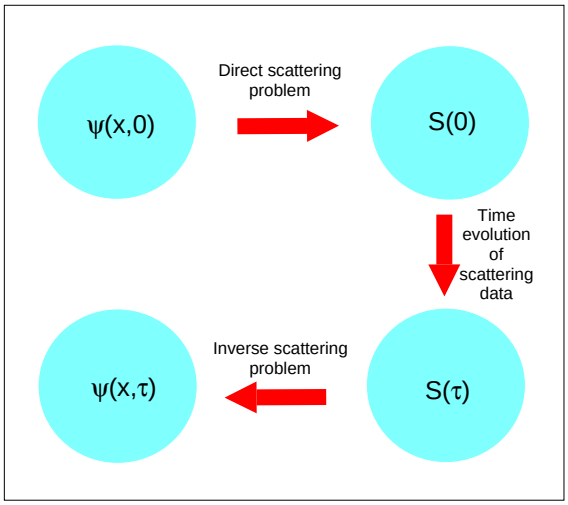

Figure 1.1: *Schematic representation of the inverse scattering transform method.*

to extend the inverse scattering transform method to solve the nonlinear Schrödinger (NLS) equation in 1971. In 1972 Wadati [101] showed that the IST method can also be used to solve the modified Korteweg-deVries (mKdV) equation. In 1973 Ablowitz Kaup Newell and Segur (AKNS) [3] extended the IST method to solve the sine-Gordon (SG) equation. A year later the same authors [4] developed a method to generate a class of integrable equation, known as the AKNS hierarchy, that can be solved through the IST method. The AKNS hierarchy includes the KdV, NLS, SG, mKdV and the sinh-Gordon equations.

1.2 The soliton content

The concept of the soliton content is rooted within the framework of the inverse scattering transform method. The inverse scattering transform method is a typical transformation method, similar to Fourier and Laplace transform methods for linear equations. This was recognized by Ablowitz, Kaup, Newell and Segur in 1974 [4] with their paper entitled "The Inverse Scattering Transform–Fourier Analysis for Nonlinear Problems". The idea behind any transformation method is to transform an initial condition into a space where the time

dependence is simple. One can therefore easily calculate the time evolution of the transformed data. The inverse transform is then applied to reconstruct the solution at this later time. In Figure 1.1 we show a schematic representation of the inverse scattering transform method. Here $\psi(x,0)$ represents the initial condition. The first step (indicated $\rightarrow$ in the schematic representation) is to transform the initial condition onto the so-called scattering data, $S(0)$. The scattering data is defined in terms of the Zakharov-Shabat eigenvalue problem. This step is usually referred to as *the direct scattering problem.* The second step (indicated $\downarrow$ in the schematic representation) is the calculation of the scattering data at $t = \tau$. If the equation is integrable, the time evolution of the scattering data is trivial thanks to the existence of the Lax pair. The third step (indicated $\leftarrow$ in the schematic representation) is to reconstruct the solution $\psi(x,\tau)$ from the scattering data $S(\tau)$, using the inverse transformation. This is usually referred to as *the inverse scattering problem.*

The range of initial value problems that can be solved by the inverse scattering transform method is limited. Although the IST can theoretically solve any initial value problem for integrable equations, it can only solve a limited class of initial value problems in practice. The reason for this is the difficulty of solving the direct and inverse scattering problems. Solutions can be obtained for pure solitons, i.e. solutions with zero radiation. Even in the case of reflectionless potentials that contain a large number of solitons, the IST becomes so complicated that other methods were developed to find analytical expressions for these solutions, including Hirota's method [51, 52, 53, 54] and Darboux transformations [79]. Important exceptions are solutions obtained by Satsuma and Yajima in 1974 [90] for a class of sech initial conditions of the NLS equation. This class of solutions, in general, contains radiation. To this day, analytical solutions can only be found for special initial conditions, and for more general initial conditions, the analytical solutions are intractable. For this reason, computer simulation and analysis remain of paramount importance in current studies of soliton theory.

Due to the complexity of the IST method, many attempts were made to simplify the problem. One way to do this is by studying only the soliton content. The soliton content forms

part of the scattering data, and reveals the number, structure and physical characteristics of solitons that form during the time evolution of the initial disturbance. In the integrable case, the soliton content is time independent. This reflects the fact that no solitons are formed, destroyed or altered as a result of collisions between solitons. Therefore, by solving the direct scattering problem only partially, one can obtain important information about the resulting solution.

1.3 Adiabatic analysis

The integrable equations of the AKNS hierarchy are idealized models that serve only as approximations to many natural phenomena. This idealization is reflected by the fact that solutions to these equations obey an infinite number of conservation laws. Integrability is very fragile, and the smallest perturbations destroy the integrability. Many of these perturbations arise in physical problems, and include dissipative effects, external driving, non-local effects and higher-order nonlinearities. A detailed description of these so-called near-integrable equations is described in a comprehensive review by Kivshar and Malomed [60] in 1989. They show that solitons are observed in many near-integrable equations, and that these solitons don't share the same properties as their integrable counterparts. For example, in most cases collisions between near-integrable solitons are inelastic, resulting in the formation of radiation, the formation of breathers or even the destruction of solitons. Indeed unstable soliton solutions are frequently encountered in near-integrable equations. Although these solutions clearly don't satisfy the "indestructible" criteria of Zabusky and Kruskal's original definition, the term "soliton" is widely used to define these spatially localized waves.

Soon after the development of soliton theory, it was realized that the inverse scattering transform method can be used to study the effect of perturbations on solitons. In 1977 Kaup [57] introduced the adiabatic analysis, an analytical method to study solitons in near-integrable equations. Adiabatic analysis is a perturbation method that estimates the time

evolution of the soliton content. This in turn allows one to study the effect of a perturbation on the time evolution of solitons. Kaup used this approach to show that any soliton in the NLS equation is destroyed after a sufficiently large time when a small damping perturbation is introduced. His method was applied to a large number of equations. However, there are some restrictions to the use of adiabatic analysis, namely *1)* the method ignores the effect of radiation, *2)* the method only applies to small perturbations of integrable equations and *3)* adiabatic analysis can only be applied to solutions that are solvable via the IST method. The first of these restrictions can be resolved by including higher-order terms of the perturbation method, resulting in the perturbed inverse scattering method (see for example Malomed [69] and Kivshar and Malomed [60]) that allows one to also study the effect of the perturbations on radiation. However, restrictions *2)* and *3)* are not improved by this method.

1.4 The direct scattering study

An alternative method that forms the main theme of this thesis is the direct scattering study. The direct scattering study amounts to the calculation and analysis of the soliton content. This method is, in essence, a numerical version of adiabatic analysis. However, the main difference between the methods is that the adiabatic analysis is used to determine the time evolution of the soliton. In the direct scattering study, the behaviour of the soliton is simulated numerically prior to the application of the direct scattering study. Therefore the goal of the direct scattering study is to analyze the soliton. An important advantage of the direct scattering study is that the soliton content can be used to calculate the distribution of energy between solitons and radiation. Therefore the direct scattering study gives some information about the radiation, whereas adiabatic analysis considers only the characteristics of the solitons.

The direct scattering study was first applied in 1986. Overman developed a code, based on Floquet theory, to calculate the soliton spectrum of the sine-Gordon equation with periodic

boundary conditions. The code was used by himself and coworkers [82] to study chaos in a damped-driven sine-Gordon equation. The direct scattering study was also used by Ablowitz and coworkers [2, 50] to investigate numerical chaos in the NLS equation. The soliton content was used to reveal the source of the chaos as so-called homoclinic crossings, the result of numerically-induced perturbations that destroy the integrability.

The numerical method for the direct scattering study was later extended to potentials defined on the real line. In 1992 Boffetta and Osborne [22] proposed a shooting method for the calculation of the soliton content of the NLS equation for potentials defined on the real line. In the context of potentials defined on the real line, the direct scattering study is useful for studies of the perturbed and unperturbed NLS equation. For the latter case, the soliton content is useful for studying the generation of solitons, while in the former it is used in the study of the influence of perturbations on solitons in near-integrable systems.

The generation of solitons in the unperturbed NLS remains an important field of study, especially in the field of nonlinear optics. In 1994 Burak and coworkers [29] studied the generation of solitons from Gaussian initial conditions. In 2001 Klaus and Shaw [61] used the direct scattering study to investigate the effect of chirping on soliton generation. In the same publication the authors reported the generation of moving solitons from real potentials, which in turn led them to the formulation and proof of the single lobe theorem in 2002 [62] that gives conditions for the generation of stationary solitons. In the same year Panoiu and coworkers [83] used the direct scattering study to investigate the generation of solitons through a superposition of solitons with different frequencies. In 2008 the direct scattering study was applied by Tsoy and De Sterke [98] to study the effect of amplitude-only and phase-only filters on solitons in optic systems. In 2012 Derevyanko and Small [39] used the direct scattering study to analyze disordered optical fields propagating in nonlinear bulk waveguides.

The direct scattering study is particularly useful in the study of solitons in perturbed NLS systems. This application of the direct scattering study forms the main topic of the thesis.

This method was applied to study the effects of a large variety of perturbations on single solitons, including periodic amplifiers [73], higher-order dissipation combined with linear gain [100], different amplifiers, phase modulators and filters [84]. The direct scattering study was also applied to study the effect of numerous perturbations on soliton complexes, known as breathers. These perturbations include linear damping [23, 85], quintic nonlinearities [14], intrapluse Raman scattering and third-order dispersion [48, 84], variation of the transverse linear refractive index [94] and a symmetric harmonic trap [21].

The calculation of the soliton content amounts to the calculation of the discrete spectrum of a linear operator, known as the Zakharov-Shabat eigenvalue problem. The numerical study of the spectrum of linear operators has received much attention recently, due to its importance in linear stability analysis. A particularly useful scheme is the Hill's method, an efficient scheme that combines Floquet and Fourier theory to solve Hill's equation. Deconinck and Kutz [38] proposed this method to calculate the soliton content of the KdV equation. The author, along with Herbst and Molchan [81], proposed a refinement of the method for the calculation of the soliton content of the NLS equation. The method not only reduces the computation time, but also allows accurate calculation of discrete eigenvalues near the continuous spectrum.

1.5 The parametrically driven nonlinear Schrödinger equation

In this thesis we consider the parametrically driven nonlinear Schrödinger (PDNLS) equation, given by

$$i\psi_t + \psi_{xx} + 2\left|\psi\right|^2\psi = \psi + h\psi^* - i\gamma\psi \tag{1.1}$$

The left hand side of this equation describes the motion of waves in dispersive media with weakly nonlinearity. The right hand side of the equation describes the effects of dissipation

and external time-periodic driving. The strength of the damping and driving is given by $\gamma > 0$ and $h > 0$ respectively.

The PDNLS equation describes resonant phenomena in a large variety of physical systems. The equation was first derived by Kaup and Newell [58] in 1978 as a model describing dipolar excitations in one-dimensional condensates. In 1984 Miles [75] used the PDNLS equation to model Faraday resonance that was reported earlier that year [74, 108] in hydrodynamic systems, and has since been used by Wang, Wei and coworkers [102, 103, 104, 105, 106, 115] to study waves in vertically oscillating water troughs. In 1991 Barashenkov and coworkers [15] derived the PDNLS equation as a model for breathers in easy-plane ferromagnets, based on the model Zakharov and coworkers [112] derived in 1974. The same model was applied recently by Clerc, Coulibaly, Laroze and coworkers [33, 34, 35, 99] in the context of easy-plane ferromagnets. Since then it was derived in a large variety of physical systems, including parametric amplification of light pulses in optical fibers [42, 66, 72, 76, 86, 89, 92], mechanical resonators in microelectromechanical and nanoelectromechanical systems [59, 95], and many more physical contexts (see for example [18, 20] and the references therein).

An important property of the PDNLS equation is it admits soliton solutions. This is due to the fact that the parametric driving can compensate for energy losses associated with the dissipation. Kaup and Newell [58] were first to investigate solitons in the PDNLS equation. They used the perturbed inverse scattering technique to show that phase-locking can lead to stable breathers, provided that the driving strength is sufficiently large. Miles [75] reported two time-independent solitons $\psi^{\pm}$ that arise when the driving strength is sufficiently large. Barashenkov and coworkers [15] studied the stability of these solitons. They found that the ψ^{-} soliton is unstable for any choice of damping and driving strenghts γ and h respectively, while the ψ^{+} soliton has a stable region in the parameter space.

The attractors of the unstable ψ^{+} solution form the basis of our study of the PDNLS equation. These attractors arise whenever the ψ^{+} soliton is unstable. Attractors are defined

in terms of heteroclinic orbits $\psi_{het}(x,t)$ satisfying

$$\lim_{t\to-\infty}\psi_{het}(x,t) = \psi^{+}(x). \tag{1.2}$$

The attractor $\psi_a(x,t)$ is defined in terms of the asymptotic behaviour of the heteroclinic orbit, given by

$$\psi_a(x,t) := \lim_{t\to\infty}\psi_{het}(x,t). \tag{1.3}$$

Bondila and coworkers [25] did a study of the attractors of the ψ^{+} soliton. They calculated attractors numerically by means of direct simulation. They reported a large number of time-periodic or quasiperiodic oscillating solitons (also sometimes called breathers) that arise as attractors. The report also indicated a period-doubling route to temporal chaos within the region of oscillating soliton attractors. The oscillating soliton attractors of the ψ^{+} soliton form the basis of our study of the PDNLS equation. These attractors consist of a soliton part and radiation waves. The soliton part consists of a single quiescent soliton that oscillates temporally. During these oscillations the soliton emits radiation waves that move away from the soliton. The attractors arise as the result of a balance between energy lost through the dissipative radiation waves and energy pumped into the soliton through the parametric driving.

The purpose of the thesis is to inverstigate the influence of damping and driving on *1)* the spatial characteristics of the soliton part of the attractor and *2)* the energy of the radiation emissions. This is done through the application of the direct scattering study. In order to apply the direct scattering study, one has to generate the attractors numerically. This is done through direct simulation, the same method employed by Bondila and coworkers [25]. The advantage of direct simulation is its ability to generate temporally chaotic attractors and soliton transients. The transients give insight into the transition from soliton attractors to other attractors that happens when, for example, the driving strength is increased or decreased within a specific damping regime.

Another way of generating stable and unstable solitons is through a combination of fixed-point iteration and numerical continuation. This method can also be used to calculate soliton complexes. Time-independent soliton complexes were reported by Barashenkov and Zemlyanaya [16] in 1999. Zemlyanaya and Alexeeva [114] reported time-periodic soliton complexes generated and analyzed numerically. In a series of papers, Barashenkov, Zemlyanaya, Alexeeva and Van Heerden [13, 18, 20, 114] analyzed these soliton complexes and calculated the attractor chart of stable soliton complexes. Although the soliton content of these complexes is still unknown, its study lies beyond the scope of this thesis.

1.6 Structure of the thesis

The thesis is structured as follows: In Chapter 2 we give a brief outline of the inverse scattering transform method for the focusing NLS equation. In order to apply the direct scattering study, one needs a good intuitive understanding of the IST method. The IST method is used to define the soliton content. We put special emphasis on the relationship between the soliton content and the characteristics of the associated solitons. We also give an example of the adiabatic analysis of the damped NLS equation.

Chapters 3 and 4 are dedicated to the numerical schemes used to analyze the PDNLS equation. A significant contribution of this thesis is the development of an efficient way to calculate the soliton content of the NLS equation. In Chapter 3 we derive our method that was reported in [81] that consists of a refinement of Hill's method, based on an optimal choice of the Floquet exponent. We show many examples to illustrate the advantages and accuracy of this choice.

In Chapter 4 we derive the fourth-order split-step method, the numerical method used to simulate solitons of the PDNLS equation, based on the algorithm of Neri [78]. We also demonstrate that the computational speed of the fourth-order split-step method compares favourably to that of the pseudo-spectral Runge-Kutta method, a method which is equivalent

to the former in terms of accuracy.

Chapters 5 and 6 are devoted to the study of the attractors of the PDNLS equation. Chapter 5 is dedicated to the description of the soliton attractors reported by Bondila and coworkers. We look at the influence of damping and driving on the characteristics of the soliton attractors. These results were obtained by inspection of the solutions. Although these results are not new, they represent the most comprehensive description of the soliton attractors to date. It also forms the basis for the direct scattering study.

The direct scattering study of the PDNLS equation constitutes the main result of this thesis, and is performed in Chapter 6. The chapter starts with a description of the direct scattering study, and reviews the relevant relationships between the soliton content and the associated solitons. Once this is established, we study the soliton content of the oscillating soliton attractors. We use the soliton content to classify four types of attractors based on the soliton content. We also show that the soliton content reflects the properties of the soliton attractors, discussed in Chapter 5. We then turn our attention to the transition from soliton attractors to the zero attractor, resulting from an increase in driving strength. This is done in two ways. Firstly, we consider the effect of period-doubling on the associated soliton. We also look at the effect it has on radiation emissions, and use this to show that the period-doubling route to chaos may act as a catalyst for the destabilization of the soliton attractor. The second way we analyze the zero attractor region is to study the soliton transients that arise in the zero attractor region. The soliton content reveals that these transients behave the same as the soliton attractors. Finally we study the transition from soliton attractors to spatio-temporal chaotic attractors. In particular, we use the direct scattering study to show the role of radiation in the formation of spatio-temporal chaos. We show that the formation of breathers play an essential role in the transition to spatio-temporal chaos.

Chapter 2

The inverse scattering transform method

The most important mathematical property of the NLS equation is the fact that it is integrable. As a result, the NLS equation has infinitely many conservation laws, as well as large classes of soliton solutions with elastic collision properties. More importantly, the NLS equation can be solved for an arbitrary initial condition through the inverse scattering method (IST).

In this chapter, we treat the integrable NLS equation analytically. We give a brief outline of the IST, first applied to the NLS equation by Zakharov and Shabat [113]. The main purpose of the chapter is to demonstrate that the ideas of the IST can be used to analyze any solution by finding the so-called "soliton content" from the initial condition. The soliton content can be used to determine the number of solitons that will emerge from any given initial condition. In addition, the soliton content reveals the amplitude and velocity of each soliton.

The chapter is structured as follows: In Section 2.1 we discuss the Lax pair of the NLS equation. Its existence ensures that the NLS equation is integrable. Moreover, the transformations of the IST are defined in terms of the ZS eigenvalue problem that forms part of the Lax pair. In Section 2.2 we consider the properties of the Zakharov-Shabat (ZS) eigenvalue problem. The spectral structure of the ZS eigenvalue problem forms the basis of the IST.

In Section 2.3 we give a brief outline of the IST. The derivation of the formulas is left out. There are, however, many books dedicated to the topic, for example [7, 8, 80]. In Section 2.4 we discuss the conservation laws of the NLS equation. In Section 2.5 we analyze the IST and show the relationship between solitons and the scattering data. We show that all solutions of the NLS equation consist of two ingredients, namely solitons and radiation. This serves as motivation for defining the soliton content of a solution. In Section 2.6 we discuss the perturbed IST method. This method relies on the techniques of the IST to analyze near-integrable partial differential equations.

2.1 The Lax pair

The IST was first applied to the Korteweg-de Vries (KdV) equation by Gardner, Greene, Kruskal and Muira in 1967 [46]. Lax introduced the Lax pair formulation of the IST in 1968 [65]. His approach helped Zakharov and Shabat to generalize the method to the NLS equation [113]. It also helped Ablowitz, Kaup, Newell and Segur to apply the IST to other nonlinear integrable equations, such as the sine-Gordon equation [3, 4].

To define the Lax pair, consider two linear operators L and M, where L is the operator of an eigenvalue problem

$$L\mathbf{v} = \lambda\mathbf{v}, \tag{2.1}$$

and M is the operator of an associated time evolution equation

$$\mathbf{v}_t = M\mathbf{v}. \tag{2.2}$$

If the compatibility condition between (2.1) and (2.2) produces a nonlinear evolution equation, the pair L and M is called the Lax pair of that nonlinear evolution equation.

For the focusing nonlinear Schrödinger equation, defined as

$$iq_t + q_{xx} + 2|q|^2 q = 0, \tag{2.3}$$

the Lax pair was first reported by Zakharov and Shabat [113]. They showed that (2.3) arises as the compatibility condition between

$$\begin{aligned} v_{1x} &= -i\zeta v_1 + q v_2 \\ v_{2x} &= -q^* v_1 + i\zeta v_2 \end{aligned}, \tag{2.4}$$

and

$$\begin{aligned} v_{1t} &= i\left(|q|^2 - 2\zeta^2\right) v_1 + \left(2\zeta q + i q_x\right) v_2 \\ v_{2t} &= \left(2\zeta q^* - i q_x^*\right) v_1 - i\left(|q|^2 - 2\zeta^2\right) v_2 \end{aligned}, \tag{2.5}$$

where the eigenvalue $\zeta \in \mathbb{C}$ is constant in time. As a result, the NLS equation is integrable, and can be solved by the inverse scattering transform method. The eigenvalue problem (2.4) is known as the Zakharov-Shabat (ZS) eigenvalue problem.

2.2 Spectral properties of the ZS eigenvalue problem

The spectrum of the ZS eigenvalue problem (2.4) consists of a continuous set and a discrete set. The continuous spectrum is defined as the dense set

$$\sigma_c = \{\zeta \in \mathbb{C} \text{ a dense point, } |\mathbf{v}(x,\zeta) \text{ is bounded for all } x\}, \tag{2.6}$$

and the discrete spectrum is defined as

$$\sigma_d = \left\{\zeta \,\middle|\, |\mathbf{v}(x,\zeta)| \to 0 \text{ as } |x| \to \infty\right\}, \tag{2.7}$$

where $\mathbf{v}(x,\zeta) = [v_1(x,\zeta), v_2(x,\zeta)]^T$. We restrict ourselves to (2.4) where $|q|$ vanishes sufficiently fast as $|x| \to \infty$. It is sufficient to restrict ourselves to the case where q is square integrable, i.e. $q \in \mathbb{L}^2$.

Before we discuss the spectrum of the ZS eigenvalue problem, it is important to develop some of its basic properties. It follows directly from the ZS eigenvalue that, if $\begin{bmatrix} v_1(x,\zeta) & v_2(x,\zeta) \end{bmatrix}^T$ satisfies the ZS eigenvalue problem (2.4), then $\begin{bmatrix} v_2^*(x,\zeta^*) & -v_1(x,\zeta^*) \end{bmatrix}^T$ also satisfies the ZS eigenvalue problem. From this symmetry it follows that $\zeta \in \sigma_d$ implies $\zeta^* \in \sigma_d$. Therefore it is sufficient to consider only the upper half of the complex plane for the spectral problem.

Since both sets of spectra are defined in terms of the asymptotic behaviour of $\mathbf{v}$, the fact that q vanishes when $|x|$ approaches infinity is significant. Indeed, as $|x| \to \infty$ the ZS eigenvalue problem reduces to

$$\begin{aligned} v_{1x} &= -i\zeta v_1 \\ v_{2x} &= i\zeta v_2 \end{aligned}.$$

From this, the following solutions are readily obtained:

$$\begin{aligned} \phi &\sim \begin{pmatrix} 1 \\ 0 \end{pmatrix} e^{-i\zeta x} & \psi &\sim \begin{pmatrix} 1 \\ 0 \end{pmatrix} e^{-i\zeta x} \\ & \text{as } x \to -\infty, & & \text{as } x \to \infty. \\ \bar{\phi} &\sim \begin{pmatrix} 0 \\ 1 \end{pmatrix} e^{i\zeta x} & \bar{\psi} &\sim \begin{pmatrix} 0 \\ 1 \end{pmatrix} e^{i\zeta x} \end{aligned} \tag{2.8}$$

These functions are called the Jost eigenfunctions. Since the Wronskians of the functions, $W\left(\phi, \bar{\phi}\right) = W\left(\bar{\psi}, \psi\right) = 1$, are nonzero, it follows that both sets $\left\{\phi; \bar{\phi}\right\}$ and $\left\{\psi; \bar{\psi}\right\}$ are bases for the ZS eigenvalue problem. Therefore one can express any solution as a linear combination of these bases. We can also express the function ϕ as a linear combination of ψ and $\bar{\psi}$, leading

to the scattering equation

$$\phi(x,\zeta) = b(\zeta)\,\psi(x,\zeta) + a(\zeta)\,\bar{\psi}(x,\zeta), \tag{2.9}$$

for complex functions $a(\zeta)$ and $b(\zeta)$. The symmetry of the eigenfunctions implies that

$$\bar{\phi} = \begin{pmatrix} -\phi_2^*(x,\zeta^*) \\ \\ \phi_1^*(x,\zeta^*) \end{pmatrix}, \qquad \bar{\psi} = \begin{pmatrix} \psi_2^*(x,\zeta^*) \\ \\ -\psi_1^*(x,\zeta^*) \end{pmatrix},$$

where $\phi = [\phi_1, \phi_2]^T$ and $\psi = [\psi_1, \psi_2]^T$.

The properties discussed above allow us to describe the sets of spectra (2.6) and (2.7) in more detail. It follows from the Jost eigenfunctions (2.8) that, for any real value of ζ, the function $\mathbf{v}$ is bounded. Therefore the continuous spectrum consists of the entire real line, i.e. $\sigma_c \equiv \mathbb{R}$. Note that this holds for any q that decays sufficiently fast. It is well known that the Jost eigenfunctions ϕ and ψ, and the function $a(\zeta)$ can be analytically continued into the upper half of the complex plane [8]. From the scattering equation (2.9) it follows that discrete eigenvalues in the upper half of the complex plane satisfies $a(\zeta) = 0$. The analyticity of the function $a(\zeta)$ ensures that discrete eigenvalues are isolated. The rapid decay of the potential $q(x) \in L^2$ as $|x|$ approaches infinity ensures that there are only a finite number of discrete eigenvalues.

In what follows, we show the main steps of the inverse scattering transform method. It is important to notice the fundamental role of the ZS eigenvalue problem in this method.

2.3 Outline of the IST

The scattering data are defined in terms of the spectrum of the ZS eigenvalue problem, σ_c and σ_d, and the associated eigenfunctions. It is defined as follows:

$$S(t) = \{\zeta_1, \cdots, \zeta_N, C_1, \cdots, C_N, \rho(\xi)\}. \tag{2.10}$$

Here $\zeta_1, \cdots, \zeta_N$ are the N discrete eigenvalues. The complex numbers $C_1, \cdots, C_N$ are the normalisation constants, defined in terms of the discrete eigenfunctions:

$$\phi(x, \zeta_j) = C_j \psi(x, \zeta_j). \tag{2.11}$$

Finally, the reflection coefficient $\rho(\xi)$ is defined in terms of the eigenfunctions corresponding to the continuous spectrum as

$$\rho(\xi) = \frac{b(\xi)}{a(\xi)} \text{ for } \xi \in \mathbb{R}. \tag{2.12}$$

The IST consists of three steps. The first step, the direct scattering problem, maps the initial potential $q(x, 0)$ onto the initial scattering data $S(0)$. The second step calculates the time evolution of the scattering data, that is, finds $S(t)$ from $S(0)$. The final step, the inverse scattering problem, reconstructs the solution $q(x, t)$ from the evolved scattering data $S(t)$. In the following, we show the formulas required to solve each step.

Direct scattering problem

The functions $a(\xi)$ and $b(\xi)$ can be expressed in terms of the Wronskians of $\phi(x, \xi)$, $\psi(x, \xi)$ and $\bar{\psi}(x, \xi)$ as follows:

$$a(\xi) = W(\phi, \psi), \; b(\xi) = -W\left(\phi, \bar{\psi}\right). \tag{2.13}$$

The functions $a(\xi)$, $\phi(x,\xi)$ and $\psi(x,\xi)$ can be extended to form analytic functions $a(\zeta)$, $\phi(x,\zeta)$ and $\psi(x,\zeta)$, where $\zeta \in \mathbb{C}$ lies in the *upper half* of the complex plane. To find the discrete eigenvalues, one simply needs to find the zeros of the function $a(\zeta)$. To find the functions $\phi(x,\zeta)$ and $\psi(x,\zeta)$ for the potential $q(x,0) \in L^2$, let

$$M(x,\zeta) = e^{i\zeta x}\phi(x,\zeta) \tag{2.14}$$

and

$$N(x,\zeta) = e^{-i\zeta x}\psi(x,\zeta). \tag{2.15}$$

The advantage of the functions $M(x,\zeta)$ and $N(x,\zeta)$ is that they have fixed boundary conditions for $|x|$ approaching infinity (see (2.8)). By expressing the solutions of the ZS eigenvalue problem in terms of the Green's functions and applying the Fourier transform method (for more details, as well as a proof of existence and uniqueness of solutions, see [7]) one can obtain the following Volterra integral equations:

$$\begin{aligned} M_1(x,\zeta) &= 1 + \int_{-\infty}^{x} q(x') M_2(x',\zeta)\, dx' \\ M_2(x,\zeta) &= -\int_{-\infty}^{x} e^{2i\zeta(x-x')} q^*(x') M_1(x',\zeta)\, dx' \end{aligned}, \tag{2.16}$$

and

$$\begin{aligned} N_1(x,\zeta) &= -\int_{x}^{\infty} e^{2i\zeta(x-x')} q(x') N_2(x',\zeta)\, dx' \\ N_2(x,\zeta) &= 1 + \int_{x}^{\infty} q^*(x') N_1(x',\zeta)\, dx' \end{aligned}. \tag{2.17}$$

Once the functions $M(x,\zeta)$ and $N(x,\zeta)$ are known, one can calculate the scattering data by constructing the functions $a(\zeta)$ and $b(\zeta)$ from equations (2.13).

Time evolution of the scattering data

The time evolution of the scattering data can be calculated from the temporal Lax operator (2.5). It can be shown that

$$\begin{aligned} a(\zeta,t) &= a(\zeta,0) \\ b(\zeta,t) &= b(\zeta,0)\, e^{4i\zeta^2 t} \end{aligned} . \tag{2.18}$$

Therefore

$$\zeta_j(t) = \zeta_j(0), \quad C_j(t) = C_j(0)\, e^{4i\zeta^2 t} \text{ for } j = 1, \cdots, N, \tag{2.19}$$

and

$$\rho(\xi,t) = \rho(\xi,0)\, e^{4i\xi^2 t}. \tag{2.20}$$

The inverse scattering problem

To reconstruct the solution $q(x,t)$ from the evolved scattering data $S(t)$, one needs to solve the following Gel'fand-Levitan-Marchenko integral equation:

$$K(x,y) = F^*(x+y) - \int_x^\infty \left[\int_x^\infty K(x,s')\, F(s+s')\, ds' \right] F^*(y+s)\, ds, \tag{2.21}$$

where the function $F(x)$ is defined in terms of the scattering data

$$F(x) = \frac{1}{2\pi} \int_{-\infty}^{\infty} \rho(\xi)\, e^{i\xi x} d\xi - i \sum_{j=1}^{N} C_j e^{i\zeta_j x}. \tag{2.22}$$

Then

$$q(x,t) = -2K(x,x). \tag{2.23}$$

2.4 Conservation laws

It is well known that the NLS equation has an infinite sequence of conservation laws. Of particular importance is the three lowest-order integrals,

$$E = \int_{-\infty}^{\infty} |q|^2 \, dx,$$

$$M = i \int_{-\infty}^{\infty} \left(q_x q^* - q_x^* q\right) dx,$$

and

$$H = \frac{1}{2} \int_{-\infty}^{\infty} \left(|q_x|^2 - |q|^4\right) dx.$$

Here E is the total mass, M is the momentum and H is the Hamiltonian. The first of these conserved integrals, namely the mass, are used extensively throughout the thesis. This quantity has different meanings in different physical applications. In hydrodynamics, it refers to total mass, in quantum mechanics it is the number of quanta, in optics it refers to the power of the pulse. In all these applications, the conserved quantity E has some energy-related meaning.

An interesting fact about the IST method is that the quantities can be divided between the soliton part and the radiation part. In particular, for a potential $q(x,0)$ we get that (see e.g. [60])

$$E = E_{sol} + E_{rad} = 4 \sum_{n=1}^{N} \eta_n + \frac{1}{\pi} \int_{-\infty}^{\infty} \ln |a(\xi)|^{-2} \, d\xi, \tag{2.24}$$

where the potential $q(x,0)$ has N discrete eigenvalues $\zeta_1, \zeta_2, \cdots, \zeta_N$ where $\zeta_n = \xi_n + i\eta_n$. From the time independence of both the discrete eigenvalues and the function $a(\zeta)$, it follows that the mass of the solitons E_{sol} and the mass of radiaton E_{rad} are also conserved quantities.

2.5 The soliton structure of the NLS

As early as 1974, soon after the NLS equation was solved [113], it was recognized that the general structure of the NLS equation can be well understood in terms of the IST. As it turns out, all solutions are made up of a combination of two ingredients, namely solitons and radiation. Solitons are localised waves that propagate with constant velocity and without change in shape. Radiation, on the other hand, refers to linear dispersive wave trains of small amplitude. The structure of solutions of the NLS equation was elegantly described by Ablowitz, Kaup, Newell and Segur [4] who noted: "*when the solutions are valid for long time, the radiation has significantly decayed and the solitons can be seen as localized pulses with permanent shape travelling in a sea of radiation*".

We saw that the IST consists of three steps. The first step, the direct scattering problem, maps the initial condition, $q(x,0)$, onto the scattering data $S(0)$. The question we ask is the following: what information about the solution $q(x,t)$ is contained in the initial scattering data $S(0)$?

As it turns out, the direct scattering problem maps the potential $q(x,t)$ onto a soliton set and a radiation set. The information about the solitons, or the soliton content, makes up the discrete scattering data. This is the part of the scattering data that is related to the discrete spectrum of the ZS eigenvalue problem, i.e. the discrete eigenvalues $\zeta_1, \cdots, \zeta_N$ and their associated normalisation coefficients $C_1, \cdots, C_N$. The information about the radiation is contained in the continuous scattering data, consisting of the reflection coefficient $\rho(x)$ for $x \in \mathbb{R}$. The interaction between solitons and radiation is not trivial, and is captured in the inverse scattering problem, in particular (2.21) - (2.23). However, the time evolution of the discrete scattering data (2.19) and the continuous scattering data (2.20) are uncoupled. This means that, during the time evolution of any potential, no solitons are created or destroyed. Also, from the conservation of mass (2.24) it follows that the mass of both the soliton part and the radiation part of all solutions are conserved. Therefore, given the initial scattering

data, one can calculate the total mass of the solitons and the total mass of the radiation.

The rest of this section is dedicated to the relationship between the initial scattering data and the corresponding solutions. We start by considering radiation. This is used to develop an intuitive idea of the relationship between radiation and the continuous scattering data. This is followed by the most important part of the chapter, namely the relationship between solitons and the scattering data. This is done by considering soliton solutions, i.e. solutions with zero reflection. Finally, we consider a Gaussian initial potential to demonstrate the soliton content in a solution consisting of a soliton with non-zero radiation.

2.5.1 Radiation

Radiation arises naturally for potentials with small amplitude. Ablowitz, Kaup, Newell and Segur [4] showed that, for small potentials, the IST reduces to the Fourier transform method for solving the linearized NLS equation. In their paper, they considered a solution of the form $q(x,t) = \varepsilon p(x,0)$, where $p \in \mathbb{L}^2$ and $\varepsilon \to 0$. In this case, there are no discrete eigenvalues. To find the reflection coefficient, we substitute the initial condition into the integral equations (2.16), giving

$$M_1(x,\xi) = 1 + \mathbb{O}\left(\varepsilon^2\right). \tag{2.25}$$

Substituting (2.25) into the second equation of (2.16) gives

$$M_2 = -e^{2i\xi x}\int_{-\infty}^{x} q^*(x')\, e^{-2i\xi x'}dx' + \mathbb{O}\left(\varepsilon^2\right). \tag{2.26}$$

In the limit $x \to \infty$ it follows that $a(\xi) = 1$ in the leading order of ε. Then $\rho(\xi) = b(\xi) = -\tilde{q}^*(-2\xi)$, where $\tilde{q}(k)$ is the Fourier transform of $q(x)$, defined by

$$\tilde{q}(k) = \int_{-\infty}^{\infty} q(x')\, e^{-ikx'}dx'.$$

Note that, in this case, the forward scattering problem reduces to a Fourier transform. From equation (2.20) it follows that the time evolution of the reflection coefficient is given by

$$\rho(\xi,t) = -\int_{-\infty}^{\infty} q^*(x',0)\, e^{2i\xi x' + 4i\xi^2 t} dx'.$$

For the inverse scattering problem, the GLM equation (2.21) becomes

$$K(x,y) = F^*(x+y) + \mathbb{O}\left(\varepsilon^2\right),$$

and, in the leading order, reduces to

$$q(x,t) = -2F^*(2x) = \frac{1}{2\pi}\int_{-\infty}^{\infty} \tilde{q}(\xi,0)\, e^{i\left(\xi x - \xi^2 t\right)} d\xi.$$

This shows that, for small ε, the reflection coefficient reduces to a Fourier transform, while the inverse scattering problem reduces to an inverse Fourier transform. The solution disperses as time evolves, as is the case in the linearized NLS equation. This has led to the term "nonlinear Fourier analysis" to describe the IST.

In the general case, the reflection coefficient corresponds to the dispersive part of the solution. The radiation forms dispersive wave trains of small amplitude, and thus "radiates" away from the solitons. Radiation arises in general, unless the potential has zero reflection, i.e. $\rho(\xi) \equiv 0$. These solutions are called reflectionless potentials, or soliton solutions. These solutions and their related scattering data are considered next.

2.5.2 Soliton solutions

As a consequence of integrability, the NLS equation has soliton solutions. Solitons are spatially localised waves that interact elastically with each other. Soliton solutions can be obtained in various ways. Inverse scattering theory can be applied by choosing the appropriate scattering data and solving the inverse scattering problem. To do so, one sets the reflec-

tion coefficient $\rho \equiv 0$, and chooses a number of discrete eigenvalues and their corresponding normalisation coefficients [8]. Other methods have also been developed for finding soliton solutions, such as Hirota's method [53] and Darboux transformations [71]. In this section, we consider single solitons, breathers and soliton collisions. Throughout the discussion we emphasize the relationship between the discrete eigenvalues of the ZS eigenvalue problem and solitons.

Single solitons

Single soliton solutions of the NLS equation are given by

$$q(x,t) = 2\eta \text{sech}\left[2\eta\left(x + 4\xi t\right) - 2\delta_0\right] \exp\left[-2i\xi x + 4i\left(\eta^2 - \xi^2\right)t - i\left(\psi_0 + \frac{\pi}{2}\right)\right]. \quad (2.27)$$

From (2.27) it follows that the amplitude of the soliton is given by 2η, while the velocity is given by -4ξ, and the width of the soliton is inversely proportional to its amplitude. It is important to note that these characteristics are directly related to the discrete spectrum. Indeed, the discrete spectrum consists of a single eigenvalue in the upper half of the complex plane $\zeta = \xi + i\eta$. The initial position and initial phase of the soliton is determined by δ_0 and ψ_0 respectively. In terms of the scattering data, these parameters depend on the imaginary

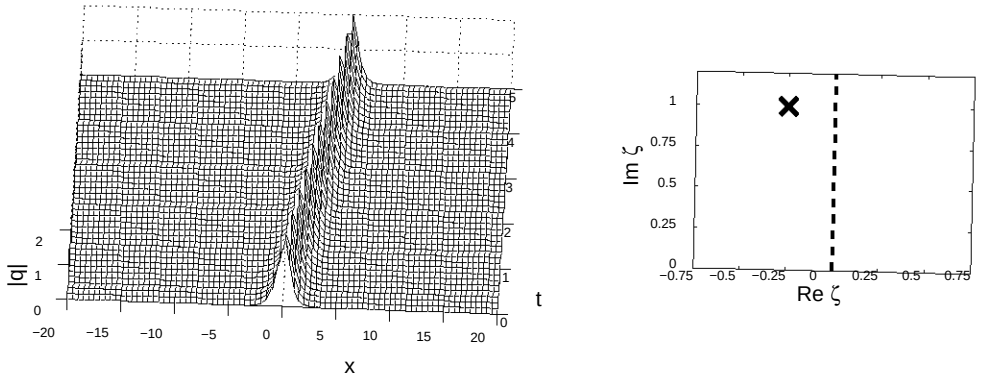

(a)

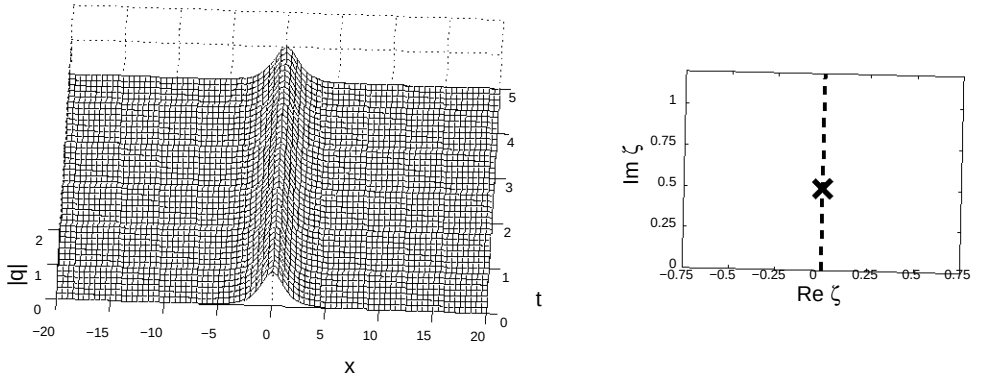

(b)

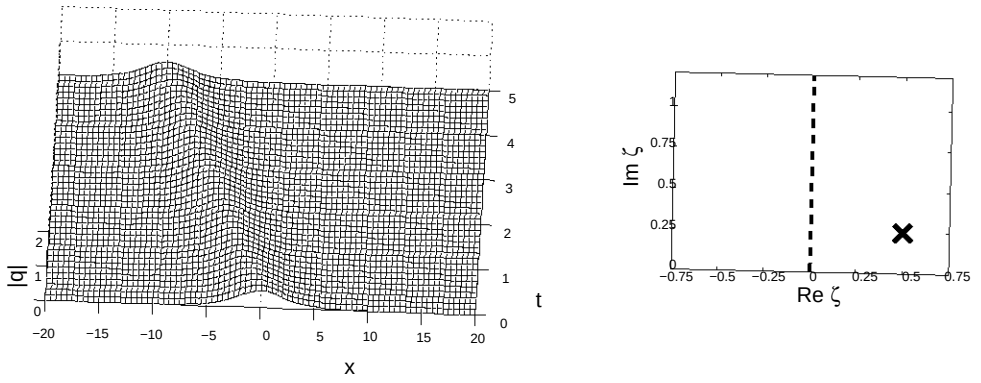

(c)

Figure 2.1: *Single solitons, with their associated discrete spectra. In (a), the soliton corresponds to an eigenvalue* $\zeta = -0.25 + i$. *In (b), the soliton corresponds to an eigenvalue* $\zeta = 0.5i$. *In (c), the soliton corresponds to an eigenvalue* $\zeta = 0.5 + 0.25i$.

part of the eigenvalue η and the normalisation coefficient C_1. The relationship is given by

$$C_1(0) = 2\eta e^{2\delta_0 + i\psi_0}. \tag{2.28}$$

In Figure 2.1 the solutions of three different solitons are plotted. On the right hand side of each picture, the associated discrete spectrum is shown. In (a), the discrete eigenvalue is $\zeta = -0.25 + i$. The soliton travels with velocity $V = -4\xi = 1$, where ξ represents the real part of the eigenvalue. The soliton has an amplitude $A = 2\eta = 2$. In (b), the discrete eigenvalue is given by $\zeta = 0.5i$. Since the real part of the eigenvalue is zero, the soliton is stationary, with amplitude $A = 2\eta = 1$. In (c), the associated eigenvalue is given by $\zeta = 0.5 + 0.25i$. The velocity is given by $V = -4\xi = 2$, while the amplitude is given by $A = 2\eta = 0.5$. Note also that the width is inversely proportional to the amplitude. For example, the soliton in (a), with large amplitude, is much thinner than the one in (c), with small amplitude.

Breathers

Breathers are soliton solutions that are associated with the two ZS eigenvalues with identical real parts. This corresponds to two solitons with identical velocity. One could think of this as a nonlinear analogue of a superposition of two solitons. Here we consider breathers with zero velocity, associated with ZS eigenvalues $\zeta_{1,2} = i\eta_{1,2}$. In this case breathers are time periodic. To study the spatial structure of breathers, we use the following exact solution [11]

$$q(x,t) = \frac{4i\left(\eta_2^2 - \eta_1^2\right)\left[\eta_1 \cosh\left(2\eta_2 x\right) e^{2i\eta_1^2 t} - \eta_2 \cosh\left(2\eta_1 x\right) e^{2i\eta_2^2 t}\right]}{\left(\eta_2 - \eta_1\right)^2 C_+ + \left(\eta_1 + \eta_2\right)^2 C_- - 4\eta_1\eta_2 \cos\phi}, \tag{2.29}$$

where $\eta_2 > \eta_1$, $C_\pm = \cosh\left[2\left(\eta_2 \pm \eta_1\right)x\right]$ and $\phi = 2\left(\eta_2^2 - \eta_1^2\right)t$. The temporal period of these solutions are $\pi/\left(\eta_2^2 - \eta_1^2\right)$. The spatial structure of the breather depends on the relative

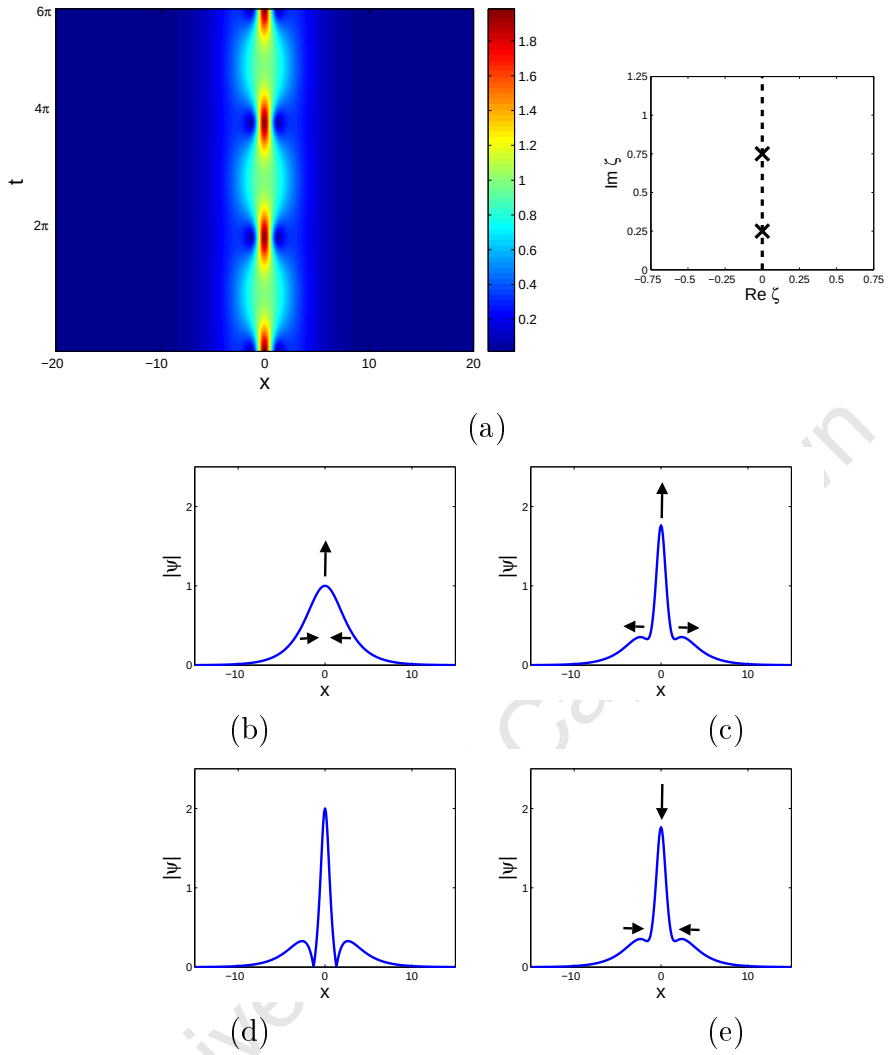

Figure 2.2: *Solution of a breather with large relative distance, associated with ZS eigenvalues* $\zeta_1 = 0.75i$, $\zeta_2 = 0.25i$. *(a)* $t = \pi$, *(b)* $t = 2\pi - 0.628$, *(c)* $t = 2\pi$, *(d)* $t = 2\pi + 0.628$.

distance between the ZS eigenvalues, defined as

$$d_{rel} = \frac{\eta_1 - \eta_2}{\eta_1}.$$

Breathers that arise for large relative distances between ZS eigenvalues ($d_{rel} \geq 0.5$) behave differently to breathers with small relative distances between ZS eigenvalues ($d_{rel} < 0.5$). We consider each case separately:

Large relative distance

Two purely imaginary ZS eigenvalues with a large relative distance are associated with a breather that consists of an oscillating quiescent soliton at the origin and two lateral waves that appear and disappear periodically. In Figure 2.2 we show the solution for the breather that arises for ZS eigenvalues $\zeta_{1,2} = i\eta_{1,2}$ for $\eta_1 = 0.75$ and $\eta_2 = 0.25$. The breather has a temporal period of $T = 2\pi$. In (a) the solution is shown at $t = \pi$. The solution consists of a single soliton. As time evolves, the width of the soliton decreases while the amplitude increases. In (b) we show the solution at $t = 2\pi - 0.628$. Here we see that two lateral waves are formed on opposite sides of the soliton. These waves separate from the soliton while the soliton's amplitude increases and its width decreases. In (c) the solution is shown for $t = 2\pi$. Here the amplitude of the soliton reaches its maximum. At this point the two smaller waves are completely separated from the soliton. As time evolves beyond $t = 2\pi$ the amplitude of the soliton decreases, the width of the soliton increases, and the lateral waves are absorbed by the widening soliton. This is shown in (d) where the solution is shown for $t = 2\pi + 0.628$. At $t = 3\pi$ the solution returns to the single soliton shown in (a), completing the cycle.

Small relative distance

Two purely imaginary ZS eigenvalues with small relative distance correspond to breathers that vary between a single-soliton and two-soliton states. The two solitons periodically attract each other, followed by a collision. During the collision, a single soliton forms with two lateral waves on opposite sides of the soliton. After the collision, the two solitons re-emerge, followed by a period where the two solitons move away from each other. This continues until they reach a maximum separation distance. Thereafter the solitons attract each other again, and the cycle is repeated. An example is shown in Figure 2.3 for the breather corresponding to purely imaginary ZS eigenvalues with imaginary parts $\eta_1 = 0.55$ and $\eta_2 = 0.45$. In this case the temporal period of the breather is given by $T = 10\pi$. In (a) we show the solution at

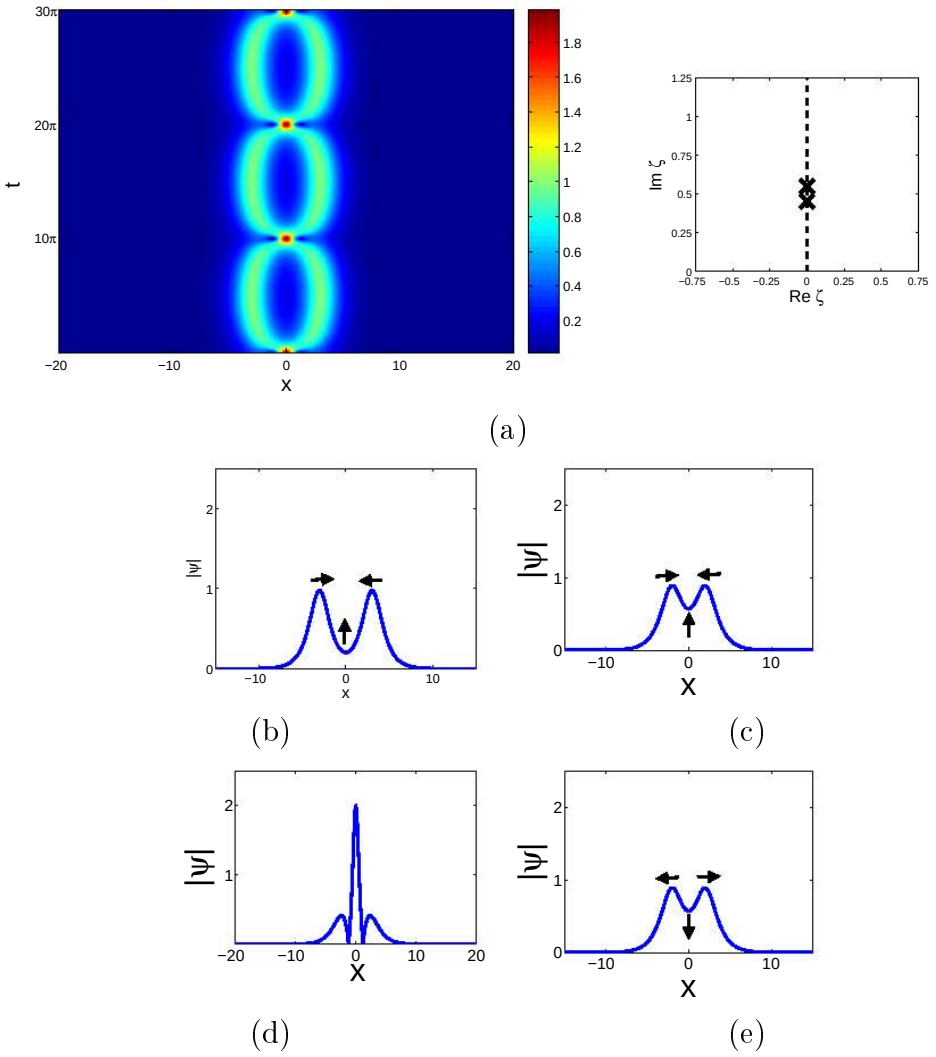

Figure 2.3: *Solution of a breather with small relative distance, associated with ZS eigenvalues* $\zeta_1 = 0.55i$, $\zeta_2 = 0.45i$. *(a)* $t = 5\pi$, *(b)* $t = 10\pi - 3.456$, *(c)* $t = 10\pi$, *(d)* $t = 10\pi + 3.456$.

$t = 5\pi$. This represents the point in time where the two solitons are separated the furthest in terms of spatial position. As time evolves, these solitons move toward each other. When they get close to each other, they start to interact. The result is that their amplitudes start to decrease while the value at $x = 0$ increases. This is shown in (b) where $t = 9\pi - 0.314$. As time evolves beyond $t = 10\pi - 3.456$, the two solitons collide, leading to the formation of a single soliton with two smaller waves on opposite sides. In (c) we show the solution at $t = 10\pi$ where the amplitude of the single solution reaches its maximum while the two smaller waves are completely separated from the soliton. As time evolves beyond $t = 10\pi$

the amplitude of the soliton decreases and widens until the two original solutions re-appear. This is shown in (d) where $t = 10\pi + 3.456$. These solitons move away from each other until they return to the maximum separation at $t = 15\pi$. At this point the solution is the same as the solution at $t = t_1$ shown in (a), completing the cycle.

Soliton collisions

A remarkable aspect of solitons in the NLS equation is that their collisions are reflectionless, and after collision each soliton retains its form and velocity as before the collision. Indeed, the only effect the collision has on the solitons is a change in phase. Let's consider the collision of two solitons associated with ZS eigenvalues $\zeta_{\pm} = \pm\xi + i\eta$, corresponding to two solitons with the same shape and velocity, traveling in opposite directions. An analytical expression of the solution is given by [11]

$$q\left(x,t\right) = -8i\eta\xi\,\frac{A+iB}{D}\,e^{-2i\left(\eta^2+\xi^2\right)t}, \tag{2.30}$$

where

$$A = 4\mathrm{cosh}4\eta\xi t\,\left[\xi\mathrm{cosh}2\eta x\,\mathrm{cos}2\xi x - \eta\mathrm{sinh}2\eta x\,\mathrm{sin}2\xi x\right],$$

$$B = \mathrm{sinh}\left(4\eta\xi t\right)\left[\xi\mathrm{sinh}2\eta x\,\mathrm{sin}2\xi x + \eta\mathrm{cosh}2\eta x\,\mathrm{cos}\left(2\xi x\right)\right],$$

and

$$D = \xi^2\mathrm{cosh}4\eta x + \left(\eta^2+\xi^2\right)\mathrm{cosh}8\eta\xi t - \eta^2\mathrm{cos}4\xi x.$$

The behaviour during the collision of the solitons depends on the amplitude/velocity ratio defined as

$$r_{col} = \eta/\xi. \tag{2.31}$$

For a large amplitude/velocity ratio ($r_{col} > 1/4$) the collision is different to the case of solitons with a large amplitude/velocity ratio ($r_{col} \leq 1/4$). Let's consider each case separately:

Large amplitude/velocity ratio

The collision of two solitons with large amplitude/velocity ratio has an interesting resemblance to breathers. Indeed, at the climax of the collision, the solution consists of a soliton with two lateral waves. The collision of solitons with large amplitude/velocity ratio is illustrated in Figure 2.5 where we show the soliton collision associated with ZS eigenvalues $\pm 0.2 + 0.2i$. In (a) we show the solution on the left, while the ZS eigenvalues are shown on the right. The solution shows that, after the collision, the two solitons propagate without change of velocity or shape. In Figure 2.5 (b) to (h) we show the behaviour of the solution during the collision. In (b) the solution is shown at $t = -50$. Here we can see the two solitons approaching each other. In (c) the solution is shown for $t = -20$. Here we see that, as the two solitons get closer to one another, the neighbouring tails begin to interact. The interaction leads to the amplitude at $x = 0$ to increase. As time progresses, a small wave starts to form at the origin. This can be seen in (d) where the solution is shown for $t = -7$. Here we see that, during this time, the amplitude of the newly-formed wave increases, while the amplitudes of the original solitons decrease. This continues until $t = 0$, where the collision is at its climax, shown in (e). Here the solution consists of a soliton situated at the origin, and two lateral waves. At this point the amplitude of the soliton obtains its maximum. Note the resemblance with breathers shown in Figure 2.2 (d) and Figure 2.3 (d).

As time evolves beyond $t = 0$, the amplitude of the central soliton decreases while the amplitudes of the lateral waves increase. This marks the reformation of the original solitons. In Figure 2.3 (e) we show the solution at $t = 7$. Here we see that the amplitudes of the lateral waves increase, while the solution at the origin decreases. In (f) the solution is shown at $t = 20$ where we see the two solitons formed. At $t = 50$ the two soliton have completely passed through each other, and propagate as before the collision. This is shown in (g).

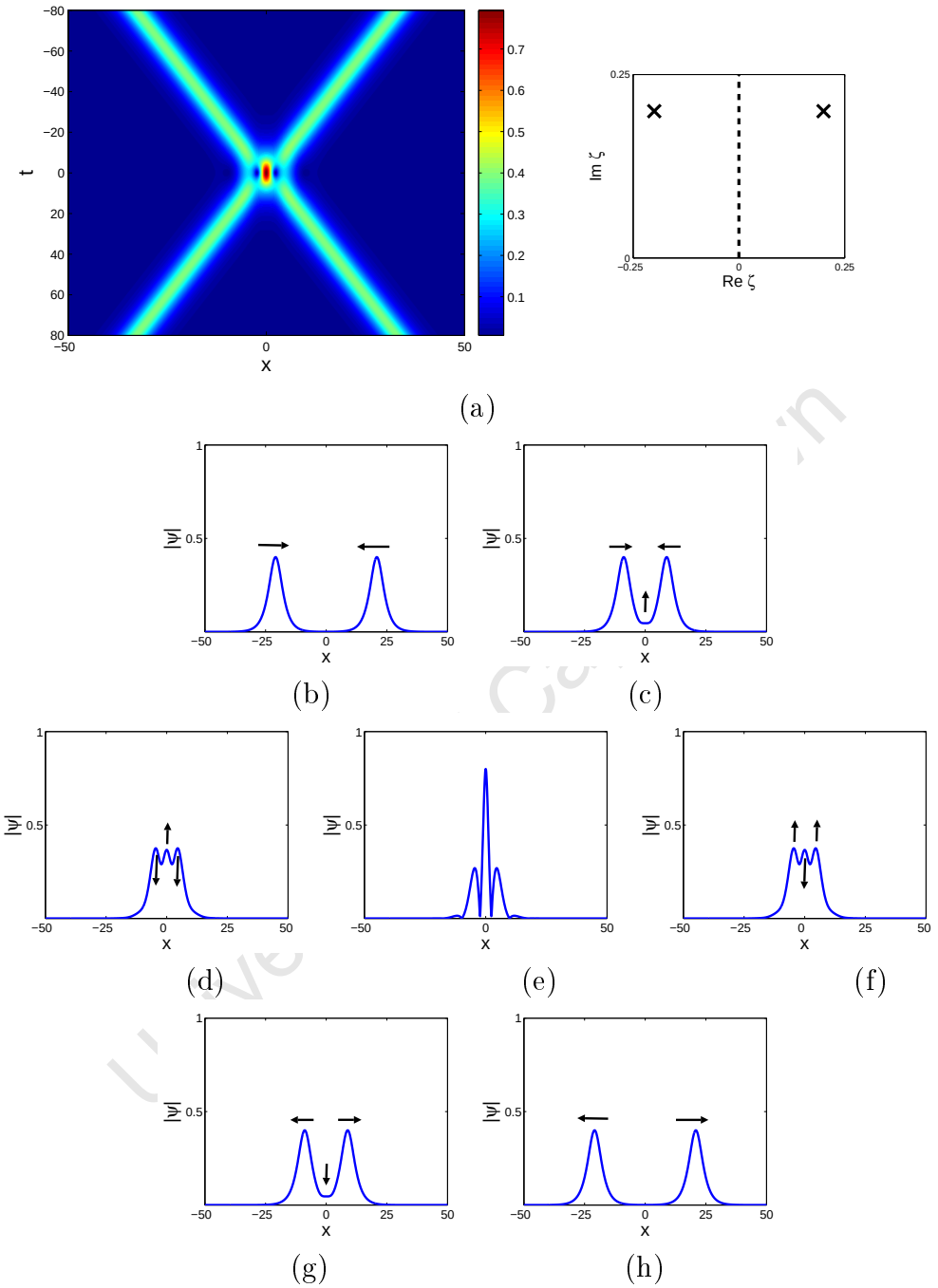

Figure 2.4: *Soliton collision associated with ZS eigenvalues* $\zeta = \pm 0.2 + 0.2i$. *In (a) the solution (left) and the ZS eigenvalues (right) are shown. The solution is shown for (b)* $t = -50$, *(c)* $t = -20$, *(d)* $t = -7$, *(e)* $t = 0$, *(f)* $t = 7$, *(g)* $t = 20$, *(h)* $t = 50$.

Small amplitude/velocity ratio

The behaviour of the solution during the collision of two solitons with small amplitude/velocity ratio is different to those observed in breathers. At the climax of the collision. the solution consists of a large number of thin waves similar to an interference pattern.

The collision of solitons with small amplitude/velocity ratio is illustrated in Figure 2.5 where we show the soliton collision associated with ZS eigenvalues $\pm 0.2 + 0.05i$. In (a) we show the solution on the left, while the ZS eigenvalues are shown on the right. The difference in behaviour during collision can be seen on the interval $-50 \leq t \leq 50$. In Figure 2.5 (b) to (h) we show the behaviour of the solution during the collision. It is important to note that the spatial interval of these plots is varied. In (b) the solution is shown at $t = -300$. Here we can see the two solitons approaching each other. In (c) the solution is shown for $t = -75$. Here we see that, as the two solitons get closer to one another, a number of smaller waves are formed symmetrically about the origin. As time evolves, a larger number of these smaller waves are formed. This can be seen in (d) where the solution is shown for $t = -25$. At this point the amplitudes of these waves increases up to the climax of the collision at $t = 0$ shown in (e). Note the contrast between this solution and that of the large amplitude/velocity ratio solution shown in Figure 2.2 (e).

As time evolves beyond $t = 0$, the ampitude of the wave at the origin decreases while the smaller waves spread across the spatial domain (note the difference in spatial interval of these figures). This marks the reformation of the original solitons. In Figure 2.3 (f) we show the solution at $t = 25$. Here we see that the original solitons almost fully recovered their shape while the smaller waves are disappearing. In (g) the solution is shown at $t = 75$ where we see the two solitons formed. At $t = 300$ the two soliton have completely passed through each other, and propagate as before the collision. This is shown in (g).

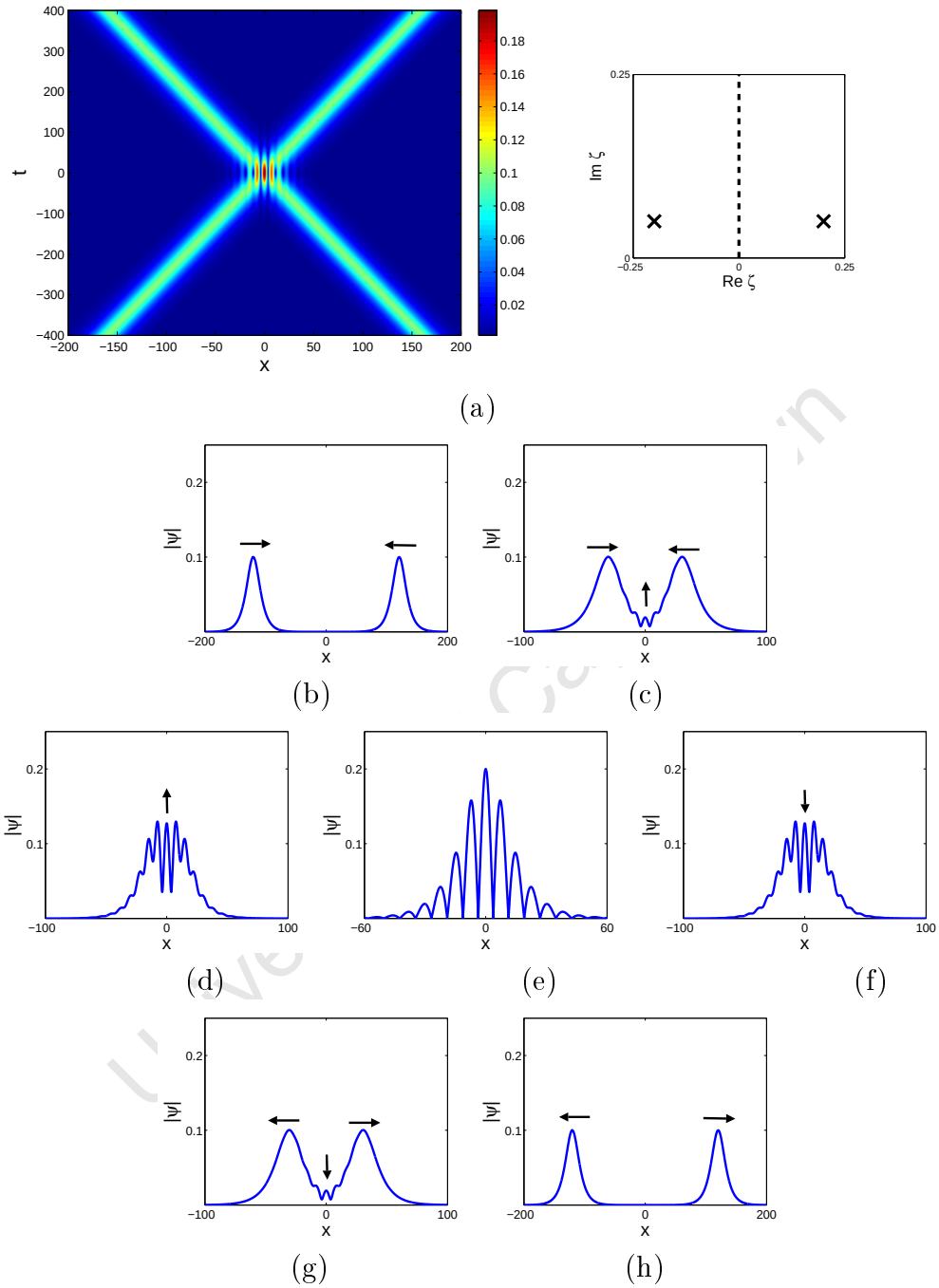

Figure 2.5: *Soliton collision associated with ZS eigenvalues* $\zeta = \pm 0.2 + 0.05i$. *In (a) the solution (left) and the ZS eigenvalues (right) are shown. The solution is shown for (b)* $t = -300$, *(c)* $t = -75$, *(d)* $t = -25$, *(e)* $t = 0$, *(f)* $t = 25$, *(g)* $t = 75$, *(h)* $t = 300$.

Multiple solitons

Soliton solutions can be found for any finite number of soliton. If the solution consists of N solitons, corresponding to N discrete eigenvalues $\zeta_j = \xi_j + i\eta_j$ for $j = 1, 2, \cdots, N$, with distinct real parts, it can be shown that, in the limit as $t \to \infty$, the solitons separate to form N solitons of the form (2.27). If this restriction is dropped, multiple breathers can be formed. Breathers have the same elastic collision properties as solitons.

2.5.3 The soliton structure for general solutions

For arbitrary initial conditions, solutions consist of solitons and radiation. Although solitons and radiation interact, no energy is transferred during propagation. In terms of the IST, the discrete scattering data describes the behaviour of the soliton part of the solution, while the continuous scattering data describes the behaviour of the radiation. As was discussed, the discrete spectrum of a potential contains the number of solitons, as well as the amplitude and velocity of each of them. Therefore, we use the term "soliton content" for the discrete spectrum associated with a solution. The purpose of this thesis is to use the soliton content to analyze solitons arising in the PDNLS equation, a near integrable equation.

For the NLS equation, this concept is perhaps best illustrated by means of an example. Consider the Gaussian initial condition

$$q(x, 0) = e^{-x^2}. \tag{2.32}$$

From the single lobe theorem (discussed in Chapter 3), it follows that the associated ZS eigenvalue problem has exactly one purely imaginary eigenvalue. Numerical results show that $\zeta \approx 2i/15$. This implies that a stationary soliton with amplitude $A \approx 4/15$ will emerge as time evolves. Figure 2.6 (a) shows the numerically calculated time evolution of the Gaussian intial condition. We see that the initial pulse spreads across the spatial domain. A part of the solution forms a stationary soliton, as was predicted by the discrete eigenvalue, while the

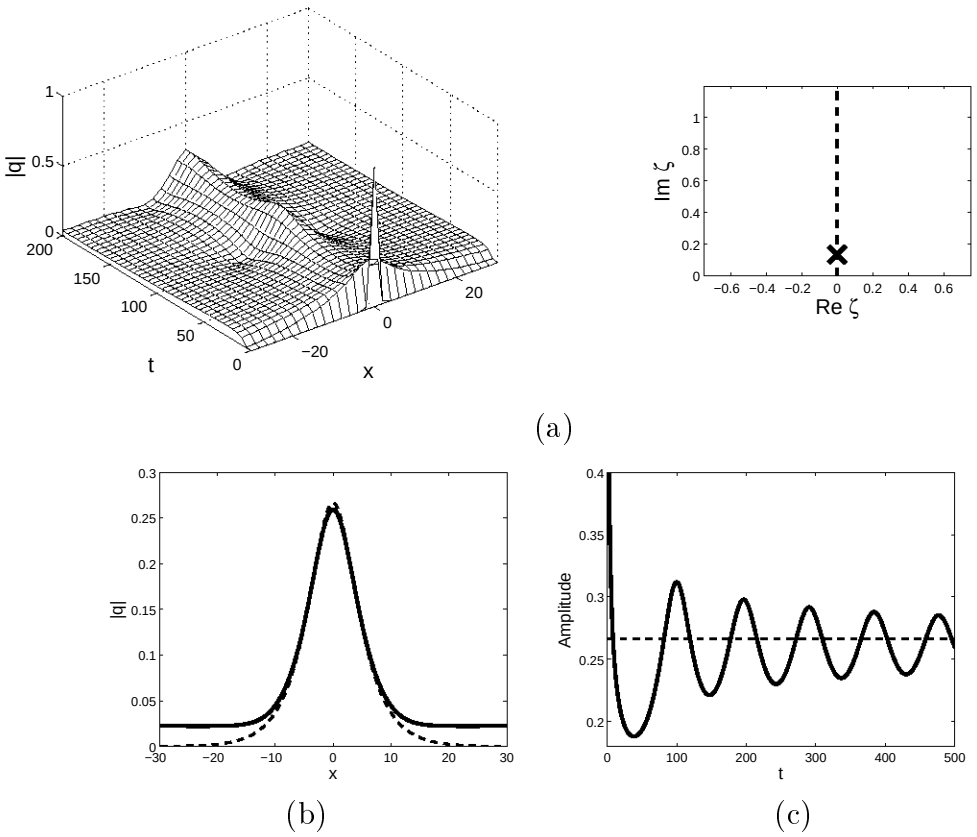

Figure 2.6: *The solution of a Gaussian initial condition. In (a), the solution is shown. In (b), the solution is shown at* $t = 500$. *The dotted line shows the soliton content, given by* $\frac{4}{15}sech\frac{4}{15}x$, *corresponding to the discrete spectrum of the associated ZS eigenvalue problem. It is seen that the solution approaches the soliton on the interval* $-10 < x < 10$, *with dispersive tails. In (c), the amplitude is shown for* $t \leq 500$.

rest of the solution disperses, corresponding to radiation in the system. In Figure 2.6 (b) we show the solution at $t = 500$. The dotted line represents the sech-like soliton (2.27) with amplitude $A = 4/15$. We see that the solution consists of the predicted soliton with dispersive tails. Therefore, given an initial condition, the corresponding discrete spectrum can be used to find the soliton content, that is, the part of the solution that does not disperse over time. In Figure 2.6 (c), the amplitude of the solution is shown as a function of time. We see that the amplitude oscillates around the dotted line due to the interaction between the soliton and radiation. This line represents the predicted soliton amplitude $A = 4/15$.

2.6 Beyond integrability: Perturbed NLS equations

The NLS equation describes waves in dispersive media that contain a cubic nonlinearity. When other factors, like damping, driving, and higher order nonlinearities are taken into account, the resulting equation is no longer integrable. The perturbed NLS equation can be written in the form

$$iq_t + q_{xx} + 2|q|^2 q = \epsilon R(q). \tag{2.33}$$

Since the perturbed NLS equation (2.33) is no longer integrable, it can no longer be solved through the inverse scattering transform method. In particular, the scattering data no longer satisfy the evolution equations (2.18) - (2.20). However, if q is a solution of the perturbed NLS equation (2.33), one can still calculate the scattering data of the solution $S(t_0)$, where t_0 is a fixed point time. Likewise, given the scattering data $S(t_1)$, the solution $q(x, t_1)$ can be reconstructed, where t_1 is an arbitrary fixed point in time. Therefore, in the perturbed case, one has to find an expression of the time evolution of the scattering data.

For small perturbations of the NLS equation, i.e. equation (2.33) with $\epsilon \ll 1$, the time evolution of the scattering data can be calculated by means of a perturbation expansion. Of particular importance is the time evolution of the discrete spectrum, as it contains the soliton content. This approach was first developed by Kaup [57]. As an example, he considered the NLS equation with a small damping term, i.e. (2.33) with

$$R(q) = iq. \tag{2.34}$$

He considered a single soliton initial condition of the form (2.27), and showed that the first order expansion yields the following time evolution of the discrete eigenvalue $\zeta = \xi + i\eta$:

$$\zeta(t) = \xi(0) + i\eta(t) e^{-2\epsilon t}. \tag{2.35}$$

In terms of the soliton content, this shows that the amplitude of the soliton decreases, while

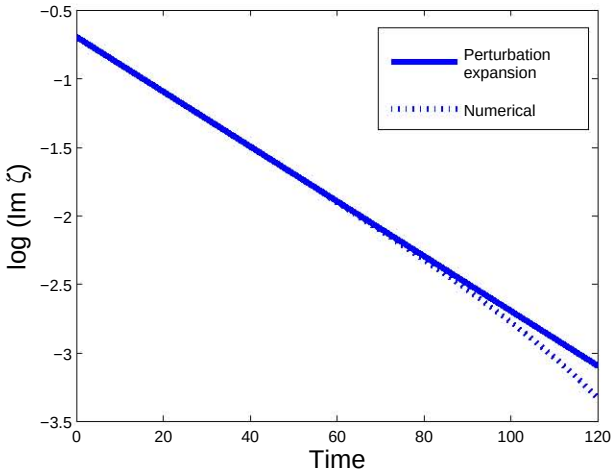

Figure 2.7: Time evolution of the discrete spectrum in the damped NLS equation.

the width of the soliton increases. Since the real part is time independent, the velocity of the decaying soliton stays constant.

To show the accuracy of the method, lets consider (2.33), $R(q) = iq$ and $\epsilon = 0.01$, and initial condition

$$q(x,0) = e^{ix/2}\text{sech}x. \tag{2.36}$$

From (2.27) it follows that the ZS eigenvalue problem with potential (2.36) has only one discrete eigenvalue in the upper-half complex plane, given by $\zeta(0) = -\frac{1}{4} + \frac{1}{2}i$. In Figure 2.7 the discrete spectrum, as predicted by the perturbation expansion (2.35), is shown with the solid line. The dotted line shows the time evolution of the discrete spectrum, calculated numerically (the numerical methods are discussed in Chapters 3 - 4). We see that the perturbation expansion is accurate for $t < 100$. This is to be expected, since the perturbation expansion is $\mathrm{O}(\epsilon)$ accurate, and therefore accurate up to $t \sim \mathrm{O}(1/\epsilon)$.

The time evolution of the discrete spectrum can be generalized for arbitrary perturbations. If the scattering data are known for the initial condition $q(x,0)$, i.e. the discrete eigenvalues $\zeta_1, \cdots, \zeta_N$, the Jost eigenfunctions $\psi = [\psi_1, \psi_2]^T$ and $\phi = [\phi_1, \phi_2]^T$, and the function $a(\zeta)$

defined in (2.9), it can be shown that [60]

$$\begin{aligned}\frac{d\zeta_j}{dt} &= \frac{1}{a'(\zeta_j)}\int_{-\infty}^{\infty}\left[\epsilon R(q)\,\psi_1(x,\zeta_n)\,\phi_2(x,\zeta_n)+\right.\\ &\left.+\,\epsilon^* R^*(q)\,\psi_2(x,\zeta_n)\,\phi_1(x,\zeta_n)\right]dx. \end{aligned} \tag{2.37}$$

From (2.37), it is clear that, as $\epsilon \to 0$, the rate of change of $\zeta_j(t)$ decreases to zero. Since the expansion is $\mathrm{O}(\epsilon)$ accurate, (2.37) predicts the change of discrete eigenvalues accurately for $t \sim \mathrm{O}(1/\epsilon)$.

Unfortunately the perturbation analysis does not provide a lot of insight for larger values of ϵ, say $\epsilon > 0.1$. Even so, solitons have been found in many NLS-type equations with large perturbations, such as the complex Ginzburg-Landau and other generalized NLS equations. In many cases, these solitons are found numerically. Moreover, many solitons found in non-integrable equations are temporally periodic, quasi-periodic, or temporally chaotic. In these cases, standard analytical methods, such as linearization and perturbation analyses (including the perturbed IST method) cannot be used to analyze the solitons.

In this thesis, we present a numerical approach to study solitons in non-integrable equations. We call this the direct scattering study. Our method relies on numerical methods to generate a (potentially time-dependent) soliton. The time evolution of the soliton content is then calculated numerically by using the soliton solution, at fixed times, as a potential of the ZS eigenvalue problem. The discrete spectrum of the resulting operator is then calculated numerically. The discrete spectrum of the associated ZS eigenvalue problem reveals the soliton content of the solution at a particular point in time. Therefore the time evolution of the discrete spectrum can be used to identify different types of solitons. In Chapter 5, we apply the direct scattering study to solitons in the PDNLS equation. The numerical methods are developed in Chapters 3 - 4.

It is important to understand the difference between our direct scattering study and the perturbed IST method. In the latter analysis, the time evolution of the discrete spectrum

is used to predict the behaviour of the solution. In our analysis, the solution has already been generated. Therefore, the time evolution of the discrete spectrum is used to describe the spatial characteristics of the soliton.

Chapter 3

Solving the Zakharov-Shabat eigenvalue problem numerically

The Zakharov-Shabat (ZS) eigenvalue problem forms the basis of the inverse scattering transform method to solve integrable partial differential equations, such as the nonlinear Schrödinger (NLS) equation. In Chapter 2 we showed that the scattering data are defined in terms of the eigenvalues and eigenfunctions of the ZS eigenvalue problem. While the existence and uniqueness of the scattering data are well established, it has proven very difficult to solve the ZS eigenvalue problem analytically. Indeed, there are only a small sub-class of potentials that can be solved analytically. This includes pure solitons (also known as reflectionless potentials), the Satsuma-Yajima sech potentials [90], and rectangular potentials solved by Manakov [70]. For many other potential, such as Gaussian potentials, the analytical solution of the ZS eigenvalue problem remains unsolved. Therefore one has to rely on numerical methods to study the behaviour of the scattering data.

The development of the IST method for periodic potentials led Overman [82] to solve the ZS eigenvalue problem numerically for periodic potentials. The ability to visualize the soliton content played an important role in the study of the IST for periodic potentials [31, 44, 45, 55, 64, 67]. Recently Deconinck and Kutz [38] introduced a particularly efficient

scheme that combines Floquet and Fourier-Hill theory for the calculation of the full spectrum for operators with periodic boundary conditions. The method is known as Hill's method, and is used extensively in this thesis.

Potentials defined on the real line are more awkward for direct numerical treatment due to the nature of the boundary conditions imposed on the eigenfunctions. Boffetta and Osborne [22] developed a method to calculate the direct scattering transform in this case, where they impose the boundary conditions using a shooting method. Another approach is to approximate infinite line potentials with periodic potentials with large periods. In this case, the potential of the large interval limit $L \to \infty$ is referred to as the homoclinic orbit. Gardner [47] proved that the spectrum of periodic potentials converge to the spectrum of the homoclinic orbit as the interval length $L \to \infty$. Deconinck and Kutz [38] used Hill's method to solve the ZS eigenvalue problem, relating to the Korteweg-de Vries equation on the infinite line, by using increasingly large periods.

In this chapter we study the rate of the large interval convergence numerically through Hill's method. Our numerical results show that, for the periodic ZS spectrum, there is an optimal choice of the Floquet exponent that converges fastest as the interval length $L \to \infty$. By convergence, we do not only mean better accuracy, but also the absence of spurious eigenvalues. By reducing the calculation of the periodic ZS-spectrum, the computational time is reduced significantly. These results are reported in the paper written by the author, Herbst and Molchan [81]. The chapter is structured as follows: In Section 3.1 we develop Floquet theory and apply it to the ZS eigenvalue problem. Floquet theory forms the basis of Hill's method, that is applied to the periodic ZS eigenvalue problem in Section 3.2. In Section 3.3 we consider the large interval limit of the periodic ZS eigenvalue problem. We formulate the use of a specific Floquet exponent, and use numerous numerical examples to justify this choice.

3.1 Floquet theory and the periodic ZS eigenvalue problem

Floquet theory applies to systems of ODE's of the form

$$\mathbf{v}' = P(x)\,\mathbf{v}, \tag{3.1}$$

where $\mathbf{v} = [v_1(x)\ v_2(x)\ \cdots, v_N(x)]^T_,$ and the matrix P is periodic with period L, i.e. $P(x+L) = P(x)$. A fundamental matrix of (3.1) is a matrix V whose columns $\mathbf{v}_1, \mathbf{v}_2, \cdots, \mathbf{v}_N$ consist of N linearly independent solutions of (3.1). Therefore $V' = PV$. The principal fundamental matrix is the unique fundamental matrix satisfying $V(0) = I$, where I is the $N \times N$ identity matrix.

For any fundamental matrix V of (3.1), it can be shown that there exists a non-singular constant matrix B satisfying

$$V(x+L) = V(x)\,B \quad \forall x. \tag{3.2}$$

One can also show that, for any two fundamental matrices, the corresponding non-singular constant matrices are similar. Therefore the eigenvalues of the matrix B only depend on the system (3.1), and not on the choice of the fundamental matrix. The N eigenvalues of B, $\rho_1, \rho_2, \cdots, \rho_N$ are called the Floquet multipliers of the system (3.1). The Floquet exponents $\nu_1, \nu_2, \cdots, \nu_N$ are defined as $\rho_j = e^{i\nu_j L}$ for $j = 1, 2, \cdots, N$.

Floquet's theorem is defined as follows:

> **Theorem 1 (Floquet's theorem)**: Let $\rho = e^{i\nu L}$ be a Floquet multiplier of the periodic system (3.1). Then there exists a solution $\mathbf{v}(x)$ such that $\mathbf{v}(x+L) = \rho\mathbf{v}(x)$. The solution satisfies $\mathbf{v}(x) = e^{i\nu x}\boldsymbol{\phi}(x)$, where the function $\boldsymbol{\phi}(x)$ is L-periodic, i.e. $\boldsymbol{\phi}(x+L) = \boldsymbol{\phi}(x)\ \forall x$.

Another useful theorem from Floquet theory is given below:

Theorem 2: Let $\rho_1, \rho_2, \cdots, \rho_N$ be the N Floquet multipliers for the system (3.1). Then

$$\rho_1 \rho_2 \cdots \rho_N = \exp\left[\int_0^L \operatorname{tr}\left\{P(x)\right\} dx\right].$$

Consider the periodic ZS eigenvalue problem

$$\begin{aligned} v_{1x} &= -i\zeta v_1 + q v_2 \\ v_{2x} &= -q^* v_1 + i\zeta v_2 \end{aligned}, \tag{3.3}$$

where the potential $q(x+L) = q(x)$ is a solution to the NLS equation. The continuous spectrum of the periodic ZS eigenvalue problem is defined as

$$\sigma_c^{(p)}(q) = \left\{\zeta \,|\mathbf{v}(x,\zeta) \text{ is bounded for all } x\right\}, \tag{3.4}$$

while the discrete spectrum is a subset of the continuous spectrum defined as

$$\sigma_d^{(p)}(q) = \left\{\zeta | \mathbf{v}(x+2L) = \mathbf{v}(x)\right\}. \tag{3.5}$$

We can rewrite equation (3.3) in the form $\mathbf{v}' = P\mathbf{v}$, where

$$P = \begin{pmatrix} -i\zeta & q \\ -q^* & i\zeta \end{pmatrix}. \tag{3.6}$$

Since $P(x+L) = P(x)$, Floquet theory applies. From Floquet theory it follows that, for any fixed choice of ζ, all solutions of (3.3) have the form

$$\mathbf{v}(x) = e^{i\nu x}\boldsymbol{\phi}(x), \tag{3.7}$$

where $\boldsymbol{\phi}(x) = [\phi_1(x)\ \phi_2(x)]^T$ is L periodic, i.e. $\boldsymbol{\phi}(x+L) = \boldsymbol{\phi}(x)$. Clearly the eigenfunctions are bounded if and only if $\nu \in \mathbb{R}$ in (3.7). For any ν, the corresponding eigenfunctions satisfy

$$\mathbf{v}(x+L) = e^{i\nu L}\mathbf{v}(x). \tag{3.8}$$

Since $e^{i\left(\nu+\frac{2\pi}{L}\right)L} = e^{i\nu L}$, all bounded eigenfunctions can be represented by (3.7) with Floquet exponents on the interval

$$\nu \in \left[-\frac{\pi}{L}, \frac{\pi}{L}\right). \tag{3.9}$$

For any fixed $\zeta \in \mathbb{C}$, the system (3.3) produces two Floquet exponents ν_1 and ν_2. Since the trace of P in (3.6) is zero, it follows from Theorem 2 that

$$e^{i\nu_1 L}e^{i\nu_2 L} = 1.$$

Therefore $\nu_2 = -\nu_1$. This implies that, for any fixed $\zeta \in \sigma_c^{(p)}$, if the corresponding eigenfunction $\mathbf{v}$ satisfies $\mathbf{v}(x+L) = e^{i\nu_1 L}\mathbf{v}(x)$, then ζ has a linearly independent eigenfunction $\mathbf{w}$ satisfying $\mathbf{w}(x+L) = e^{-i\nu_1 L}\mathbf{w}(x)$. This symmetry implies that all eigenvalues of the periodic ZS eigenvalue problem can be obtained by considering only the Floquet exponents in the interval

$$\nu \in \left[0, \frac{\pi}{L}\right]. \tag{3.10}$$

As a result the continuous spectrum of the periodic ZS eigenvalue problem arises as line segments in the complex plane, see for example Calini and Ivey [31]. One can define the continuous spectrum and the discrete spectrum of the periodic ZS eigenvalue problem in terms of Floquet theory as follows:

$$\sigma_c^{(p)}(q) = \left\{\zeta | \mathbf{v}(x+L) = e^{i\nu L}\mathbf{v}(x) \text{ for } \nu \in \left[0, \frac{\pi}{L}\right)\right\}, \tag{3.11}$$

$$\sigma_d^{(p)}(q) = \left\{\zeta | \mathbf{v}(x+L) = e^{i\nu L}\mathbf{v}(x) \text{ for } \nu = 0 \text{ or } \frac{\pi}{L}\right\}. \tag{3.12}$$

3.2 Hill's method for the periodic ZS eigenvalue problem

We now proceed to develop a numerical method to calculate the continuous spectrum of the ZS eigenvalue problem for periodic potentials. The method, known as Hill's method, was developed by Deconinck and Kutz [38].

We know from Floquet theory that all eigenfunctions can be written in the form (3.7). If we substitute this into the ZS eigenvalue problem (3.3) we get

$$\begin{aligned} i\nu\phi_1 + \phi_{1x} &= -i\zeta\phi_1 + q\phi_2 \\ i\nu\phi_2 + \phi_{2x} &= -q^*\phi_1 + i\zeta\phi_2 \end{aligned}. \tag{3.13}$$

Therefore Floquet theory allows us to redefine the original eigenvalue problem to a set of eigenvalue problems (3.13), depending on the Floquet exponents $\nu \in \left[0, \frac{\pi}{L}\right]$. Since ϕ_1 and ϕ_2 are periodic, we can write these functions as Fourier series

$$\phi_p(x) = \sum_{n=-\infty}^{\infty} \hat{\phi}_{p,n} e^{i\mu_n x}, \tag{3.14}$$

where

$$\hat{\phi}_{p,n} = \frac{1}{L} \int_{-L/2}^{L/2} \phi_p(x)\, e^{-i\mu_n x} dx, \tag{3.15}$$

$p = 1, 2$, and $\mu_n = -\frac{2\pi n}{L}$. The derivative of (3.14) is formally given by

$$\phi_p'(x) = \sum_{n=-\infty}^{\infty} i\mu_n \hat{\phi}_{p,n} e^{i\mu_n x}. \tag{3.16}$$

By substituting the Fourier series (3.14) and its formal derivative (3.16) into the ZS eigenvalue (3.13), one can write

$$\begin{array}{ll} \sum_{n=-\infty}^{\infty} e^{i\mu_n x/L}\left[i\alpha\left(\nu;n\right)\hat{\phi}_{1n}-q\hat{\phi}_{2n}\right] & =-i\zeta\sum_{n=-\infty}^{\infty} e^{i\mu_n x/L}\hat{\phi}_{1n} \\ \sum_{n=-\infty}^{\infty} e^{i\mu_n x/L}\left[-q^*\hat{\phi}_{1n}-i\alpha\left(\nu;n\right)\hat{\phi}_{2n}\right] & =-i\zeta\sum_{n=-\infty}^{\infty} e^{i\mu_n x/L}\hat{\phi}_{2n} \end{array}. \tag{3.17}$$

where $\alpha\left(\nu;n\right)=\nu+\mu_n$. If we multiply equations (3.17) with the factor $e^{i\mu_m x/L}$ for any integer m, it follows from the orthogonality of the exponential functions that

$$\begin{array}{rcl} i\alpha\left(\nu;m\right)\hat{\phi}_{1m}-\sum_{n=-\infty}^{\infty}\mathcal{I}_{m,n}\left(q\right)\hat{\phi}_{2n} & = & -i\zeta\hat{\phi}_{1m} \\ -\sum_{n=-\infty}^{\infty}\mathcal{I}_{m,n}\left(q^*\right)\hat{\phi}_{1n}-i\alpha\left(\nu;m\right)\hat{\phi}_{2m} & = & -i\zeta\hat{\phi}_{2m} \end{array}, \tag{3.18}$$

where

$$\mathcal{I}_{m,n}\left(q\right)=\frac{1}{L}\int_{-L/2}^{L/2} qe^{i\mu_{n-m}x}dx. \tag{3.19}$$

Equation (3.18) is a system of infinitely many equations, known as Hill's equations [68]. In order to solve it numerically, we discretize the system. This is done by choosing a grid with N points on the interval $\left[-\frac{L}{2},\frac{L}{2}\right]$, for a large even number N. Let $\Delta x=\frac{L}{N}$, $x_j=j\Delta x$ for $j=-\frac{N}{2},\cdots,\frac{N}{2}-1$. We also use the notation $q_j=q\left(x_j\right)$. The integral $\mathcal{I}_{m,n}\left(q\right)$ is estimated by the sum

$$\mathcal{I}_{m,n}\left(q\right)\approx\frac{1}{L}\sum_{j=-N/2}^{N/2-1} q_j e^{i\mu_{n-m}x_j}\Delta x. \tag{3.20}$$

If we write x_j and Δx in terms of L , N, and j in (3.20), we get

$$\mathcal{I}_{m,n}\left(q\right)\approx\tilde{q}_{n-m},$$

where $\tilde{q}_n$ corresponds to the discrete Fourier transform (DFT), defined as

$$\tilde{q}_n=\frac{1}{N}\sum_{j=-N/2}^{N/2-1} q_j\exp\left(\frac{2\pi ijn}{L}\right),$$

for $-\frac{N}{2} \leq n \leq \frac{N}{2} - 1$. The values of $\tilde{q}_n$ can be calculated by the fast Fourier transform algorithm. Note that the DFT has the property that $\tilde{q}_n = \tilde{q}_{n+aN}$, for any integer a. If we let $m = -\frac{N}{2}, \cdots, \frac{N}{2} - 1$ in (3.18), we arrive at a matrix eigenvalue problem

$$\begin{pmatrix} A & B \\ C & -A \end{pmatrix} \begin{pmatrix} \hat{\boldsymbol{\phi}}_{\mathbf{1}} \\ \hat{\boldsymbol{\phi}}_{\mathbf{2}} \end{pmatrix} = -i\zeta \begin{pmatrix} \hat{\boldsymbol{\phi}}_{\mathbf{1}} \\ \hat{\boldsymbol{\phi}}_{\mathbf{2}} \end{pmatrix}, \tag{3.21}$$

where $\hat{\boldsymbol{\phi}}_p = \begin{bmatrix} \tilde{\phi}_{p,-N/2} & \tilde{\phi}_{p,-N/2+1} & \cdots & \tilde{\phi}_{p,N/2-1} \end{bmatrix}^T$ for $p = 1, 2$, A is the diagonal matrix

$$A = \begin{pmatrix} i\alpha\left(\nu; -\frac{N}{2}\right) & 0 & \cdots & 0 \\ 0 & i\alpha\left(\nu; -\frac{N}{2}+1\right) & \ddots & 0 \\ \vdots & \ddots & \ddots & 0 \\ 0 & \cdots & 0 & i\alpha\left(\nu; \frac{N}{2}-1\right) \end{pmatrix}, \tag{3.22}$$

B is the Toeplitz matrix

$$B = \begin{pmatrix} \tilde{q}_0 & \tilde{q}_{-1} & \cdots & \tilde{q}_1 \\ \tilde{q}_1 & \tilde{q}_0 & \ddots & \vdots \\ \vdots & \ddots & \ddots & \tilde{q}_{-1} \\ \tilde{q}_{-1} & \cdots & \tilde{q}_1 & \tilde{q}_0 \end{pmatrix}, \tag{3.23}$$

and

$$C = B^*. \tag{3.24}$$

The first row of the matrix B is given by

$$\begin{bmatrix} \tilde{q}_0 & \cdots & \tilde{q}_{-N/2} & \tilde{q}_{N/2-1} & \tilde{q}_{N/2-2} & \cdots & \tilde{q}_1 \end{bmatrix},$$

and the matrix B^* is the complex conjugate of B. Hill's method amounts to the calculation of the eigenvalues of the matrix (3.21) for different values of $\nu \in \left[0, \frac{\pi}{L}\right]$.

The convergence criteria of Hill's method are still a work in progress. Numerical evidence was supplied for many problems, see for example [38]. There are also some cases where the

results diverge, as is shown in [26]. Convergence was proved for self-adjoined operators by Curtis and Deconinck [37]. Johnson and Zumbrun [56] proved convergence for a class of operators of the form

$$L = \sum_{j=0}^{m} \left(\frac{\partial}{\partial x} \right)^{j} a_j, \tag{3.25}$$

where the matrix a_m is positive definite, and the matrices a_j are periodic for $j = 0, \cdots, m$, i.e. $a_j(x + X) = a_j(x)$. The class of operators (3.25) include nonselfadjoint operators. The periodic ZS eigenvalue falls outside the class of the Johnson-Zumbrun operators (3.25), since the matrix $a_m = a_1$ is not positive definite. However, our numerical results indicate that Hill's method converges for the periodic ZS eigenvalue problem as is clear from the results in the next section.

3.3 Large interval limit $(L \to \infty)$ of periodic ZS eigenvalue problem

The aim of this chapter is to develop a numerical method that will allow us to study the behaviour of the discrete spectrum of the ZS eigenvalue problem associated with decaying potentials defined on the real line $q(x) \in L^2(\mathbb{R})$. The discrete spectrum of the ZS eigenvalue problem (3.3) in the upper half of the complex plane is defined as

$$\sigma_d(\mathcal{L}^x) := \left\{ \zeta \in \mathbb{C},\ \mathrm{Im}\zeta > 0 \,\middle|\, \mathbf{v}(x) \sim \begin{bmatrix} 0 \\ 1 \end{bmatrix} e^{i\zeta x} \text{ as } x \to \infty,\ \mathbf{v}(x) \sim \begin{bmatrix} 1 \\ 0 \end{bmatrix} e^{-i\zeta x} \text{ as } x \to -\infty \right\}. \tag{3.26}$$

The continuous spectrum consists of the entire real line, while the discrete spectrum consists of a finite number of pairs of complex conjugates in the complex plane. In order to obtain a numerical scheme to calculate the discrete spectrum (3.26), we propose the truncation of the interval of x to a large but finite interval. This is done by reducing the interval to

$x \in \left[-\frac{L}{2}, \frac{L}{2}\right]$, and imposing periodic boundary conditions. The truncated potential $\tilde{q}$ becomes

$$\tilde{q}(x) = \begin{cases} q(x) & \text{for } x \in \left[-\frac{L}{2}, \frac{L}{2}\right] \\ q(x+L) = q(x) & \text{for all } x \end{cases} . \tag{3.27}$$

The spectrum of the resulting periodic ZS eigenvalue problem is then calculated through Hill's method.

The ZS eigenvalue problem changes significantly when periodic boundaries are imposed. It is obvious from the Floquet form of the eigenfunctions (3.7) that, in the periodic setting, no discrete eigenvalues of the form (3.26) exist. Instead, the spectrum of the periodic problem arises as line segments in the complex plane. These line segments form due to the symmetry of the Floquet exponents. The convergence of the truncation of the interval was studied in 1997 by Gardner [47]. He proved that, for any fixed Floquet exponent, the continuous spectrum converges to the discrete spectrum of the unbounded potential as the interval length $L \to \infty$. He also proved that, in the limit, the multiplicities of eigenvalues are preserved and that no spurious eigenvalues are formed. Therefore, provided that Hill's method converges and that the length of truncation L is sufficiently large, the continuous spectrum of the truncated ZS eigenvalue problem is contained in a δ-neighbourhood of the discrete eigenvalue of the homoclinic orbit.

This leads us to the question: is there a specific choice of Floquet exponent that converges fastest? We propose the use of a specific Floquet exponent ν_c, reported by the author, Herbst and Molchan in [81] to give the fastest convergence, where

$$\nu_c = \frac{\pi}{2L}. \tag{3.28}$$

We have no analytical justification for this conjecture. However, the method provides the best estimate in numerous problems, while producing no spurious eigenvalues, as is demonstrated shortly. The rest of this chapter is devoted to provide numerical evidence in favour of this

conjecture.

For our first example, consider the following class of decaying potentials

$$q(x) = A\text{sech}(x). \tag{3.29}$$

The discrete spectrum for these potentials were calculated analytically by Satsuma and Yajima [90], and are given by

$$\sigma_d = \{\pm\zeta_1, \pm\zeta_2, \cdots, \pm\zeta_M\}, \tag{3.30}$$

where

$$\zeta_j = i\left(A + \frac{1}{2} - j\right), \quad j = 1, \ldots, M, \tag{3.31}$$

and where M is the largest integer satisfying

$$M < A + \frac{1}{2}. \tag{3.32}$$

It follows that there are no discrete eigenvalues for $A \leq 0.5$, while the first complex conjugate pair of eigenvalues occurs as A is increased beyond $A = 0.5$. For $A = 0.52$, the eigenvalue pair is given by $\zeta = \pm 0.02i$.

Figures 3.1 (a) and (b) show the numerical results for $A = 0.48$ and $A = 0.52$ respectively, where an interval length $L = 60$ and $N = 256$ Fourier modes are used. The lines represent the continuous spectrum (of the periodic problem), calculated by uniform samples of the Floquet exponent in the interval $\nu \in \left[0, \frac{\pi}{L}\right]$. Note that there is no marked difference between the line segments in (a) and (b). In addition the dots, corresponding to the discrete spectrum of the periodic problem, i.e. $\nu = 0,$ and $\nu = \pi/L$ have no counterpart in the spectrum of the homoclinic orbit. Indeed, they bear little if any relation to the discrete eigenvalue of the homoclinic orbit, and produce multiple spurious eigenvalues. In contrast, the eigenvalues obtained by choosing $\nu = \nu_c$ of (3.28), indicated with crosses, produce much better results. In (a) all these points lie on the real line, corresponding to the continuous spectrum of the

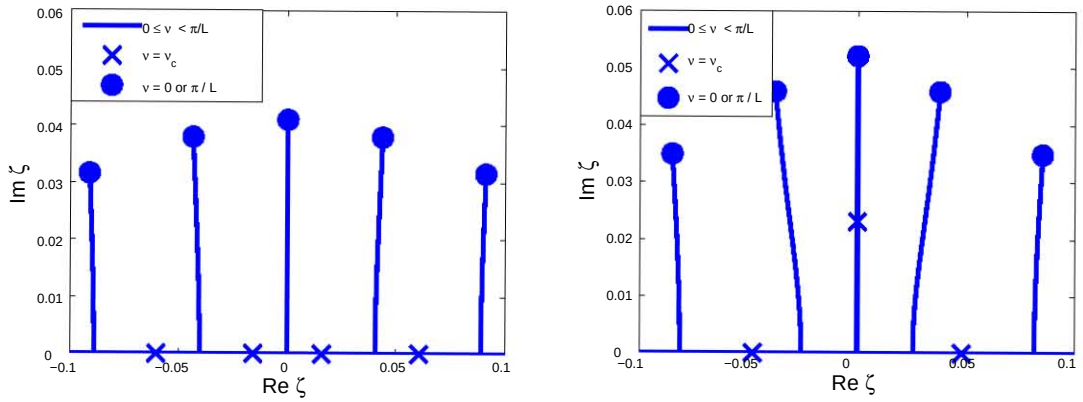

(a) (b)

Figure 3.1: *Numerical results for the potentials* (3.29) *with* $L = 60$. *(a)* $A = 0.48$. *(b)* $A = 0.52$.

homoclinic orbit. In (b) one eigenvalue lies on the imaginary axis, close to the eigenvalue of the homoclinic orbit, $\zeta = 0.02i$. The rest of the eigenvalues lie on the real line, and thus no spurious eigenvalues are calculated when ν_c is used.

It is now easy to visualize what happens if the amplitude A in (3.29) is increased from $A = 0.48$ to $A = 0.52$. The discrete eigenvalues marked by crosses on the real axis, corresponding to $\nu = \nu_c$, move closer to the origin. For $A = 0.5$ the two values on either side of the origin in Figure 3.1 (a) form a double value at the origin. If A is further increased, they split into a complex conjugate pair. A further increase in A move them away from the origin on the imaginary axis while the next two on the real axis move closer to the origin, also splitting into complex conjugate pairs as A is increased beyond $A = 1.5$.

It should be noted that, for potentials of the form (3.29), an alternative numerical approach [38] is to approximate the sech function not by truncation, but by the periodic function $\mathrm{cn}\,(x, k)$ with $k \to 1$ ($L \to \infty$). We only consider truncated potentials of the form (3.27) since we are primarily interested in potentials defined on the real line. In Figure 3.2 the continuous spectrum is shown for the truncated potential (3.29) with $A = 0.52$. Here we use $N = 512$ Fourier modes to calculate the spectrum. Note that the scales in Figures 3.2 (a) to (c) are larger than the scales in (d) to (h). In Figure 3.2 (a), we see that, for $L = 60$, the continuous

spectrum consists of a series of line segments, each connected to the real line. For larger L the two segments adjacent to the imaginary axis approach the imaginary axis to join at the origin for $L = 102.7$, as shown in Figure 3.2 (b). As the interval length is increased further, these two pieces move up the imaginary axis to form the pitchfork shape seen in Figure 3.2 (c). As L increases further, the two outer segments start to decrease, moving closer to the imaginary axis, as shown in Figures 3.2 (d) and (e). Figure 3.2 (f) shows the spectrum for $L = 317.8$, where the two line segments collide on the imaginary axis. With a further increase in L, a gap on the imaginary axis opens up, with the upper part receding towards the eigenvalue of the homoclinic orbit at $\zeta = 0.02i$, as is shown in Figure 3.2 (g) and (h).

It is only after the gap on the imaginary axis forms that the spectrum becomes isolated clearly demonstrating Gardner's results. Of particular interest is the discrete eigenvalues calculated using the Floquet exponent ν_c, indicated by crosses in Figure (3.2). Note that these values accurately predict the discrete eigenvalue for the homoclinic orbit, long before the spectrum is isolated and Gardner's results are applicable.

The next issue we address is the rate of convergence of the choice of Floquet exponent $\nu_c = \frac{\pi}{2L}$ as L is increased. In particular we want to establish the fact that this choice of Floquet exponent converges faster to the discrete eigenvalue than other choices. To show this, we consider the potential (3.29) with $A = 2$, i.e. $q(x) = 2\text{sech}x$. This is the initial condition for a breather solution with two eigenvalues in the upper half of the complex plane at $\zeta = 0.5i$ and $\zeta = 1.5i$. In this experiment, we fix the number of Fourier modes $N = 128$ for increasing values of L. Figure 3.3 shows the error, given by $\text{Im}(\zeta_n - \zeta_a)$, where ζ_n is the numerically calculated eigenvalue, and ζ_a is analytical eigenvalue. The solid line shows the error when the Floquet exponent $\nu = \nu_c$ is used to find ζ_n. The dashed lines show the errors when Floquet exponents $\nu_\pm$ are used, where

$$\nu_\pm = (1 \pm \epsilon) \times \nu_c, \tag{3.33}$$

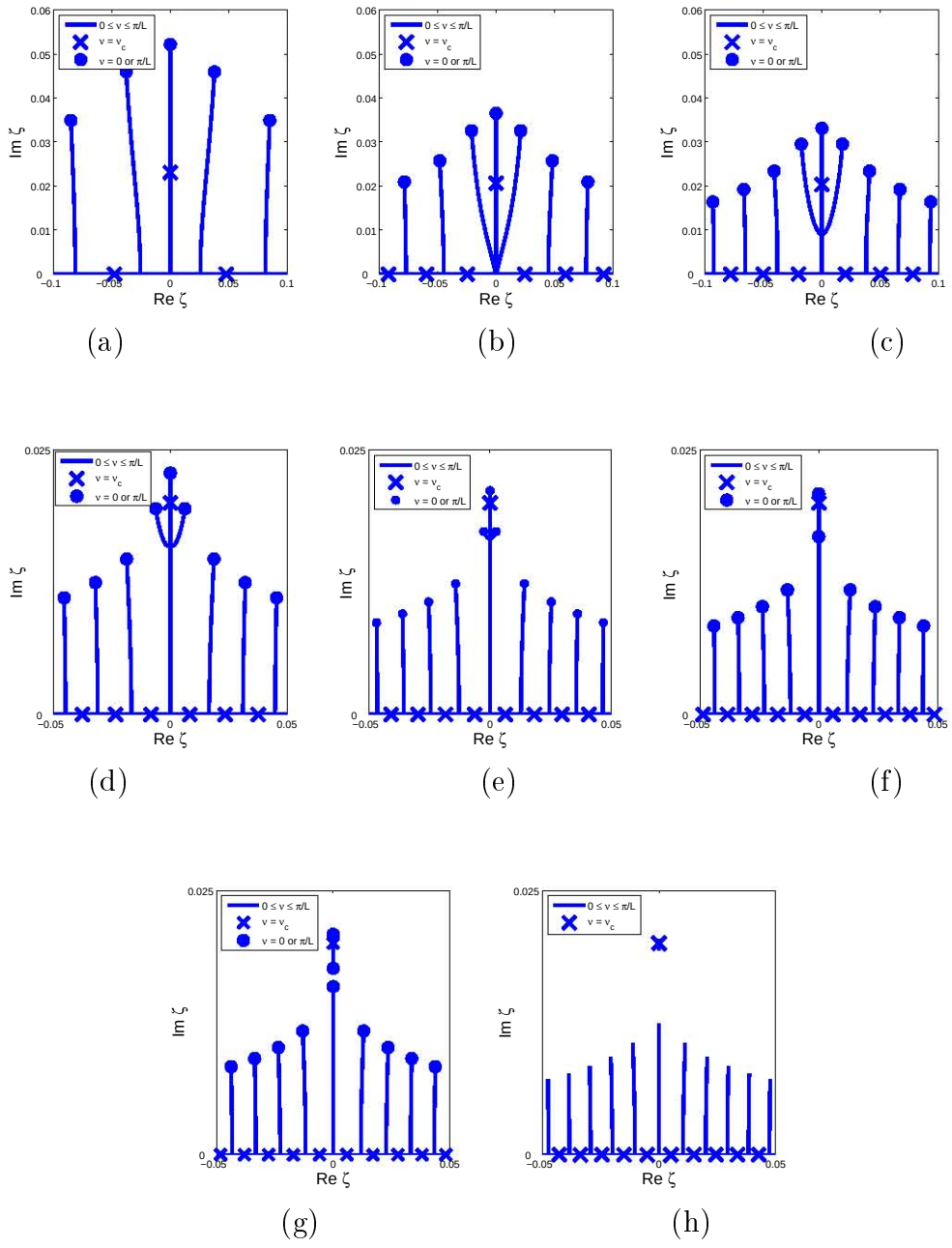

Figure 3.2: *Numerical results for the potentials* (3.29) *with* $A = 0.52$. *(a)* $L = 60$. *(b)* $L = 102.7$ *(c)* $L = 120$. *(d)* $L = 240$. *(e)* $L = 300$. *(f)* $L = 317.8$ *(g)* $L = 320$. *(h)* $L = 360$.

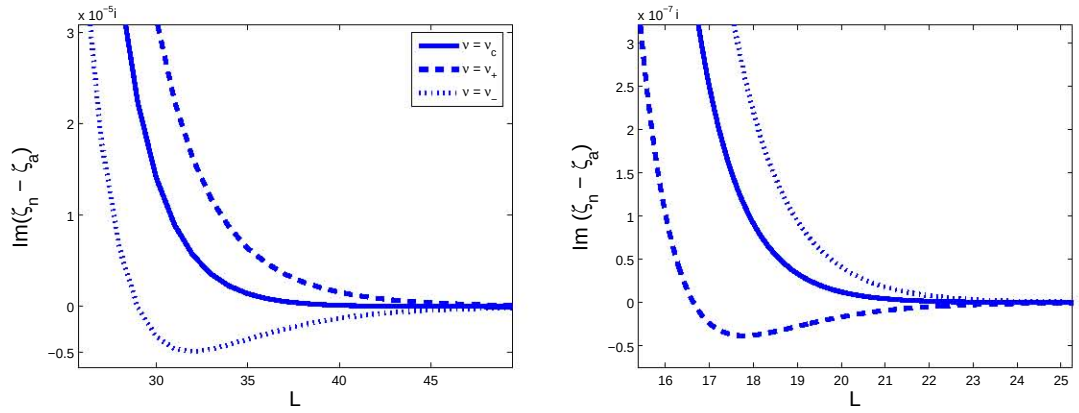

(a) (b)

Figure 3.3: *Errors for the potential* $q(x) = 2sechx$ *for different values of* L. *Here* ζ_n *corresponds to the numerically calculated eigenvalues, and* ζ_a *corresponds to the analytical eigenvalues. The solid, dashed and dotted lines correspond to Floquet exponents* $\nu = \nu_c, \nu_+\nu_-$ *respectively, used to calculate* ζ_n. *(a)* $\zeta_a = 0.5i$. *(b)* $\zeta_a = 1.5i$.

and $\epsilon = 0.01$. For both eigenvalues $\zeta = 0.5i$ and $\zeta = 1.5i$, we see that the proposed Floquet exponent converges somewhat faster than the other choices.

Our next numerical example is a class of super Gaussian potentials given by

$$q(x) = Ae^{-x^{2M}} \text{for } M = 1, 2, 3, \cdots . \tag{3.34}$$

The potentials (3.34) are real, square integrable functions that are monotonically increasing for $x < 0$ and monotonically decreasing for $x > 0$. Therefore they satisfy the criteria for the single lobe theorem [62]. The theorem states that all eigenvalues of (3.34) must be purely imaginary. In addition, the number of eigenvalues are given by

$$N = \left\lfloor \frac{1}{2} + \frac{1}{\pi} \int_{-\infty}^{\infty} q(x)\, dx \right\rfloor, \tag{3.35}$$

where $\lfloor x \rfloor$ is the integer part of x. This implies that new eigenvalues are created on the imaginary axis whenever

$$A = (2N - 1)\, A_c, \tag{3.36}$$

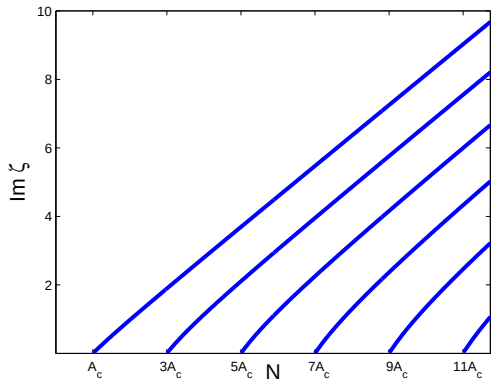

Figure 3.4: *Imaginary part of eigenvalues for Gaussian potentials* (3.34) *where* $M = 1$.

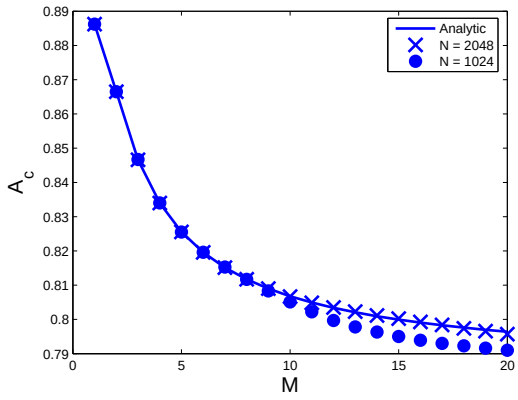

Figure 3.5: *Critical amplitudes of super Gaussian potentials*

for $N = 1, 2, \cdots$, where

$$A_c = \left[\frac{4}{\pi}\Gamma\left(1 + \frac{1}{2M}\right)\right]^{-1}. \tag{3.37}$$

In Figure 3.4 we show the numerical results for Gaussian potentials, i.e. (3.34) for $M = 1$. We calculate the eigenvalues for amplitudes $0 \leq A \leq 12A_c$, where $A_c = \frac{\sqrt{\pi}}{2}$, using an interval length $L = 100$, $N = 1024$ Fourier modes, and Floquet exponent $\nu = \nu_c$. Note that these potentials cannot be approximated by simple periodic functions, as was the case for the sech potentials, and one is therefore left no choice but to truncate. Figure 3.4 shows that eigenvalues are created at $A_c, 3A_c, \cdots, 11A_c$, in agreement with the analytical result (3.36).

We also calculated the critical amplitude A_c numerically for super Gaussian potentials (3.34) with $M \leq 20$, using an interval length $L = 100$, and Floquet exponent $\nu = \nu_c$. The

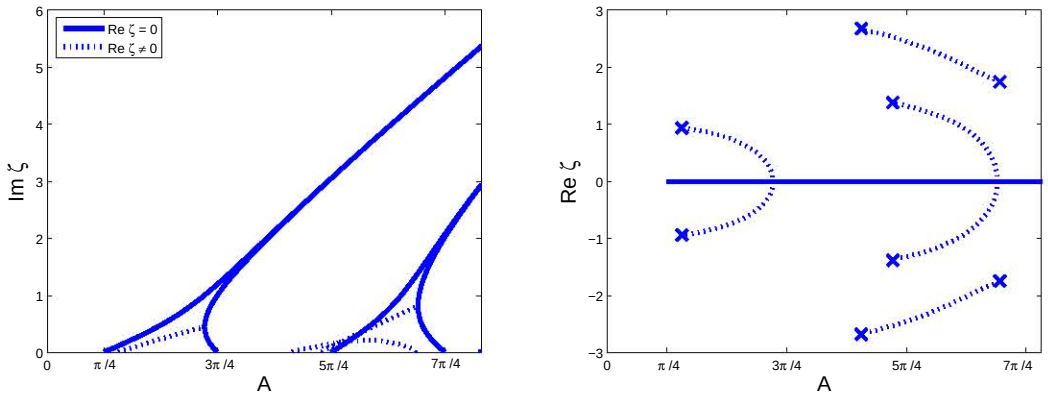

(a) (b)

Figure 3.6: *Spectrum of the two rectangular pulse. In (a), the imaginary parts of the eigenvalues are shown. In (b) the real parts of the eigenvalues are shown. The 'x' points in (b) indicates the points where complex eigenvalues are born or annihilated.*

results are shown in Figure 3.5. The solid line represents the analytical result (3.37). The dots show the numerically calculated critical amplitudes for $N = 1024$ Fourier modes, while the crosses show the critical amplitudes for $N = 2048$ Fourier modes. Once again the numerical results are in good agreement with the analytical results, in particular for $N = 2048$ Fourier modes. Indeed, for $M \geq 10$, more Fourier modes are required to produce accurate results of Hill's method, since the slope of the super Gaussian potentials increases as M is increased.

As a final example, we consider a class of double rectangle potentials, given by

$$q(x) = Ar_2(x), \tag{3.38}$$

where

$$r_2(x) = \begin{cases} 1 \text{ if } 1 \leq |x| \leq 2 \\ 0 \text{ otherwise} \end{cases}. \tag{3.39}$$

For this potential, the single lobe theorem no longer guarantees only purely imaginary eigenvalues. In [1], Abdullaev and coworkers derived an analytical expression for the discrete spectrum of potentials of the form (3.38). Desaix and coworkers [40] factorized this formula to find critical amplitudes where eigenvalues appear or disappear. They showed that crit-

ical amplitudes, where purely imaginary eigenvalues are born or annihilated, are given by equation (3.36), where $A_c = \frac{\pi}{4}$. They also showed that complex eigenvalues are born or annihilated on the real line when

$$A = |\xi/\sin 2\xi|\,, \tag{3.40}$$

where $\xi \in \mathbb{R}$ satisfies the equation

$$\cot\left[\xi\sqrt{1+\operatorname{cosec}^2(2\xi)}\right] + \frac{\cot(2\xi)}{\sqrt{1+\operatorname{cosec}^2(2\xi)}} = 0. \tag{3.41}$$

In Figure 3.6 the numerical results are shown for $0 \leq A \leq 5.7$. In (a) the imaginary parts of the eigenvalues are shown. We used a solid line to indicate purely imaginary eigenvalues, and a dotted line to indicate eigenvalues in the complex plane. In (a) we see that purely imaginary eigenvalues are born at amplitudes A_c and $5A_c$, while purely imaginary eigenvalues are annihilated at amplitudes $3A_c$ and $7A_c$. This agrees well with the analytic results. In (b) the numerical results for the real parts of the eigenvalues are shown with the solid lines. The crosses indicate the amplitudes and real parts where complex eigenvalues are born or annihilated, according to equations (3.40) and (3.41). We see that the numerical results are in good agreement with the analytical results.

3.4 Concluding remarks

In this chapter we developed a numerical method to calculate the discrete spectrum of the Zakharov-Shabat eigenvalue problem for decaying potentials on the real line. To do this, the potential is truncated, and treated as a periodic potential, resulting in an auxiliary eigenvalue problem, namely the periodic ZS eigenvalue problem. To solve the auxiliary eigenvalue problem, the Hill's method is applied, developed by Deconinck and Kutz [38]. Numerical results show that, as the interval of truncation is increased, the spectrum of the auxiliary problem converges to the spectrum of the original problem, albeit in a complicated

way. It is also found that the rate of convergence depends on the choice of Floquet exponent. The Floquet exponent that produces the optimal rate of convergence is predicted based on numerical evidence [81]. This allows us to accurately calculate the discrete spectrum through the calculation of a single matrix eigenvalue problem. In Chapter 5 we use this to calculate the time evolution of the discrete spectrum of a perturbed NLS system, namely the parametrically driven nonlinear Schrödinger (PDNLS) equation. In order to do this, we first need to solve the PDNLS equation numerically. To do this, we develop the split-step method in Chapter 4.

Chapter 4

The split-step method for the PDNLS equation

Numerical simulation plays a vital role in the study of nonlinear partial differential equations. For example, in the development of soliton theory, numerical experiments played a foundational role. Fermi, Pasta and Ulam (FPU) [43] studied a nonlinear lattice problem numerically in 1955. Contrary to their expectations, the experioments revealed that the effect of nonlinearity is not to leak energy to higher order modes. They used direct simulation to confirm their results. Zabusky and Kruskal [111] investigated the FPU in the continuum limit by studying the KdV equation. The results of numerical simulation were responsible for their discovery of the reflectionless collision property of solitons. These results paved the way for the development of modern soliton theory.

The split-step method is frequently used in the direct simulation of NLS-type equations. For the NLS equation, the method was first implemented in 1973 by Hardin and Tappert [49]. Taha and Ablowitz [96] compared the split-step method to a number of finite difference schemes, including the integrable finite difference scheme developed earlier by Ablowitz and Ladik [5, 6]. They showed that the split-step method is best scheme in terms of efficiency, i.e. computational speed. In 1988, Neri [78] derived a fourth-order accurate symplectic

split-step method. Forest and Ruth [45] showed that the fourth-order split-step method can be generalized, and derived the method by means of the Campbell-Baker-Hausdorf (CBH) formula in 1990. In the same year, Yoshida [110] constructed a method, using the CBH formula, to construct symplectic schemes of any even order. Since then, the split-step method has been implemented to many NLS-type equations, such as the complex Ginzburg-Landau equation [12], generalized NLS equations [77], and higher-dimensional NLS equations [9].

In this chapter we develop two numerical schemes for solving the PDNLS equation. In Section 4.1 a fourth-order pseudo-spectral Runge-Kutta method is developed. In Sections 4.2 - 4.4 a fourth-order split-step scheme is developed, based on Bondila [24]. The chapter is concluded in Section 4.5 where we compare the two methods to show that the split-step method is the faster of the two. We also comment on the stability of the two methods.

4.1 The pseudo-spectral Runge-Kutta method

The Runge-Kutta method is often employed for the integration of systems of ordinary differential equations. To apply the method to the PDNLS equation,

$$i\psi_t + \psi_{xx} + 2|\psi|^2\psi - \psi = h\psi^* - i\gamma\psi, \tag{4.1}$$

one has to reduce the PDNLS to a system of ODE's by truncating and discretizing the spatial domain. We do this by truncating the spatial domain to the interval $x \in [0, L]$ for a large, but finite L. On this interval, we define a grid with N points, $x_0, x_1, \cdots, x_{N-1}$, where $x_j = j \times \Delta x$ and $\Delta x = \frac{L}{N}$. The points on the grid is defined by $\psi_j(t) = \psi(x_j, t)$ for $j = 0, 1, \cdots, N-1$.

An important step in the discretization of the PDNLS is to approximate the spatial derivative term, ψ_{xx}, in terms of the points on the grid. To accomplish this, we note that, after the truncation of the spatial interval, we can express the function $\psi(x, 0)$ as a Fourier

series,

$$\psi(x,t) = \sum_{n=-\infty}^{\infty} \hat{\psi}_n(t)\, e^{2\pi i n x/L}, \tag{4.2}$$

where

$$\hat{\psi}_n(t) = \frac{1}{L}\int_0^L \psi(x,t)\, e^{-2\pi i n x/L} dx. \tag{4.3}$$

The second derivative of (4.2) is formally given by

$$\psi_{xx}(x,t) = \sum_{n=-\infty}^{\infty} -\left(\frac{2\pi n}{L}\right)^2 \hat{\psi}_n(t)\, e^{2\pi i n x/L}. \tag{4.4}$$

After discretization, if we substitute $x_j = j \times \frac{L}{N}$ into the sum 4.4, we get $\psi_{xx}(x_j) \approx \tilde{\psi}_j$, where

$$\tilde{\psi}_j(t) \approx \sum_{n=-N/2}^{N/2-1} -\left(\frac{2\pi n}{L}\right)^2 \Psi_n(t)\, e^{2\pi i n x/L}. \tag{4.5}$$

Here $\Psi_n(t) \approx \hat{\psi}_n(t)$ is the discretized Fourier coefficient, given by

$$\Psi_n(t) = \frac{1}{L}\sum_{j=0}^{N-1} \psi_j(t)\, e^{-2\pi i n x_j/L} \Delta x. \tag{4.6}$$

If we substitute $x_j = jL/N$ and $\Delta x = L/N$ into the sum (4.6), we get

$$\Psi_n = \frac{1}{N}\sum_{j=-N/2}^{N/2-1} \psi_j(t)\, e^{-2\pi i j n/N}. \tag{4.7}$$

This leads us to a discretized system of ODE's, given by

$$\dot{\psi}_j = i\tilde{\psi}_j + 2i\left|\psi_j\right|^2 \psi_j - i\psi_j - ih\psi_j^* - \gamma\psi_j \tag{4.8}$$

for $j = 0, 1, \cdots, N-1$. Equations (4.7) and (4.5) are well-known definitions of the discrete Fourier transform (DFT) and the inverse discrete Fourier transform (IDFT) respectively. These mappings can be efficiently calculated by means of the fast Fourier transform (FFT),

an efficient algorithm that was developed by Cooley and Tukey [36].

Finally, we integrate the system of ODE's (4.8), using the fourth-order Runge-Kutta method. The formula is given by

$$\psi_j(\tau) = \psi_j(0) + \frac{1}{6}(k_1 + 2k_2 + 2k_3 + k_4),$$

where

$$k_1 = \tau g(\psi_j),$$

$$k_2 = \tau g\left(\psi_j + \frac{1}{2}k_1\right),$$

$$k_3 = \tau g\left(\psi_j + \frac{1}{2}k_2\right),$$

and

$$k_4 = \tau g(\psi_j + k_3).$$

The function g is defined by the right-hand side of equation (4.8), i.e.

$$g(\psi_j) = i\tilde{\psi}_j + 2i|\psi_j|^2\psi_j - i\psi_j - ih\psi_j^* - \gamma\psi_j.$$

There are three sources of errors, namely the error associated with the discretization of the system, the error incurred with the use of the DFT to estimate the spatial derivative term, and the error incurred when integrating the system of ODE's. Provided that the spatial structure of the solution, ψ, is sufficiently smooth, it can be shown that the error of discretization, as well as the aliasing error associated with the discrete Fourier transform, is exponentially small (see for example [97, 28]). Since $|\psi| \to 0$ as $|x| \to 0$, this smoothness is guaranteed, provided that the interval length L, and the number of grid points N, are sufficiently large. Therefore, the largest part of the error is incurred by the time integration, resulting in an error of $\mathrm{O}(\tau^5)$.

4.2 First-order split-step scheme

The PDNLS can be written in the form

$$\psi_t = (L + N)\,\psi, \tag{4.9}$$

where the operators L and N are defined by

$$L\psi = i\psi_{xx} - i\psi - ih\psi^* - \gamma\psi, \tag{4.10}$$

and

$$N\psi = 2i\,|\psi|^2\,\psi. \tag{4.11}$$

The formal solution of (4.9) at $t = \tau$ is given by

$$\psi\,(x,\tau) = e^{(L+N)\tau}\psi\,(x,0)\,, \tag{4.12}$$

where the exponential operator is defined by

$$e^A = I + A + \frac{1}{2!}A^2 + \frac{1}{3!}A^3 + \cdots\,. \tag{4.13}$$

The solution (4.12) can be "split" by writing the formal solution (4.12) as the product of two exponential operators,

$$e^{(L+N)\tau}\psi\,(x,0) \approx e^{L\tau}e^{N\tau}\psi\,(x,0)\,. \tag{4.14}$$

The "split" operator on the right hand side of equation (4.14), $e^{L\tau}e^{N\tau}$, is not equivalent to the original operator, $e^{(L+N)\tau}$. This is verified by expressing each operator as a Taylor series

(4.13). The operator $e^{(L+N)\tau}$ becomes

$$e^{(L+N)\tau} = I + \tau (L+N) + \frac{\tau^2}{2}\left(L^2 + LN + NL + N^2\right) + \mathbb{O}\left(\tau^3\right), \tag{4.15}$$

while the Taylor series for the "split" operator $e^{L\tau}e^{N\tau}$ is given by

$$e^{L\tau}e^{N\tau} = I + \tau (L+N) + \frac{\tau^2}{2}\left(L^2 + 2LN + N^2\right) + \mathrm{O}\left(\tau^3\right). \tag{4.16}$$

From these expansions, it follows that the exponential operators are only equivalent when the operators L and N commute, i.e. $LN = NL$. One can easily check that L and N, defined in (4.10) and (4.11) respectively, do not commute. A comparison between the Taylor series of the solution (4.15) and the Taylor series of the split operator (4.16) shows that the latter operator coincides with the former operator in the first order of τ. In other words, the accuracy of the splitting is of $\mathrm{O}(\tau)$.

The solution of the right hand side of (4.14) is equivalent to solving two equations. Firstly, let $\tilde{\psi}(x,\tau)$ be the intermediate solution, defined by

$$\tilde{\psi}(x,\tau) = e^{N\tau}\psi(x,0). \tag{4.17}$$

Equation (4.17) is the formal solution of the initial value problem

$$\begin{aligned} \tilde{\psi}_t &= 2i\left|\tilde{\psi}\right|^2\tilde{\psi}, \\ \tilde{\psi}(x,0) &= \psi(x,0) \end{aligned} \tag{4.18}$$

at $t = \tau$. Since $\left(|\psi|^2\right)_t = 0$ in (4.18), the intermediate solution is given by

$$\tilde{\psi}(x,\tau) = \psi(x,0)\, e^{2i|\psi(x,0)|^2\tau}. \tag{4.19}$$

Substitution of (4.19) into equation (4.14) then gives the first-order split-step scheme

$$\psi(x,\tau) = e^{L\tau}\tilde{\psi}(x,\tau). \tag{4.20}$$

Equation (4.20) is the formal solution of the equation $\psi_t = L\psi$ at $t = \tau$, i.e.

$$\begin{aligned} \psi_t &= i\psi_{xx} - i\psi - ih\psi^* - \gamma\psi \\ \psi(x,0) &= \tilde{\psi}(x,\tau). \end{aligned} \tag{4.21}$$

Since the operator (4.21) is linear, one can solve it by using Fourier theory. To solve the linear equation, we write the solution in the form

$$\psi(x,\tau) = e^{-\gamma\tau} f(x,\tau), \tag{4.22}$$

where $f(x,t)$ is a complex function. If we substitute this into the equation (4.21), we get

$$f_t + f_{xx} - f - hf^* = 0. \tag{4.23}$$

Separating the real and imaginary parts of f, we get the following system of equations:

$$\begin{aligned} -b_t + a_{xx} - a + ha &= 0 \\ a_t + b_{xx} - b + hb &= 0 \end{aligned}, \tag{4.24}$$

where $f(x,t) = a(x,t) + ib(x,t)$ for the real functions a and b.

From a numerical perspective, one has to truncate the spatial interval to a finite interval

$x \in [0, L]$. After truncation, one can expand the functions a and b in Fourier series,

$$\begin{aligned} a(x,t) &= \sum_{n=-\infty}^{\infty} A_n(t)\, e^{2\pi i n x/L} \\ b(x,t) &= \sum_{n=-\infty}^{\infty} B_n(t)\, e^{2\pi i n x/L} \end{aligned}, \tag{4.24}$$

where

$$\begin{aligned} A_n(t) &= \tfrac{1}{L}\int_0^L a(x,t)\, e^{-2\pi i n x/L} \\ B_n(t) &= \tfrac{1}{L}\int_0^L b(x,t)\, e^{-2\pi i n x/L} \end{aligned}.$$

Note that, by applying the Fourier series, periodic boundary conditions are imposed.

If we substitute the Fourier series into the system (4.24) we get

$$\begin{aligned} \dot{B}_n &= -\left(k_n^2 + 1 + h\right)\dot{A}_n \\ \dot{A}_n &= \left(k_n^2 + 1 - h\right)\dot{B}_n \end{aligned} \tag{4.25}$$

for $n = 0, \pm 1, \pm 2, \cdots$. The solution of equation (4.25) is given by

$$\begin{aligned} A_n(\tau) &= A_n(0)\cos\omega_n\tau + \alpha_n B_n(0)\sin\omega_n\tau \\ B_n(\tau) &= B_n(0)\cos\omega_n\tau - \alpha_n^{-1} A_n(0)\sin\omega_n\tau \end{aligned}, \tag{4.26}$$

for $h^2 < \left(1 + k_n^2\right)^2$, and

$$\begin{aligned} A_n(\tau) &= \tfrac{A_n(0) - \alpha_n B_n(0)}{2} e^{\omega_n\tau} + \tfrac{A_n(0) + \alpha_n B_n(0)}{2} e^{-\omega_n\tau} \\ B_n(\tau) &= \tfrac{B_n(0) - \alpha_n^{-1} A_n(0)}{2} e^{\omega_n\tau} + \tfrac{B_n(0) + \alpha_n^{-1} A_n(0)}{2} e^{-\omega_n\tau} \end{aligned}, \tag{4.27}$$

for $h^2 > \left(1 + k_n^2\right)^2$. Here $k_n = 2\pi n/L$, $\omega_n = \left|\left(1 + k_n^2\right)^2 - h^2\right|^{1/2}$ and $\alpha_n = \left|\frac{1 + k_n^2 - h}{1 + k_n^2 + h}\right|^{1/2}$.

Since the functions $a(x,t)$ and $b(x,t)$ are real, the Fourier coefficients satisfy

$$A_n(t) = A^*_{-n}(t), \quad B_n(t) = B^*_{-n}(t). \tag{4.28}$$

Moreover, the Fourier coefficients of the functions $a(x,t)$ and $b(x,t)$ can be expressed in terms of the Fourier coefficients of the function $f(x,t)$ through the identities

$$A_n(t) = \frac{F_n(t) + F^*_{-n}(t)}{2}, \quad B_n(t) = \frac{F_n(t) - F^*_{-n}(t)}{2i}, \tag{4.29}$$

where

$$F_n(t) = \frac{1}{L}\int_0^L f(x,t)\, e^{-2\pi i n x/L}, \tag{4.30}$$

satisfying

$$f(x,t) = \sum_{n=-\infty}^{\infty} F_n(t)\, e^{2\pi i n x/L}. \tag{4.31}$$

Therefore, using the Fourier coefficients $F_{\pm n}(t)$ of the complex function $f(x,t)$, one can calculate the Fourier coefficients $A_{\pm n}(t)$ and $B_{\pm n}(t)$ of the real and imaginary part of $f(x,t)$ respectively.

In order to calculate the Fourier coefficients F_n numerically, we need to discretize the spatial interval. This is done by choosing N points $x_0, x_1, \cdots, x_{N-1}$, where $x_j = j \times \Delta x$ with a step size $\Delta x = \frac{L}{N}$ for $n = -N/2, \cdots, N/2-1$. We define the notation $f_j(t) = f(x_j, t)$. We use a truncated Fourier series to estimate the Fourier series (4.31), given by

$$f_j(t) = \sum_{n=-N/2}^{N/2-1} F_n(t)\, e^{2\pi i j n/N}. \tag{4.32}$$

To calculate the Fourier coefficients, we estimate the integral (4.30) through the finite sum

$$\begin{aligned} F_n(t) &= \frac{1}{L}\sum_{j=0}^{N-1} f_j(t)\, e^{-2\pi i n x_j/L}\Delta x \\ &= \frac{1}{N}\sum_{j=0}^{N-1} f_j(t)\, e^{-2\pi i j n/N} \end{aligned} . \tag{4.33}$$

The fast Fourier transform (FFT) can be used to evaluate the sum (4.33), and the inverse fast Fourier transform (IFFT) can be used to evaluate the sum (4.32). Note that the DFT has the identity $F_{n+N}(t) = F_n$ for all n. Therefore, by using the identity $F_{N/2}(t) = F_{-N/2}(t)$, it follows that

$$A_{-N/2}(t) = F_{-N/2}(t) \tag{4.34}$$

and

$$B_{-N/2}(t) = 0. \tag{4.35}$$

To summarize, the first-order split-step method consists of five steps:

- Discretize the interval $x \in [0, L]$, let $x_j = j \times \frac{L}{N}$, and let $\psi_j(t) = \psi(x_j, t)$ for $j = 0, 1, \cdots, N-1$.
- Calculate the intermediate solution $\tilde{\psi}_j(\tau)$ from $\psi_j(0)$ using the solution (4.19).
- Use the transformation (4.22) and the FFT to calculate the Fourier coefficients $F_{-N/2}(0), F_{-N/2+1}(0),$
- Use equations (4.26) - (4.29) and (4.34) - (4.35) to calculate the evolved Fourier coefficients $F_{-N/2}(\tau), F_{-N/2+1}(\tau), \cdots, F_{N/2-1}(\tau)$
- Use the IFFT and the transformation (4.22) to calculate the solution $\psi_0(\tau), \psi_1(\tau), \cdots, \psi_{N-1}(\tau)$.

The bulk of the computational time is spent on the calculation of the FFT in step 2 and the IFFT in step 5.

For the split-step scheme described above, there are two sources of errors, namely *1)* the splitting of the operator (4.12) into the operator (4.14) and *2)* the truncation and discretiza-

tion of the spatial grid to solve the linear PDE (4.21). The error incurred by the truncation and discretization is exponentially small, as in the case of the fourth-order pseudo-spectral Runge-Kutta method. Therefore, the error consists mainly from the time splitting, producing an error of $\mathrm{O}(\tau^2)$, as follows from (4.15) and (4.16) and the subsequent discussion in Section 4.1. Therefore, the method is $\mathrm{O}(\tau)$, as is claimed in the title of this section.

4.3 Second-order split-step method

To construct a second order accurate scheme, we write the formal solution of the PDNLS equation as

$$\psi(x,\tau) = e^{[(c_1+c_2)N+(d_1+d_2)L]\tau}\psi(x,0),$$

where $c_1 + c_2 = d_1 + d_2 = 1$. We then split the equation as

$$\psi(x,\tau) = e^{c_1 N\tau}e^{d_1 L\tau}e^{c_2 N\tau}e^{d_2 L\tau}\psi(x,0) + e(\tau), \tag{4.36}$$

where $e(\tau)$ denotes an error term. If each exponential operator in equation (4.36) is expanded as a Taylor series and compared to the Taylor series expansion of the formal solution (4.15), one gets the following system of equations that ensures an $\mathrm{O}(\tau^2)$ accurate solution:

$$\begin{aligned} c_1 + c_2 &= 1 \\ d_1 + d_2 &= 1 \\ c_1 d_1 + c_1 d_2 + c_2 d_2 &= 1/2 \\ c_2 d_1 &= 1/2 \end{aligned} . \tag{4.37}$$

The system (4.37) has multiple solutions. From a numerical point of view, it is convenient to choose $d_2 = 0$, since the calculation of the linear operator $e^{\alpha L\tau}$ requires the computationally expensive calculation of an FFT and an IFFT, while the calculation of the nonlinear operator $e^{\alpha N\tau}$ is much faster. From the choice $d_2 = 0$, one can find a solution $c_1 = c_2 = 1/2$, $d_1 = 1$.

Then equation 4.36 becomes

$$\psi(x,\tau) = e^{N\tau/2}e^{L\tau}e^{N\tau/2}\psi(x,0) + \mathrm{O}\left(\tau^3\right). \tag{4.38}$$

4.4 Fourth-order split-step scheme

Yoshida [110] showed that one can construct higher order split-step schemes from the second order split-step scheme (4.38) without using the Taylor series expansion. Rather, one can apply the Campbell-Baker-Hausdorff (CBH) formula for operators. The CBH formula relates to the product of two exponential operators. The formula states that

$$e^X e^Y = e^Z,$$

where

$$\begin{aligned} Z &= X + Y + \frac{1}{2}[X,Y] + \frac{1}{6}[X,X,Y] + [Y,Y,X] + \\ &+ \frac{1}{12}([X,X,Y] + [Y,Y,X]) + \frac{1}{720}([Y,Y,Y,Y,X] + [X,X,X,X,Y]) + \\ &+ \frac{1}{360}([Y,X,X,X,Y] + [X,X,Y,Y,X]) + \\ &+ \frac{1}{120}([X,X,Y,Y,X] + [Y,Y,X,X,Y]) + \cdots \end{aligned} \tag{4.39}$$

Here $[\cdot,\cdot]$ denotes the commutator, defined by $[X,Y] = XY - YX$, and higher order bracket terms are defined by $[X,Y,Z] = [X,[Y,Z]]$ etc. The commutator has some basic properties that can be easily verified,

$$\begin{aligned} [X,X] &= 0, \\ [aX,bY] &= ab\,[X,Y] \text{ for } a,b \in \mathbb{R}, \\ [X,Y] &= -[Y,X], \\ [[A,B],C] &= [A,B,C]-[B,A,C]. \end{aligned} \tag{4.40}$$

By applying the CBH formula twice, one can show that

$$e^X e^Y e^X = e^W, \tag{4.41}$$

where the operator W can be expanded as

$$\begin{aligned} W &= 2X+Y+\frac{1}{6}[Y,Y,X]-\frac{1}{6}[X,X,Y]+\frac{7}{360}[X,X,X,X,Y]- \\ &- \frac{1}{360}[Y,Y,Y,Y,X]+\frac{1}{90}[X,Y,Y,Y,X]+ \\ &+ \frac{1}{45}[Y,X,X,X,Y]-\frac{1}{60}[X,X,Y,Y,X]+\frac{1}{30}[Y,Y,X,X,Y]+\cdots. \end{aligned} \tag{4.42}$$

The advantage of this representation is that all brackets contain an odd number of terms, due to the reversibility of the operator (4.41). Indeed, using the expansion (4.42), one can represent the second-order split step operator

$$S_2(\tau) = e^{\frac{\tau}{2}N} e^{L\tau} e^{\frac{\tau}{2}N} \tag{4.43}$$

as

$$S_2(\tau) = e^{W_2}, \tag{4.44}$$

where

$$W_2 = \alpha_1\tau + \alpha_3\tau^3 + \mathbb{O}\left(\tau^5\right),$$

and

$$\alpha_1 = L + N,\ \alpha_3 = \frac{1}{12}[L,L,N] - \frac{1}{24}[N,N,L],\ \alpha_5 = \frac{7}{5760}[N,N,N,N,L] + \cdots.$$

To construct fourth order scheme S_4^τ, we apply the CBH formulas (4.41) and (4.42) to the following operator,

$$S_4(\tau) = S_2(a_1\tau)\, S_2(a_0\tau)\, S_2(a_1\tau), \tag{4.45}$$

where

$$\begin{aligned} S_2(a_1\tau) &= \exp\left(a_1\tau\alpha_1 + a_1^3\tau^3\alpha_3 + a_1^5\tau^5\alpha_5 + \cdots\right), \\ S_2(a_0\tau) &= \exp\left(a_0\tau\alpha_1 + a_0^3\tau^3\alpha_3 + a_0^5\tau^5\alpha_5 + \cdots\right). \end{aligned}$$

From these expressions, and the CBH formulas for symmetric operators (4.41) and (4.42), it follows that

$$S_4(\tau) = e^{W_4} \tag{4.46}$$

where

$$\begin{aligned} W_4 &= 2\left\{a_1\tau\alpha_1 + a_1^3\tau^3\alpha_3 + \mathrm{O}\left(\tau^5\right)\right\} + \\ &+ \left\{a_0\tau\alpha_1 + a_0^3\tau^3\alpha_3 + \mathrm{O}\left(\tau^5\right)\right\} + \\ &+ \frac{1}{6}\left\{[a_0\tau\alpha_1, a_0\tau\alpha_1, a_1\tau\alpha_1] + \mathrm{O}\left(\tau^5\right)\right\} - \\ &- \frac{1}{6}\left\{[a_1\tau\alpha_1, a_1\tau\alpha_1, a_0\tau\alpha_1] + \mathrm{O}\left(\tau^5\right)\right\} + \mathrm{O}\left(\tau^5\right). \end{aligned} \tag{4.47}$$

The commutator in the third bracket is zero, since

$$\frac{1}{6}\left[a_0\tau\alpha_1, a_0\tau\alpha_1, a_1\tau\alpha_1\right] = \frac{a_0^2 a_1\tau^3}{6}\left[\alpha_1, \alpha_1, \alpha_1\right] = 0.$$

Similarly, the commutator in the fourth term of equation (4.47) is zero. Therefore the operator (4.47) becomes

$$W_4 = \left(2a_1 + a_0\right)\tau\alpha_1 + \left(a_0^3 + 2a_1^3\right)\tau^3\alpha_3 + \mathrm{O}\left(\tau^5\right). \tag{4.48}$$

To ensure that the operator $S_4(\tau)$ is fourth order accurate, we need to show that $W_4 = \alpha_1\tau + \mathrm{O}(\tau^5)$. From (4.48) it follows that

$$\begin{aligned} 2a_1 + a_0 &= 1 \\ a_0^3 + 2a_1^3 &= 0. \end{aligned}$$

These equations are satisfied when

$$a_0 = -\frac{2^{1/3}}{2 - 2^{1/3}}, \tag{4.49}$$

$$a_1 = \frac{1}{2 - 2^{1/3}}. \tag{4.50}$$

Therefore, the fourth-order accurate scheme is given by equation (4.45) where a_0 and a_1 are given by equations (4.49) and (4.50) respectively.

4.5 Comparison between Runge-Kutta method and the split-step method

In Section 4.1 we developed a fourth-order pseudo-spectral Runge-Kutta method for solving the PDNLS equation. In sections 4.2 to 4.4 we developed the fourth-order split-step method for solving the PDNLS. Both methods are fourth-order accurate in terms of temporal integration, while spatial errors of in both cases are exponentially small provided that the interval length L is chosen sufficiently large, and that the solution is sufficiently smooth [97]. Therefore, in terms of accuracy, the methods are equivalent. However, the split-step method is superior in terms of efficiency, i.e. computational time. For the fourth-order pseudo-spectral Runge-Kutta scheme, each time step requires one FFT computation and one IFFT computation for $k_1, \cdots, k_4$, resulting in a total of four FFT computations and four IFFT computations per time step. For the fourth-order split-step scheme, each operator $e^{\alpha L \tau}$ requires a single FFT, and a single IFFT to be calculated. From the respective schemes (4.43) and (4.45) it follows that, during t each time step, only three FFT's and three IFFT's need to be calculated. Based on the reduction of Fourier transform evaulations, the split-step method yields a 33% improvement in terms of computational time.

In Figure 4.1 we show the percentage improvement of the split-step method in compar-

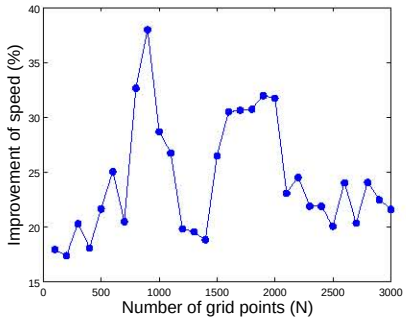

Figure 4.1: *Percentage of increase of computational speed for the split-step method relative to the Runge-Kutta method*

ison to the Runge-Kutta method for different numbers of grid points N. We see that the improvement is slightly below 33%. This may reflect the fact that the split-step method has larger storage requirements.

Since the majority of the compuation time depends on the calculation of the FFT, it is important to maximize the efficiency of the FFT algorithm. The efficiency of the FFT algorithm depends largely on the size of the vector N, representing the number of spatial grid points chosen during the discretization of the original PDE. The efficiency of the FFT algorithm depends on the ability to factorize the number N. In particular, the FFT algorithm works best when the number of grid points is of the form $N = 2^j$, while it performs worst when N is a prime number. For example, the split-step method for $N = 2039$ grid points takes almost ten times longer than the split-step method for $N = 2^{11} = 2048$ grid points. For this reason we used $N = 2048$ grid points for the split-step method throughout the thesis.

For the unperturbed NLS equation, a stability analysis for the Runge-Kutta method and split-step method was carried out by Yang [109]. He showed that the Runge-Kutta method is stable if and only if the spatial stepsize Δx and the temporal stepsize Δt satisfy the inequality

$$\frac{\Delta t}{\Delta x^2} \leq \frac{2\sqrt{2}}{\pi^2}. \tag{4.51}$$

He also showed that the split-step scheme is stable whenever the criterion of Weideman and

Herbst [107] is satisfied:

$$\frac{\Delta t}{\Delta x^2} < \frac{1}{\pi}. \tag{4.52}$$

However, it was shown that the split-step scheme is also stable for intervals of the ratio $\Delta t/\Delta x^2$ outside the stability criterion (4.52).

We compared the stability of the numerical schemes of the PDNLS equation to that of the unperturbed NLS equation. Our results show that the stability criterion (4.51) also applies for the Runge-Kutta scheme for the PDNLS equation. For the split-step scheme of the PDNLS equation we chose $\Delta t = 0.005$ and $\Delta x = \frac{200}{2048} \approx 0.05$. The results were stable in all our simulations performed in Chapter 5 and Chapter 6, despite the fact that the ratio $\Delta t/\Delta x^2$ lies outside the stability region (4.52). A rigorous stability analysis is required to determine wheter the stability criterion 4.52 is improved as a result of the dissipation in the PDNLS equation. This analysis is beyond the scope of the present thesis.

Chapter 5

Oscillating soliton attractors of the PDNLS equation

The parametrically driven nonlinear Schrödinger (PDNLS) equation is an important mathematical model that describes a large variety of physical phenomena. The model is used to describe Faraday resonance in vertically oscillating water tanks [74, 75, 104], magnetization waves in an easy-plane ferromagnet [15, 32, 112], the effect of phase-sensitive amplifiers on solitons propagating in optical fibres [41, 89], and many more (see [20] and the references therein).

The PDNLS equation admits soliton solutions. Many of these solutions cannot be expressed analytically, and can only be obtained by numerical methods. In this chapter we review some of the results that are reported in the literature. This chapter lays the foundation for the direct scattering study of the PDNLS equation that follows in Chapter 6.

This chapter is structured as follows: In Section 5.1 we look at the solutions of the PDNLS equation. We use this to define the oscillating soliton attractors that form the basis of our study. In Section 5.2 we look at the temporal structure of the oscillating soliton attractors. This includes a discussion of the period-doubling route to temporal chaos. In Section 5.3 we look at the spatial structure of the oscillating soliton attractors. The influence of the damping

coefficient on the formation and propagation of radiation waves of the oscillating soliton attractors is considered in Section 5.4. The results are briefly summarized in Section 5.5.

5.1 Solutions of the PDNLS equation

The PDNLS equation is given by

$$i\phi_t + \phi_{xx} + 2|\phi|^2\phi = h\phi^* e^{2it} - i\gamma\phi. \tag{5.1}$$

The left hand side of equation (5.1) is the focusing nonlinear Schrödinger (NLS) equation. The right hand side of (5.1) relates to damping and driving of the PDNLS equation. In particular the parameters $\gamma > 0$ and $h > 0$ correspond to the strength of the damping and parametric driving respectively. In the absence of damping and driving, i.e. $\gamma = h = 0$, the PDNLS equation becomes the integrable NLS equation. One can therefore think of the damping and driving as a perturbation of the integrable NLS equation. It is convenient to make the substitution $\phi(x,t) = \psi(x,t)\, e^{it}$. Then the PDNLS equation becomes autonomous:

$$i\psi_t + \psi_{xx} + 2|\psi|^2\psi - \psi = h\psi^* - i\gamma\psi. \tag{5.2}$$

This simplifies the application of the split-step method, the numerical scheme we use to integrate the PDNLS equation. Another advantage of this form is that it admits time-independent soliton solutions. Therefore, throughout the chapter, we work with this form of the PDNLS equation.

The simplest solution of the PDNLS equation (1.1) is the zero solution $\psi \equiv 0$. The zero solution is stable provided that the driving strength is not too large. If the driving strength exceeds the critical driving strength $h > h_c(\gamma)$, the zero solution is unstable. Here

$$h_c = \sqrt{1+\gamma^2}. \tag{5.3}$$

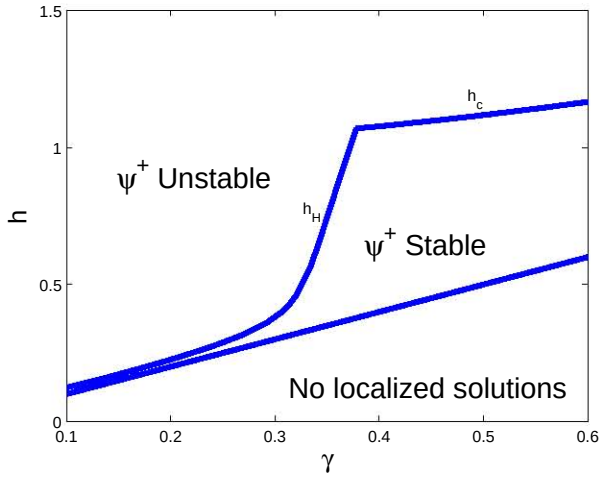

Figure 5.1: *Stability chart of the ψ^+ solution*

Moreover, for large driving strengths $h > h_c$ all spatially localized solutions are unstable with respect to continuous spectrum instabilities [15].

The PDNLS equation has two time-independent, spatially localized soliton solutions, provided that the driving strength issufficiently strong ($\gamma \leq h$). These solitons are given by

$$\psi^{\pm}(x) = A^{\pm} e^{-i\theta^{\pm}} \mathrm{sech}\left(A^{\pm} x\right), \tag{5.4}$$

where $A^{\pm} = \left(1 \pm \sqrt{h^2 - \gamma^2}\right)^{1/2}$, $\theta^{+} = \frac{1}{2}\arcsin(\gamma/h)$ and $\theta^{-} = \theta^{+} - \frac{\pi}{2}$. The solution ψ^{-} is unstable for all combinations of damping and driving strengths, γ and h respectively. The solution ψ^{+} has a stable region, shown in Figure 5.1. The stability of the ψ^{+} solution was studied by Barashenkov and coworkers [15]. They showed that the solution ψ^{+} loses its stability whenever the driving strength h becomes too large. For smaller damping coefficients ($\gamma < 0.378$) the instability is the result of a Hopf bifurcation. For larger damping coefficients($\gamma \geq 0.378$) the instability is suffered as result of continuous spectrum instabilities.

The attractors of the unstable ψ^{+} solution form the basis of our study of the PDNLS

equation. These attractors are defined in terms of heteroclinic orbits $\psi_{het}(x,t)$ satisfying

$$\lim_{t\to-\infty}\psi_{het}(x,t)=\psi^{+}(x). \tag{5.5}$$

The attractor $\psi_a(x,t)$ is defined in terms of the asymptotic behaviour of the of the heteroclinic orbit, given by

$$\psi_a(x,t):=\lim_{t\to\infty}\psi_{het}(x,t). \tag{5.6}$$

To calculate the heteroclinic orbits numerically, we use $\psi^{+}(x)$ as an initial condition, and integrate the solution numerically over a long period of time by using the fourth-order split-step method. The numerical round-off error of the initial condition $\psi^{+}(x)$ is sufficient to destabilize the solution. This initial condition provides the smallest possible numerical perturbation. We can therefore treat the resulting solution as a simulation of a heteroclinic orbit. It should be noted that heteroclinic orbits are not necessarily unique. There could be multiple heteroclinic orbits. The study of the uniqueness of the numerically obtained heteroclinic orbits is beyond the scope of this thesis.

In 1995, Bondila and coworkers [25] undertook a numerical study of the attractors that arise in the unstable region of the ψ^{+} solution. Their study relied on the direct simulation of heteroclinic orbits described above. They reported that, in the region where the zero solution is unstable ($h>h_c$), spatio-temporally chaotic attractors arise due to instabilities in the continuous spectrum. In the region $h<h_c$, three types of attractors were identified, namely the zero attractor, spatio-temporally chaotic attractors, and most notably oscillating soliton attractors. Oscillating soliton attractors are spatially localized, while being temporally periodic or quasiperiodic. These results are summarized in Figure 5.2. The aim of this chapter is to describe the oscillating soliton attractors.

In this thesis we restrict ourselves to the study of the oscillating soliton attractors. However, it should be noted that more localized solutions of the PDNLS equation are also reported in the literature. Unstable travelling solitons were reported by Barashenkov and Zemlyanaya

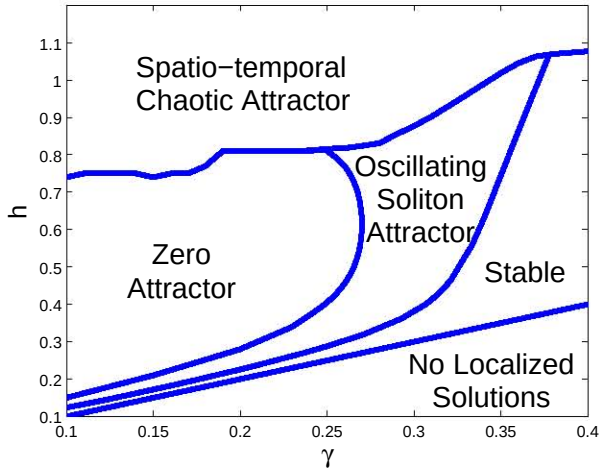

Figure 5.2: *Attractor chart of the ψ^+ solution*

[17, 19]. Soliton complexes were obtained by using Newton's fixed point iteration method. These solutions were numerically continued to obtain both stable and unstable solutions. Stable soliton complexes were first reported in 1999 by Barashenkov and Zemlyanaya [16]. The same authors recently constructed a stability chart for two-soliton complexes [18]. Quasi-periodic two-soliton complexes were also obtained by Alexeeva and Zemlyanaya [13] through direct simulation.

5.2 Temporal behaviour of oscillating soliton attractors

Bondila and coworkers [25] reported that the oscillating soliton attractor region consists of temporally periodic and quasi-periodic solitons. The temporally periodic oscillating soliton attractors can be classified as N-periodic solutions. Here, an N-periodic solution $\psi_N(x,t)$ with minimal period T is defined as a wave whose amplitude contains exactly N local maxima and N local minima on the interval $0 \leq t < T$. Examples of a 1-period, a 2-period and a quasiperiodic oscillating soliton attractor are shown in Figure 5.3 (a), (b) and (c) respectively. In each case the modulus of the solution is shown on the left, while the phase portrait of the attractor at $x = 0$, $\psi(0,t)$, is shown on the right. The latter representation is useful for the

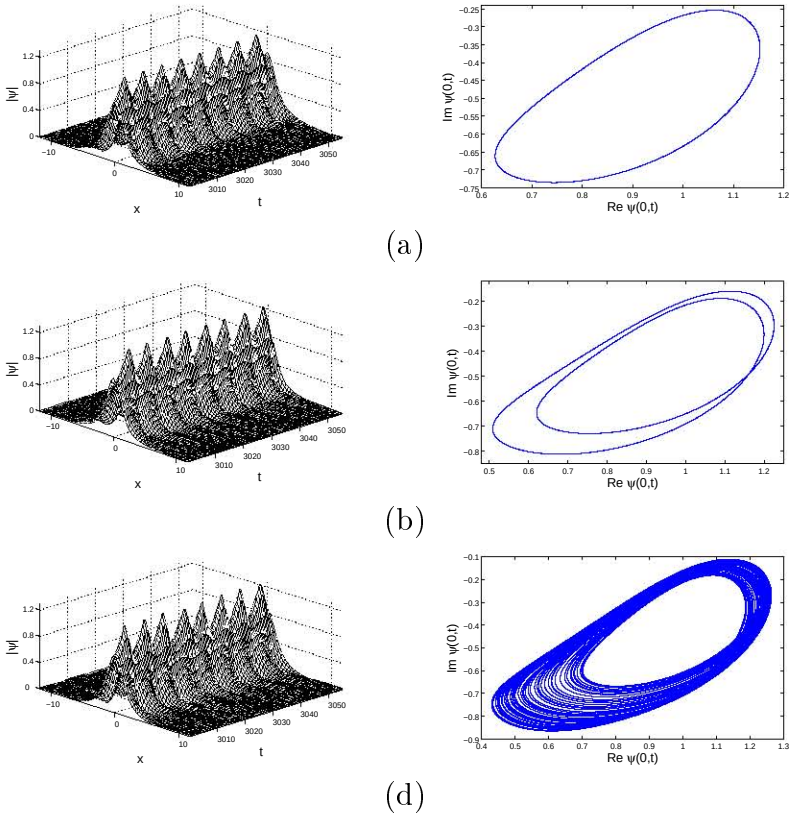

Figure 5.3: *Solutions (left) and amplitudes (right) of oscillating soliton attractors. (a) 1-Periodic (b) 2-Periodic (c) Quasi-periodic*

identification of the temporal period, and is sometimes referred to as a the Lissajous figure. These attractors were calculated for a fixed damping $\gamma = 0.15$, where driving strengths of $h = 0.19$, $h = 0.202$ and $h = 0.2087$ were used to generate (a), (b) and (c) respectively.

For most combinations of damping and driving, the associated oscillating soliton attractors consist of 1-period solitons. The only exception is in a narrow band that is bounded by the zero attractor region. This part of the oscillating soliton attractor region is shaded in the attractor chart shown in Figure 5.4. In this band the oscillating soliton attractors exhibit a complicated structure that is characterized by a period-doubling route to chaos.

A period-doubling route to chaos arises in the small damping regime ($\gamma < 0.27$) whenever the damping is fixed, and the driving is increased above the Hopf bifurcation value h_H. A further increase in driving leads to the emergence of the zero attractor. Here h_H is the critical

driving strength where the Hopf bifurcation occurs. An example is shown in Figure 5.5 for the case where we fix the damping coefficient $\gamma = 0.15$. Here we show the local maxima and minima of the amplitudes of oscillating soliton attractors for different driving strengths. For driving strengths $0.15 < h < 0.17$ the ψ^+ solution is stable. For the critical driving strength $h_H = 0.17$ the ψ^+ solution loses its stability by means of a Hopf bifurcation. The result is the emergence of a 1-period oscillating soliton attractor. The 1-period oscillating soliton attractor arises for $0.17 < h < 0.198$. At $h = 0.198$ a period-doubling bifurcation occurs, resulting in a 2-period oscillating soliton attractor for $0.198 < h < 0.204$. At $h = 0.204$ a second period-doubling bifurcation occurs, resulting in the formation of a 4-period oscillating soliton attractor. For driving strengths $0.204 \leq h \leq 0.2063$ a series of period-doubling bifurcations occur. A further increase in driving strength ($0.2063 < h < 0.2102$) leads to the formation of temporally chaotic attractors. For large driving strengths the oscillating soliton attractor makes way for the zero attractor ($0.2102 < h < 0.74$) or a spatio-temporally chaotic attractor ($h > 0.74$).

We have shown that, for the majority of combinations of damping and driving (γ, h) within the oscillating soliton attractor region, the associated attractors have a 1-period temporal structure. For these attractors the temporal period T is a decreasing function of both the damping coefficient γ and the driving strength h. To illustrate this, Figure 5.6 (a) shows the temporal period T as a function of the damping coefficient γ when the driving strength is fixed at $h = 0.55$. As the damping increases, the temporal period decreases. In Figure 5.6 (b) the temporal period T is shown as a function of the driving strength h for a fixed damping coefficient of $\gamma = 0.3$. Once again we see that the temporal period T decreases when the driving strength h is increased.

To summarize we have shown that. multiple-period and quasiperiodic oscillating soliton attractors are associated with combinations of damping and driving strengths (γ, h) situated in a narrow band on the boundary between the oscillating soliton attractor region and the zero attractor region. These complicated temporal structures are the result of series of

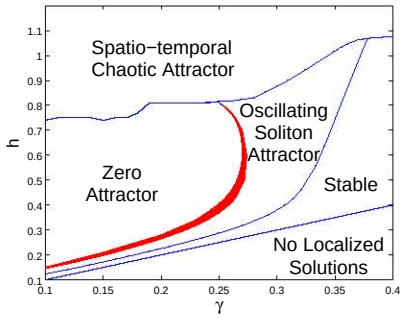

Figure 5.4: *Attractor chart. The shaded area indicates oscillating soliton attractors that are not 1-periodic attractors. These attractors consists of N-periodic and quasiperiodic oscillating soliton attractors, where $N \geq 2$.*

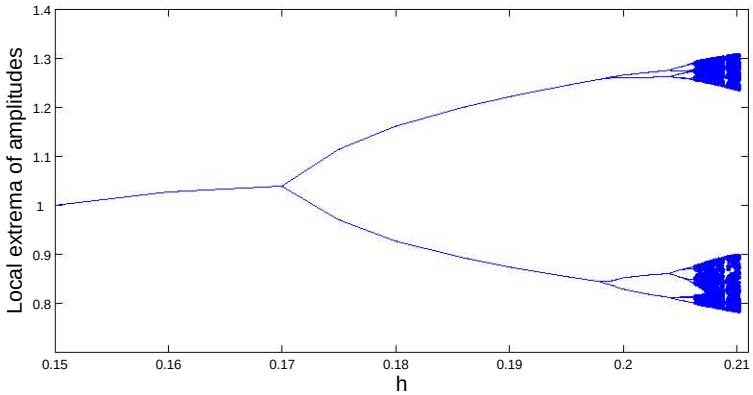

(a)

Figure 5.5: *Period doubling route to chaos for* $\gamma = 0.15$.

period-doubling bifurcations that leads to temporal chaos. The majority of attractors that form within the oscillating soliton attractor region have a 1-period temporal structure. The periods of these attractors are decreasing functions of both damping and driving strengths.

5.3 Spatial structure of oscillating soliton attractors

Oscillating soliton attractors consist of two ingredients, namely a single soliton and radiation. The soliton is spatially centred at the origin, and oscillates with time. The characteristics of the soliton include the period of temporal oscillation, the maximum and minimum values of

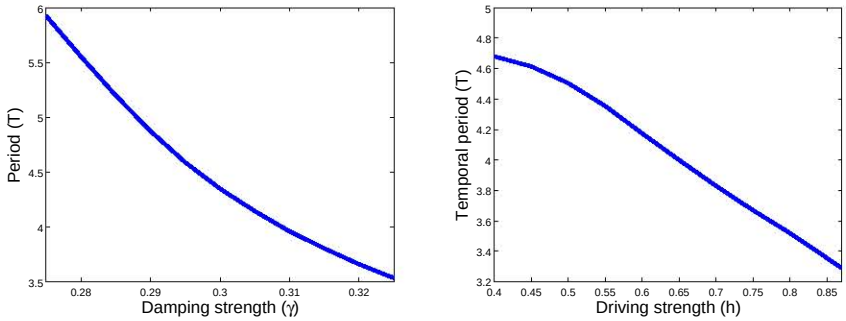

Figure 5.6: *Temporal period of oscillating soliton attractors. In (a), the driving strength is fixed at* $h = 0.55$*. In (b), the damping coefficient is fixed at* $\gamma = 0.3$*.*

the amplitude, and the magnitude of the oscillations. The latter is defined as

$$m(\gamma, h) = \max_t \{|\psi_a(0,t)|\} - \min_t \{|\psi_a(0,t)|\}, \tag{5.7}$$

where $\psi_a(x,t)$ is the oscillating soliton attractor that arises for the combination of damping and driving strength (γ, h). In general an increase in the amplitude of a soliton leads to a decrease in its width and vice versa. Radiation consists of moving waves with small amplitudes. These waves arise in pairs, symmetric about the origin. The radiation waves dissipate, and consequently have a finite lifespan, i.e. their amplitudes decay to zero as they move away from the origin. Other important characteristics are the velocities of the radiation waves and their amplitudes at the moment of formation. The latter gives an indication of the energy that is radiated from the soliton.

This leads us to the question: How do the characteristics of the soliton and the radiation depend on the damping and driving? For a fixed driving strength, an increase in damping leads to a smaller magnitude of oscillation of the amplitude. Indeed, the maximum soliton amplitude decreases while the minimum soliton amplitude increases. This leads to a decrease in the energy of the radiation. This decrease, along with the fact that dissipation increases, causes the lifetime of the radiation waves to decrease. An increase in the driving strength has the opposite effect on these characteristics. These results are summarized in Table 5.1.

Component	Characteristic	Increase: Damping	Increase: Driving
Soliton	Temporal Period	Decrease	Decrease
	Maximum Amplitude	Decrease	Increase
	Minimum Amplitude	Increase	Decrease
Radiation	Energy	Decrease	Increase
	Velocity	Unchanged	Unchanged
	Lifetime	Decrease	Increase

Table 5.1: *Influence of increased damping and driving on the characteristics of the oscillating soliton attractor.*

Also included in the table is the interesting characteristic of the velocity of radiation waves, namely that the velocity of the radiation waves is independent of the damping and driving strengths. We also included the dependence of the temporal period of oscillating soliton attractors on the damping and driving strengths, as discussed in the previous section.

In order illustrate these important characteristics, we consider the oscillating soliton attractors that arise when the damping is fixed at $\gamma = 0.3$, and when the driving strength is varied.

$\gamma = 0.3$ case

We start this case study by considering the characteristics of the soliton itself. Table 5.1 shows that an increase in driving strength leads to an increase in the maximum amplitude and a decrease in the minimum amplitude of the soliton. It is therefore clear from the definition in equation (5.7) that an increase in driving strength leads to an increase in the magnitude of oscillation $m(0.3, h)$. This characteristic is illustrated in Figure 5.7 where we show the magnitude of oscillations as a function of the driving strength h.

The properties of the radiation are best illustrated by considering the imaginary part of the oscillating soliton attractors. We use the notation

$$\psi_m(x,t) = \mathrm{Im}\{\psi_a(x,t)\}.$$

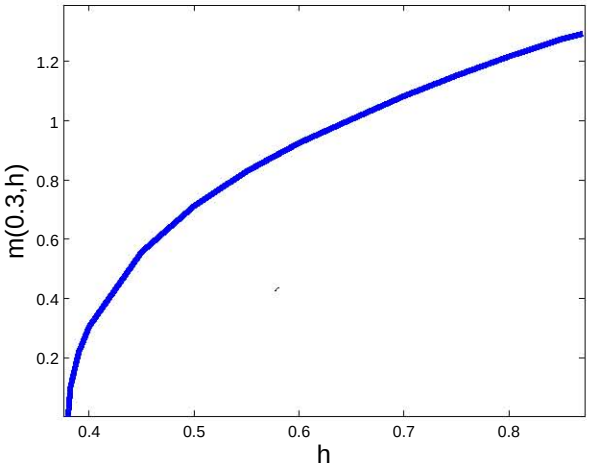

Figure 5.7: *The magnitude of oscillations* (5.7) *as a function of the driving strength* h *for fixed* $\gamma = 0.3$.

For 1-period oscillating soliton attractors, two sets of radiation wave trains are formed during each temporal cycle. Each wave train consists of a hill and a valley. These wave trains are spatially symmetric about the centre. Each wave train travels away from the origin. An example of the radiation wave trains is shown in Figure 5.8.

An important relationship between the driving strength h and radiation waves exists, namely that larger driving strength leads to the emission of larger radiation waves. In particular, the amplitude of the radiation waves is an increasing function of the driving strength h. To illustrate this, we show the maximum amplitude of the valleys at the formation

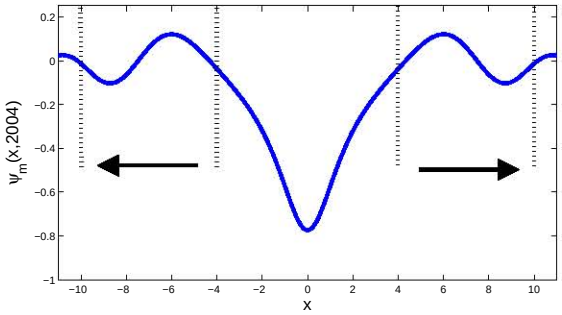

Figure 5.8: *An example of the two pairs of radiation wave trains that form during each cycle. This is the imaginary part of the soliton* $\psi_m(x,t)$ *for* $\gamma = 0.3$ *and* $h = 0.6$.

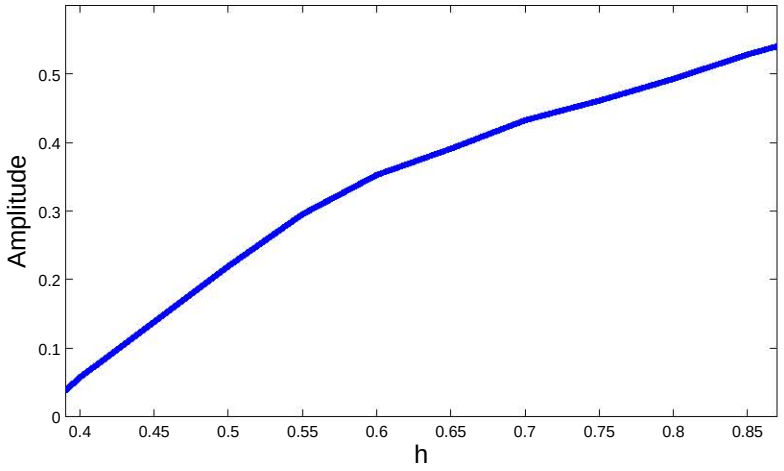

Figure 5.9: *Amplitude of valleys of radiation wave trains for* $\gamma = 0.3$ *and different driving strengths.*

of the wave trains as a function of the driving strength h. The results are shown in Figure 5.9. Here we can clearly see that the amplitudes increase with the driving strength.

The effect of increased amplitudes of the radiation waves, caused by increased driving strengths, is that the lifespan of the radiation waves increases. This, in turn, leads to increased radiation energy. To illustrate this, we introduce the mass of radiation of $\psi_m(x,t)$, defined as

$$R_m(\gamma, h) = \int_{x_0}^{\infty} |\psi_m(x, t_0)|^2 \, dx, \tag{5.8}$$

where

$$x_0 := \text{Smallest positive root of } \psi_m(x, t_0)$$

and t_0 is the point in time where the amplitude of $\psi_m(0,t)$ is a global minimum. This means that t_0 satisfies the criteria

$$\frac{\partial \psi_m}{\partial t}(0, t_0) = 0, \quad \frac{\partial^2 \psi_m}{\partial t^2}(0, t_0) > 0.$$

In essence equation (5.8) measures the energy of the radiation tail. In Figure 5.10 (a) we

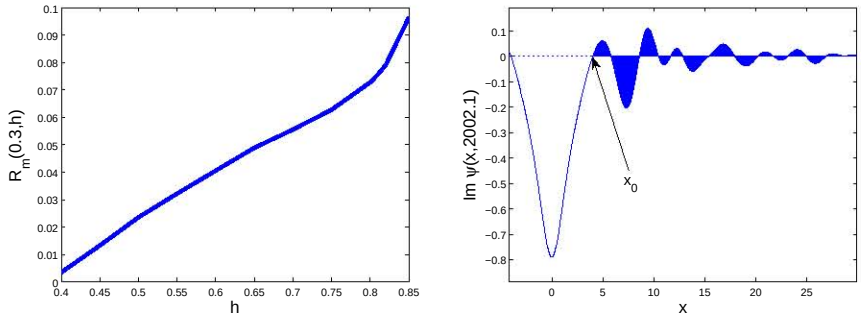

Figure 5.10: *The mass of radiation is shown as a function of driving strength h for $\gamma = 0.3$ in (a). In (b) a graphical representation the mass of radiation $R_m(0.3, 0.82)$ is shown.*

show the mass of radiation for different driving strengths h for fixed damping $\gamma = 0.3$. It is clear that the mass of radiation is an increasing function of the driving strength h. In Figure 5.10 (b) we show a graphical representation of the mass of radiation. In this example we show the imaginary part of the oscillating soliton attractor that arises when the damping coefficient is $\gamma = 0.3$ and the driving strength is $h = 0.82$.

The next aspect of radiation we consider is the formation of radiation waves. To do this, we consider the spatial profile of the radiation waves. Here the spatial profile is defined as the projection of the local extremes of $\psi_m(x,t)$ onto the space-time (x,t) plane. The local extrema are defined as the set

$$\left\{ \psi_m(x,t) \left| \frac{\partial \psi_m}{\partial x} = 0 \right. \right\}. \tag{5.9}$$

For small driving strengths $h_H < h < 0.46$ two radiation waves form symmetrically about the origin at $x = \pm x_f$ for $x_f > 0$, both moving away from the origin. An example is shown in Figure 5.11 (a) where the spatial profile is shown for $h = 0.39$. The hills satisfying $\partial^2 \psi_m / \partial x^2 > 0$ are indicated with a solid line, while the valleys satisfying $\partial^2 \psi_m / \partial x^2 < 0$ are indicated with a dotted line. For driving strengths $0.459 < h \leq 0.53$ the hills no longer move away from the origin, but move towards the origin. At the origin the two hills collide. After collision, both hills continue their propagation, unchanged by the collision.

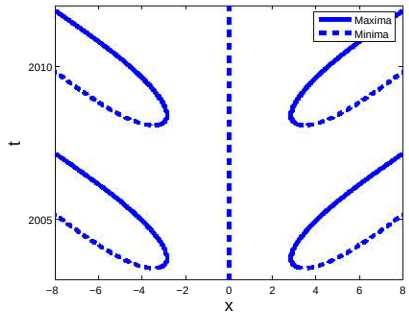

(a)

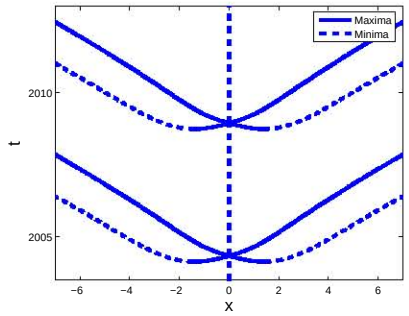

(b)

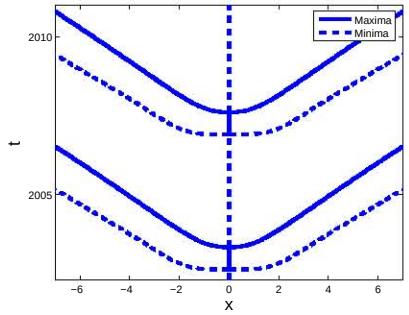

(c)

Figure 5.11: *The three different ways that radiation is emitted.* $h = 0.39$ *in (a),* $h = 0.46$ *in (b), and* $h = 0.53$ *in (c).*

An example is shown in Figure 5.11 (b), corresponding to the oscillating soliton attractor arising for $h = 0.46$. As the driving strength $h \to 0.528$, the points of formation $x_f \to 0$. For $h \geq 0.528$ both sets of radiation waves form at the origin, i.e. $x_f = 0$. An example is shown in Figure 5.11 (c), corresponding to the solution for $h = 0.53$. This is a typical pattern of radiation wave formation in the large damping regime $\gamma > 0.275$. For smaller damping coefficients this pattern is destroyed by the formation of the zero attractor in the

zero attractor region.

5.4 The effect of damping on radiation

Barashenkov and coworkers [20] investigated the influence of damping coefficient on the radiation emitted by oscillating soliton attractors. Their study relied on the calculation of the flux of the oscillating soliton attractors through points $x = \pm R$, where R is chosen large enough so that the flux through these points is not affected by the oscillation of the soliton, thus ensuring that the flux is only due to radiation. They showed that, in the large damping regime ($\gamma > 0.28$) the flux is larger than in the small damping regime ($\gamma < 0.25$). They argued that the ability of oscillating soliton attractors to emit more radiation in the large damping regime acts as a stabilizing agent for the 1-period oscillating soliton attractors, thus eliminating the period-doubling bifurcations that leads to the zero attractor in the small damping regime. This result is counter-intuitive in the sense that larger damping coefficients correspond to stronger dissipation. One may therefore expect lower flux in this regime. The effect of damping on the emission of radiation is best illustrated by considering the spatial profile of the oscillating soliton attractors.

Before we discuss the relationship between the damping coefficient and the radiation, let's first consider the formation of radiation waves. During each temporal oscillation, a wave train is emitted in both directions, each consisting of a hill and a valley. We refer to this as *the original wave train*. The original wave train, together with the previous wave trains, form a radiative tail. During the time evolution of the oscillating soliton attractor, some waves in the radiative tail interact with each other. The result is the formation of two additional radiation waves in the form of a hill and a valley. We refer to these waves as *the interaction waves*. The formation of interaction waves plays a crucial role in the propagation of the radiation waves.

We use Figure 5.12 to illustrate the formation of interaction waves in the case of the

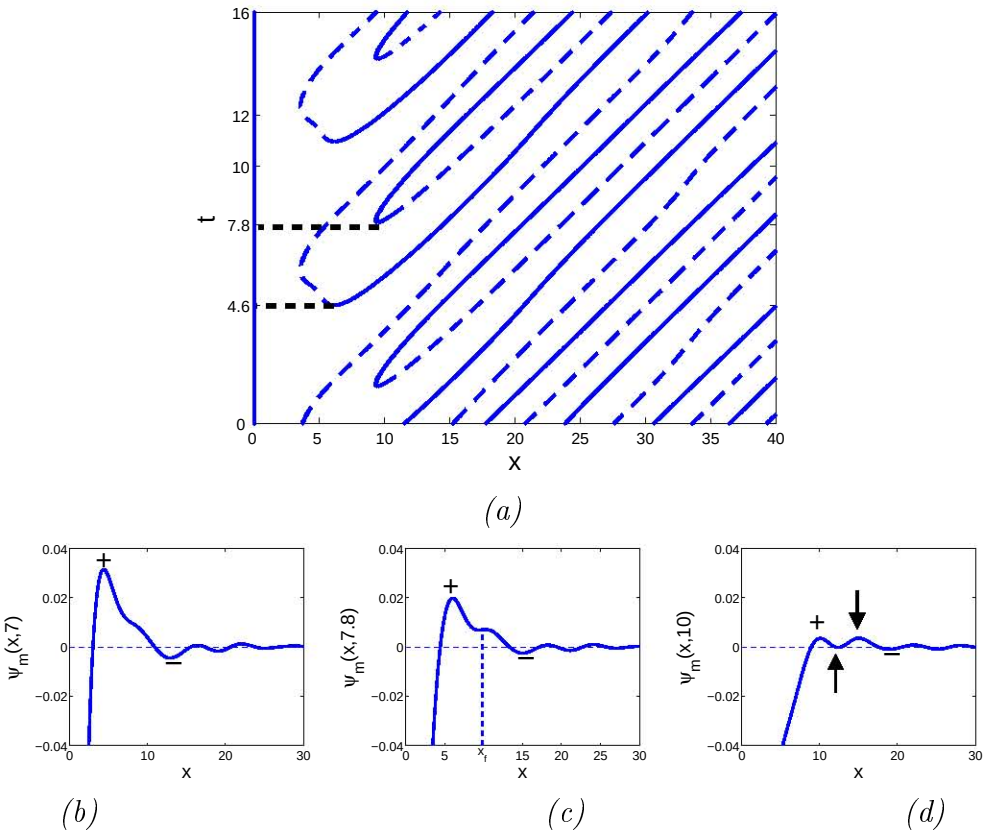

Figure 5.12: *In (a) the spatial profile of the attractor* ($\gamma = 0.2\,, h = 0.2364$). *The solutions* $\psi_m\,(x,t)$ *are shown for* $t = 7$, $t = 7.8$ *and* $t = 10$ *in (b), (c) and (d) respectively, where* + *indicates the hill and* – *the valley of the original wave train. The arrows in (d) shows the interaction waves.*

oscillating soliton attractor associated with damping coefficient $\gamma = 0.2$ and driving strength $h = 0.2634$. In Figure 5.12 (a) we show the spatial profile of the attractor. Since the solution $\psi\,(x,t)$ is spatially symmetric about the origin, we only consider the half-plane $x \geq 0$. The solid lines represent valleys ($\partial^2\psi_m/\partial x^2 > 0$) while the dashed lines represent hills ($\partial^2\psi_m/\partial x^2 < 0$). At $t = 4.6$ we see the formation of an original wave train, consisting of a hill (dashed line) and a valley (solid line). At $t = 7.8$ the interaction waves are formed $x_f = 9.5$ units away from the origin. In Figure 5.12 (b) – (d) we show the solution $\psi_m\,(x,t)$. In (b) the solution is shown at $t = 7$ where the interaction waves haven't formed. We use + to indicate the hill and – to indicate the valley of the original wave train. In (c) the solution is shown at $t = 7.8$. The interaction waves form at the saddle point $x_f = 9.8$. As time evolves beyond

$t = 7.8$, the saddle point splits to form a local maximum and a local minimum, resulting in the formation of the interaction waves. In (d) we show the solution at $t = 10$. The arrows are used to indicate the interaction waves. The interaction waves separate the hill (+) and the valley (–) of the original wave train.

We studied the radiation waves of the oscillating soliton attractors for different choices of damping coefficient γ. For a fixed driving strength h an increase in damping coefficient γ results in a loss of energy emitted through radiation (see Table 5.1). To compensate for this, we vary the driving strength with the damping coefficient γ by fixing the magnitude of oscillations $m(\gamma, h) = 0.25$. In other words, for each damping coefficient γ we associate the driving strength $h_r(\gamma)$ defined as

$$h_r(\gamma) := \{h \,|m(\gamma, h) = 0.25\}. \tag{5.10}$$

The fact that, for any fixed damping γ, the magnitude of oscillations increases monotonically with h ensures that the number $h_r(\gamma)$ is unique.

We calculated the spatial position of the formation of interaction waves x_f for different combinations of damping γ and driving strengths $h_r(\gamma)$. In Figure 5.13 (a) we show x_f as a function of the damping coefficient γ. When the damping γ is increased, the point of formation x_f moves away from the origin on the intervals $0.1 \leq \gamma \leq 0.27$ and $0.29 < \gamma \leq 0.31$. This shows that x_f is larger in the case of larger damping. The function x_f mostly decreases on the interval $\gamma > 0.27$, while some jump discontinuities occur. This can be explained as follows: At the formation of interaction waves, the waves form between two pre-existing radiation waves. We refer to the neighbouring radiation wave closest to the origin as the *left wave*, and the one furthest from the origin as the *right wave*. As the damping increases, the point of formation approaches the right wave. As x_f approaches the right wave, the interaction waves and the right wave repel each other. The consequence is that the interaction waves form closer to the origin. This accounts for the decreasing of the point of formation

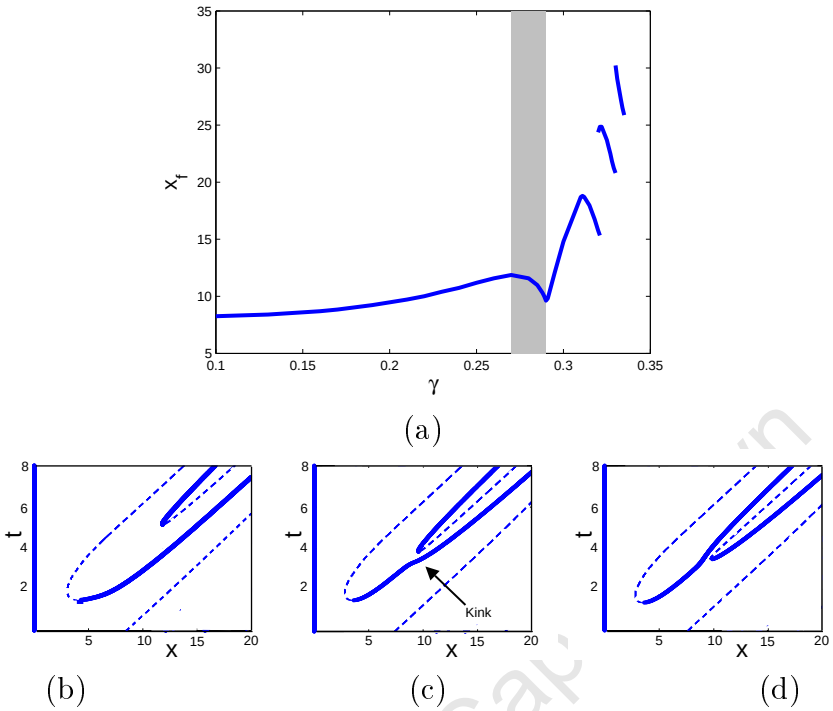

Figure 5.13: *Formation points of interaction radiation waves. In (a) the spatial point of formation x_f is shown for attractors for different damping coefficients γ, each with a magnitude of oscillation $m(\gamma, h) = 0.25$. In (b), (c) and (d) the local extremes are shown for $\gamma = 0.27$, $\gamma = 0.29$ and $\gamma = 0.291$ respectively.*

x_f. At the same time the right wave moves further away from the origin. The repulsion of the right wave leads to the formation of a kink in the spatial profile. When the damping is increased beyond a critical damping coefficient the formation of interaction waves x_f occurs on the opposite side of the right wave. In other words, the right wave becomes the left wave. In Figure 5.13 (a) the critical points consist of the cusp at $\gamma = 0.29$ and the discontinuities at $\gamma = 0.32$ and $\gamma = 0.33$. Therefore despite the decreasing intervals of Figure 5.13 (a) we conclude that larger damping coefficients lead to the interaction waves forming further away from the origin.

The crossing of the interaction waves from one side of a radiation wave to the other is best explained by means of an example. In Figure 5.13 (a) the shaded area $0.27 \leq \gamma \leq 0.291$ shows a typical example of this crossing. In Figure 5.13 (b) – (d) we show the spatial profile of the interaction radiation wave and its neighbouring radiation waves. In (b) the spatial profile is

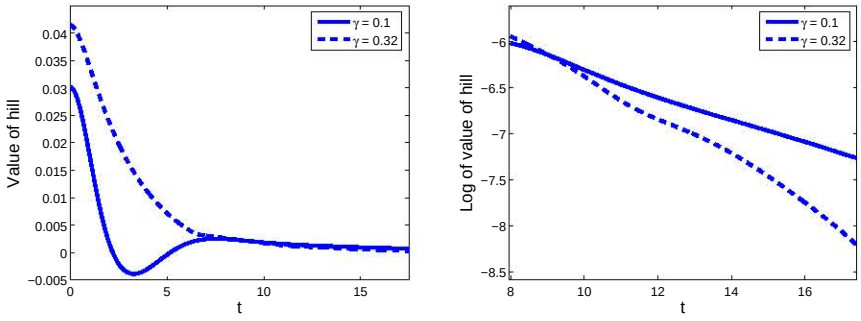

(a) (b)

Figure 5.14: *The time evolution of the value of the hill of the original radiation wave for* $\gamma = 0.1$ *(solid line) and* $\gamma = 0.32$ *(dashed line). In (a) the values are shown for* $0 \leq t \leq 18$. *In (b) the log of the values are shown for* $8 \leq t \leq 18$.

shown for the $\gamma = 0.27$ attractor. Here we see that the interaction waves form approximately in the middle of the left wave and the right wave. In Figure 5.13 (c) the spatial profile is shown for $\gamma = 0.29$ attractor. Here we see that the formation of the interaction waves occur much closer to the right wave. Notice the kink in the right wave that is caused by the repulsion between the right wave and the interaction waves. In Figure 5.13 (d) we show the spatial profile of the $\gamma = 0.291$ attractor. Here we see that the interaction waves form on the opposite side of the right wave of (b) and (c), in the process becoming the left wave of the interaction waves.

The formation of interaction waves results in an increase in the rate of decay of the amplitudes of the hill and the valley of the original wave train. Larger values of x_f imply that the original wave train propagates undisturbed for larger periods of time. This causes the amplitudes of the hill and the valley of the original wave train to decay slower. Therefore the interaction waves play an important role in the result of Barashenkov and coworkers [20]. To illustrate this, we consider the value of the hill of the original wave train. In Figure 5.14 (a) we plot the time evolution of the value of the hill. The solid line shows the value of the hill for the $\gamma = 0.1$ attractor, while the dotted line shows the value of the hill for the $\gamma = 0.32$ attractor.

For $0 \leq t \leq 6$ we see a great difference in the behaviour of the respective hills. The solid

line ($\gamma = 0.1$) decreases rapidly on the interval $0 \leq t \leq 3$, before it increases on the interval $3 \leq t \leq 6$. Thereafter the value decreases exponentially. On the other hand, the dotted line ($\gamma = 0.32$) decreases monotonically. On the interval $0 \leq t \leq 6$ the rate of change of the value of the hill corresponding to the $\gamma = 0.32$ attractor is much slower than that of the $\gamma = 0.1$ attractor. The rapid rate of change of the $\gamma = 0.1$ attractor is attributed to the formation of interaction waves that occurs at $t = 0.88$. For the $\gamma = 0.32$ attractor the interaction waves form only at $t = 9.7$, and have very little effect on the value of the hill. The effect of dissipation becomes clearly visible after sufficiently long time. In Figure 5.14 (b) we show the values of the hills for $t > 8$ by using a logarithmic scale. Here we see that the value of the $\gamma = 0.32$ attractor decays faster than that of the $\gamma = 0.1$ attractor. This is due to the fact that, in the former case, the damping is greater, resulting in a larger rate of dissipation.

5.5 Conclusion

In this chapter we defined the oscillating soliton attractors that can be obtained numerically by means of direct simulation. We showed that many of the characteristics of radiation can be obtained through inspection of the solutions themselves. In particular, we managed to gain much insight into the properties of the radiation waves. This is due to the fact that radiation waves move away from the soliton. They can therefore be easily detected. However, little insight was gained into the behaviour of the soliton itself. To obtain more insight into the soliton part of the oscillating soliton attractors we apply the direct scattering study. The next chapter is devoted to this topic.

Chapter 6

The direct scattering study of the PDNLS equation

The oscillating soliton attractors of the PDNLS equation emit radiation waves on a periodic basis. These radiation waves propagate away from the soliton itself. Radiation waves can be easily identified provided that they are well separated spatially from the soliton. However, during their formation, it is difficult to distinguish between the soliton and radiation. This combination of solitons and radiation is usually referred to as a "dressed" soliton. The purpose of the direct scattering study is to "undress" the attractor, i.e. to determine the soliton part and the radiation part of the attractor.

This chapter contains the main results of the thesis, and combines all the theory and numerical schemes of previous chapters to analyze the attractors of the PDNLS equation. The chapter is structured as follows: In Section 6.1 we give a description of the direct scattering study that is applied throughout this chapter. In Section 6.2 we apply the direct scattering study to the oscillating soliton attractors. We identify four types of attractors, each characterized by its soliton content. In Sections 6.3 and 6.4 we apply our knowledge of the soliton structure of oscillating soliton attractors to the zero attractor region. In Section 6.3 we discuss the effect of the period-doubling route to chaos on the soliton structure of the

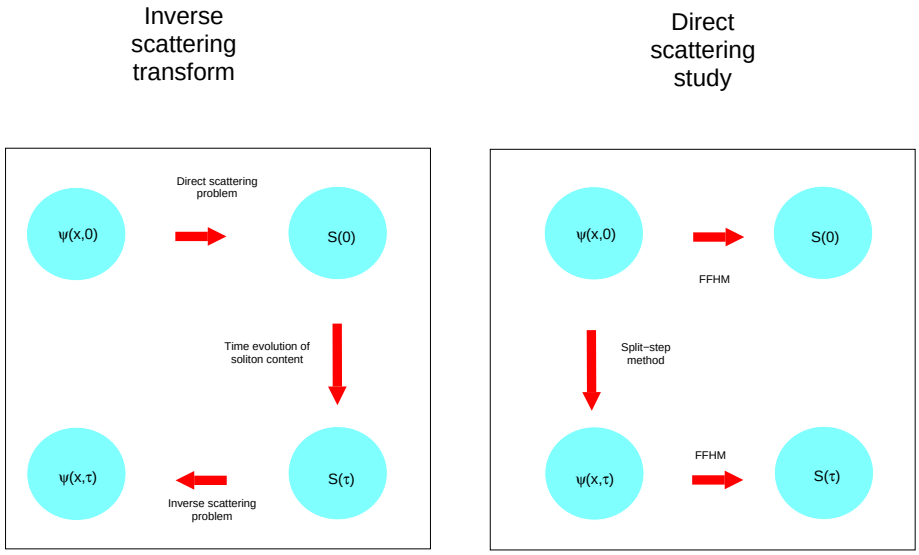

Figure 6.1: *Schematic representations of the inverse scattering transform (a) and the direct scattering study (b).*

oscillating soliton attractors. In Section 6.4 we study the soliton transients that arise in the zero attractor region. Finally in Section 6.5 we study the soliton transients that arise at the onset of chaos in the spatio-temporally chaotic region, followed by a brief summary in Section 6.6.

6.1 Description of the direct scattering study

The direct scattering study is a numerical study of soliton solutions in near-integrable equations. The direct scattering study amounts to the calculation and analysis of the soliton content. The soliton content consists of the discrete eigenvalues of the associated ZS eigenvalue problem. We refer to these eigenvalues as the ZS eigenvalues. The soliton content reveals the number of solitons as well as the characteristics of each soliton while it can be used to calculate the total mass of the radiation. Due to a symmetry of the ZS eigenvalue problem we consider only the upper half of the complex.

The direct scattering study is closely related to the IST method. Figure 6.1 shows a

schematic representation of the IST method and the direct scattering study. In Figure 6.1 (a) we show the representation of the IST method that is used to solve intergrable equations such as the unperturbed NLS equation. The purpose of the IST method is to solve an initial value problem, i.e. to find the solution $\psi(x,\tau)$ for a given initial condition $\psi(x,0)$. The initial scattering data $S(0)$ are found by solving the direct scattering problem. The soliton content forms part of the scattering data. The equations that govern the time evolution of the scattering data are known explicitly, and can be used to calculate the evolved scattering data $S(\tau)$. In particular, in the integrable case the soliton content is time-independent, reflecting the fact that solitons are not altered by interactions with other solitons and radiation. The solution $\psi(x,\tau)$ can be reconstructed through the inverse scattering problem. The IST method is discussed in more detail in Chapter 2.

In Figure 6.1 (b) the schematic representation of the direct scattering study is shown. In this case the initial value problem is solved numerically, i.e. the solution $\psi(x,t)$ is known at $t=0$ and $t=\tau$ at the onset of the direct scattering study. In this case, we are interested in the time evolution of the soliton content. This is due to the fact that, in the near-integrable case, the soliton content is no longer time-independent. The soliton content $S(0)$ and $S(\tau)$ describe the soliton structure of the solution $\psi(x,t)$ at $t=0$ and $t=\tau$ respectively. The time evolution of the soliton content describes the way that the soliton changes, and provides some information about the radiation waves.

The effectiveness of the direct scattering study relies on the ability to interpret the soliton content. We therefore briefly review the relationship between the ZS eigenvalues and solitons in the integrable NLS case. This relationship is discussed in more detail in Chapter 2. We look at three types of soliton content that arise frequently in the direct scattering study of the PDNLS equation, namely *1)* one purely imaginary ZS eigenvalue, *2)* two purely imaginary ZS eigenvalues and *3)* two complex ZS eigenvalues symmetric about the imaginary axis.

One purely imaginary ZS eigenvalue

In the integrable NLS case a single purely imaginary ZS eigenvalue $\zeta = i\eta$ is associated with a quiescent soliton. The amplitude of the soliton is given by $A = 2\eta$ and the width is proportional to $1/A$. One can also obtain the total mass of the soliton and that of the radiation from the conservation law of the mass. These quantities act as indicators of the distribution of energy between the soliton and radiation. Therefore in the direct scattering study, a single purely imaginary ZS eigenvalue reveals the shape and total mass of the soliton and the total mass of the radiation. Since the oscillating soliton attractors consist of an oscillating quiescent soliton that emits radiation, it is no surprise that a single purely imaginary ZS eigenvalue arises in the direct scattering study of these attractors.

Two purely imaginary ZS eigenvalues

In the integrable NLS case two purely imaginary ZS eigenvalues are associated with a breather solution. In Chapter 2 we discussed the behaviour of breathers. In particular we showed that the relative distance of the ZS eigenvalues determine the spatial structure of the breather. However, the behaviour of all breathers is similar during the time when their amplitudes approach their maximum. This behaviour plays an important role in the direct scattering study of the PDNLS equation. An example of the behaviour of breathers during the time when they approach their maximum is illustrated in Figure 6.2. Here we show the breather corresponding to two ZS eigenvalues $\zeta_1 = 0.75i$ and $\zeta_2 = 0.25i$. In Figure 6.2 (a) we show the time evolution of the local maxima of the absolute value of the breather. The shaded area shows the stage where the amplitude of the breather approaches its maximum. In Figure 6.2 (b) we see the solution at $t = 5.65$. At this stage the amplitude of the central soliton increases while its width decreases. As this happens, two lateral waves are formed on opposite sides of the soliton. As time evolves, these waves move away from the soliton, until $t = 2\pi$, where the soliton's amplitude reaches its maximum. The solution at this point

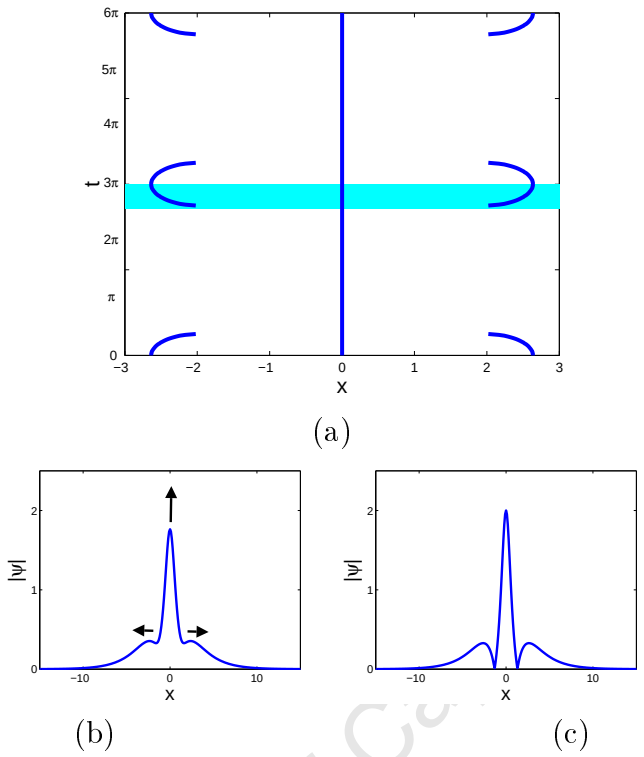

Figure 6.2: *Breather solution corresponding to two purely imaginary ZS eigenvalues* $\zeta_1 = 0.75i$ *and* $\zeta_2 = 0.25i$. *In (a) the spatial profile of the solution is shown. In (b) and (c) the solution is shown for* $t = 5.65$ *and* $t = 2\pi$ *respectively.*

is shown in (c). At this stage the two lateral waves reach their maximum distance from the soliton. Note that the formation of lateral waves of breathers is similar to the formation of radiation waves in oscillating soliton attractors of the PDNLS equation. In the latter case the emission of sufficiently large radiation waves results in the formation of two purely imaginary ZS eigenvalues.

Two symmetric complex ZS eigenvalues

Here we consider a soliton content consisting of two ZS eigenvalues $\zeta_\pm = \pm\xi + i\eta$. In the integrable case this corresponds to two solitons with equal amplitudes $A = 2\eta$ travelling in opposite directions with velocities $V = \pm 4\xi$. Therefore the soliton content reveals the fact that the soliton solution consist of two solitons. The soliton content also reveals the amplitude

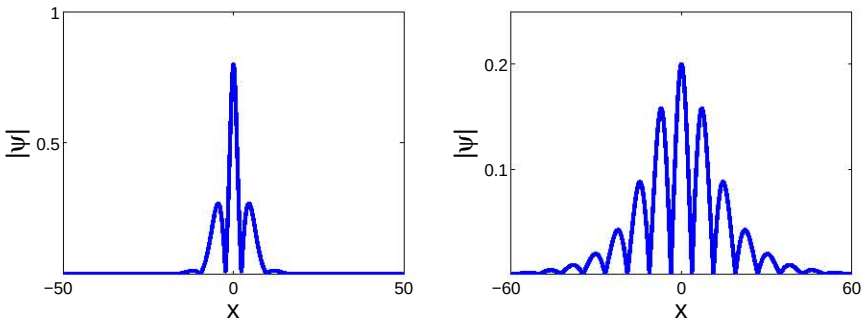

Figure 6.3: *Solutions during the climax of the collision of two colliding solitons. In (a) the solution is shown associated with a large amplitude/velocity ratio* $\eta = 0.2$ *and* $\xi = 0.2$*. In (b) the solution is shown for a small amplitude/velocity ratio with* $\eta = 0.05$ *and* $\xi = 0.2$*.*

and velocity of each. However, the soliton content does not reveal the spatial position of these solitons. This is due to the fact that the soliton content is time-independent. Consequently the same soliton content used to describe two solitons approaching each other is also used to describe two solitons in the process of colliding and two solitons moving away from each other. Within the context of the oscillating soliton attractors, two symmetric complex ZS eigenvalues indicate that the attractor behaves like two moving soliton during the process of collision.

In Chapter 2 we saw that the behaviour of two solitons during collision is determined by the amplitude/velocity ratio $r_{col} = \eta/\xi$. For large ratios the collision results in the formation of a thin soliton with two lateral waves on each side. An example is shown in Figure 6.3 (a), corresponding to the collision that occurs for solitons associated with ZS eigenvalues $\zeta = \pm 0.2 + 0.2i$. For this reason we interpret two symmetric ZS eigenvalues in the complex plane with a large amplitude/velocity ratio as indicators of large lateral waves. similar to those observed in the case of two purely imaginary ZS eigenvalues.

In contrast, for small amplitude/velocity ratios the collision results in the formation of a number of smaller waves next to the lateral waves. An example is shown in Figure 6.3 (b) where we show the solution corresponding to ZS eigenvalues $\zeta = \pm 0.2 + 0.05i$. Instead of the formation of two solitary lateral waves, we see the formation of a wave train on each side of

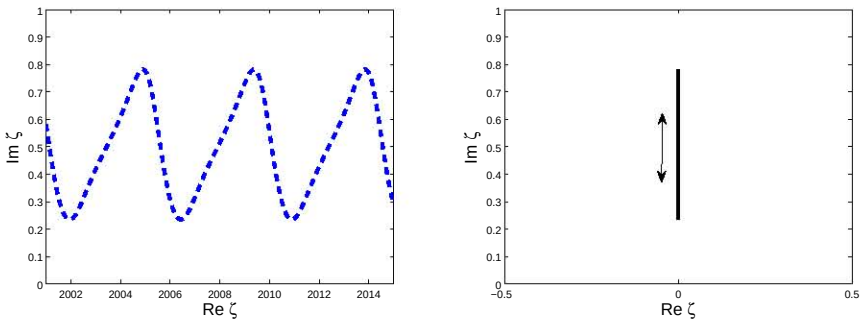

(a) *(b)*

Figure 6.4: *Type I attractor, corresponding to* $\gamma = 0.3$, $h = 0.51$. *The time evolution of the imaginary part of the ZS eigenvalue is shown in (a). In (b) we show the image of the ZS eigenvalue on the complex plane.*

the soliton. In this example each wave train consists of five smaller waves. Note that, in this case, the wave trains formed during the collision of two solitons resemble the radiation wave trains that form in oscillating soliton attractors of the PDNLS equation. In the latter case the formation sufficiently large radiation tails results in the formation of two symmetric ZS eigenvalues in the complex plane with a small amplitude/velocity ratio.

6.2 The soliton structure of soliton attractors

Oscillating soliton attractors consist of a quiescent soliton that oscillates temporally while emitting radiation waves. We calculated the soliton content for a large number of oscillating soliton attractors. We identified four types of oscillating soliton attractors, classified Type I - Type IV, each with a unique soliton structure. To illustrate the behaviour of each type of attractor we fix the damping $\gamma = 0.3$ and change the driving strength h. The characteristic soliton content of each type of attractor is discussed. Once the properties of each type of attractor are established, we discuss the general soliton structure of the oscillating soliton attractors of the PDNLS equation.

Type I attractor

For a fixed damping coefficient $\gamma = 0.3$, Type I attractors arise for driving strengths $0.38 < h < 0.54$. For these attractors the soliton content consists of a single purely imaginary ZS eigenvalue, oscillating on the imaginary axis. Figure 6.4 shows the behaviour of the soliton content for the soliton attractor corresponding to a driving strength of $h = 0.51$. Figure 6.4 (a) shows the time evolution of the imaginary part of the ZS eigenvalue. In Figure 6.4 (b) we plot the range of the ZS eigenvalues on the complex plane, showing the path of the ZS eigenvalue on the imaginary axis.

In the integrable NLS case, a single purely imaginary ZS eigenvalue corresponds to a quiescent soliton. Therefore the soliton content shows that the soliton of a Type I attractor is similar to solitons that arise in the integrable NLS case.

In Chapter 5 we showed that the energy of the radiation that is emitted by oscillating soliton attractors increases with the driving strength. In the integrable NLS case one can get a time-independent measurement of the mass of the radiation from the conservation law (2.24),

$$m_{rad} = m_{total} - m_{soliton} = \int_{-\infty}^{\infty} |\psi(x)|^2 \, dx - 4\sum_{j=1}^{N} \eta_j, \tag{6.1}$$

where the potential $\psi(x)$ has N discrete eigenvalues, each given by $\zeta_j = \xi_j + i\eta_j$. Due to the non-integrability of the PDNLS equation, the total mass of radiation m_{rad} becomes time dependent for the oscillating soliton attractors. In this case it is sensible to define the average radiation mass as

$$\bar{m}_{rad}(\gamma, h) = \frac{1}{T}\int_{0}^{T} m_{rad}(t) \, dt, \tag{6.2}$$

where $\psi(x,t)$ is the Type I attractor that arises for a damping coefficient γ and a driving strength h, $m_{rad}(t)$ is the mass of radiation at time t, and T is the temporal period of the attractor. In Figure 6.5 we show the average radiation mass for Type I attractors that

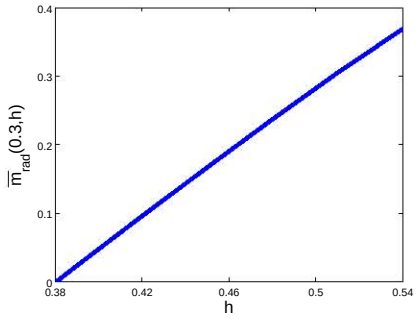

Figure 6.5: *Energy of radiation of Type I attractors for different driving strengths that arises for fixed damping* $\gamma = 0.3$.

arises when the damping is fixed at $\gamma = 0.3$. We see that the average radiation mass is approximately linearly related to the driving strength. Therefore the soliton content reflects the fact that increased driving strengths lead to increases in the energy of radiation emissions.

Type II attractor

For a fixed damping $\gamma = 0.3$, Type II attractors arise for driving strengths $0.54 \leq h < 0.7$. The soliton content of these attractors consist of one oscillating purely imaginary ZS eigenvalue and a pair of two complex ZS eigenvalues that appear and disappear periodically. The pair of ZS eigenvalues is symmetric about the imaginary axis. We refer to them as *side eigenvalues*. Figure 6.6 shows the soliton content of the Type II attractor associated with the driving strength $h = 0.65$. Figure 6.6 (a) shows the time evolution of the imaginary part of the soliton content. We use dotted lines to represent purely imaginary ZS eigenvalues and solid lines to represent ZS eigenvalues with non-zero real parts. We see that the side ZS eigenvalues appear and disappear in the region where the purely imaginary eigenvalue approaches a local minimum. In Figure 6.6 (b) the real part of the discrete spectrum is shown, illustrating the symmetry of the side eigenvalues. Here we see that the side eigenvalues are not formed at the origin, but on the real line at $\zeta \approx \pm 0.4$. In Figure 6.6 (c) we show the range of the ZS eigenvalues in the complex plane. We used a logarithmic scale of the imaginary part of the eigenvalue to emphasize the behaviour of the side eigenvalues.

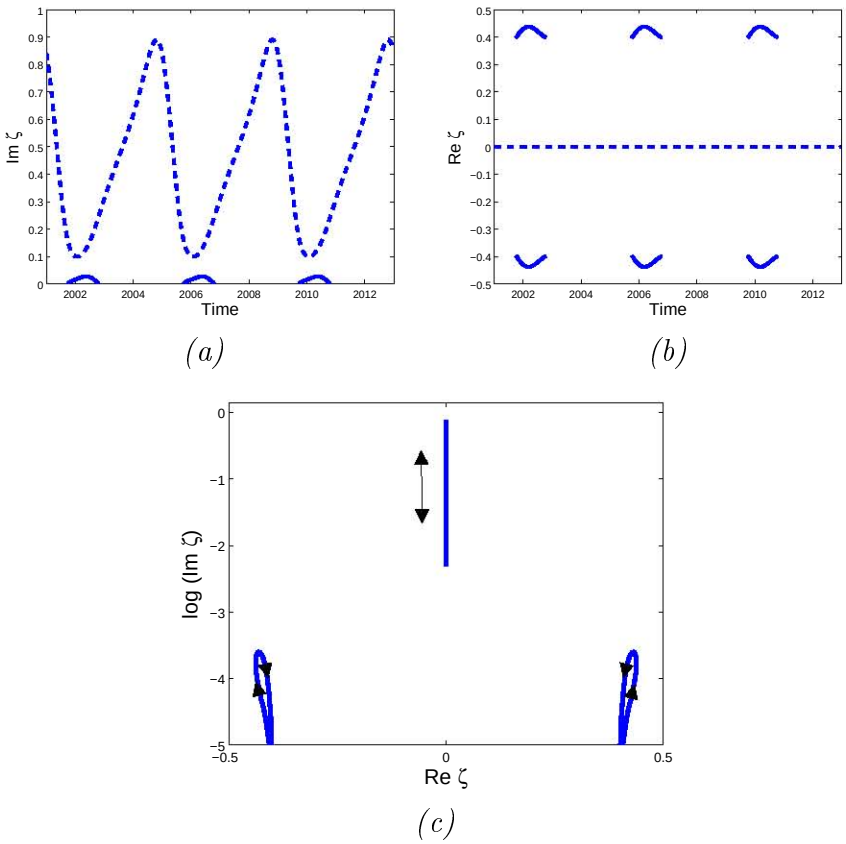

Figure 6.6: *Type II attractor, corresponding to* $\gamma = 0.3$, $h = 0.65$. *The time evolution of the imaginary parts and the real parts of the ZS eigenvalues are shown in (a) and (b) respectively. In (c) the image of the ZS eigenvalues on the complex plane is shown.*

During the lifetime of the side eigenvalues, the soliton content consists of three ZS eigenvalues. In the integrable case this corresponds to a quiescent soliton and two solitons moving in opposite directions with velocities $V = \pm 4\xi$, where the real parts of the side eigenvalues are given by $\pm\xi$. The imaginary parts of the side eigenvalues are small in comparison to the real parts, resulting in a small amplitude/velocity ratio. The side eigenvalues are therefore excited by the formation of larger radiation tails. Indeed, this result is consistent with the results from Section 5.3, showing that increases in driving strength leads to *1)* increases in the amplitude of the radiation waves, *2)* increases in the lifespan of radiation waves and *3)* increases in the frequency of radiation wave formation. All these factors contribute to the formation of fatter radiation tails that are responsible for exciting the side eigenvalues.

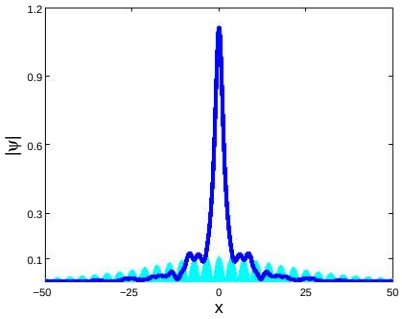

Figure 6.7: *Comparison between the attractor (solid line) and the reconstructed collision of two solitons associated with the side eigenvalues (shaded area).*

To illustrate the relationship between the side eigenvalues and the radiation tail, we consider the Type II attractor that arises for damping and driving $\gamma = 0.3$ and $h = 0.65$ respectively at $t = 2002.35$. At this point in time the soliton content of the attractor includes two side eigenvalues given by $\zeta_{side} \approx \pm 0.43 + 0.03i$. The soliton collision of the *unperturbed NLS equation* associated with the side eigenvalues can be reconstructed. This is done by plugging the side eigenvalues into the solution (2.30) of the integrable NLS equation corresponding to two complex symmetric ZS eigenvalues. For the reconstruction we evaluate the solution (2.30) at $t = 0$, the point where the soliton collision is at its climax. In Figure 6.7 we compare the solution of the attractor at $t = 2002.35$ to the reconstructed soliton collision. We use a solid line for the solution of the Type II attractor and a shaded area for the reconstructed soliton collision. On the interval $-5 \leq x \leq 5$ we see that the reconstructed solution does not fit the attractor's solution well. This shows that the side eigenvalues do not describe the soliton itself. However, outside this interval, the reconstructed solution is similar to the radiation tail of the attractor's solution. This shows that the side eigenvalues correspond to the radiation tail ($|x| > 5$ in this example). In other words, the side eigenvalues are excited by radiation tails with high energy in the form of large total mass.

The side eigenvalues indicate that the oscillating soliton attractor has radiation tails with large total mass, representing a state of high radiation. As driving strength increases, the energy of radiation emissions increases. The effect of larger radiation emissions on the soliton

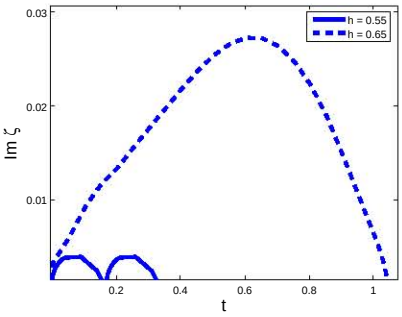

Figure 6.8: *Imaginary parts of the side eigenvalues that arises in Type II attractors corresponding to driving strenghts* $h = 0.55$ *(solid lines) and* $h = 0.65$ *(dotted line).*

content is that both the lifetime and the maximum value of the imaginary part of the side eigenvalues increase. To illustrate this, Figure 6.8 shows the time evolution of the imaginary part of the side eigenvalues associated with Type II attractors that arises for the damping coefficient $\gamma = 0.3$ and driving strengths $h = 0.55$ and $h = 0.65$. The time of each attractor is scaled so that the formation of the side eigenvalue occurs at $t = 0$. We see that the lifetime of the side eigenvalues of the attractor corresponding to $h = 0.55$ is less than 0.4 units of time. The disappearance and reappearance of the side eigenvalues are typical of small side eigenvalues, i.e. side eigenvalues with small imaginary parts. On the other hand the lifetime of the side eigenvalues of the attractor corresponding to $h = 0.65$ is larger than 1 unit of time. It is also clear that the imaginary part of the side eigenvalue of the $h = 0.65$ attractor is much larger than that of the $h = 0.55$ attractor.

Type III attractor

For a fixed damping coefficient $\gamma = 0.3$ Type III attractors arise for driving strengths $0.7 < h \leq 0.775$. The soliton content of Type III attractors consists of *1)* an oscillating purely imaginary ZS eigenvalue *2)* side eigenvalues and *3)* a second purely imaginary ZS eigenvalue that appears and disappears periodically. In Figure 6.9 the soliton content is shown for the $h = 0.77$ attractor. Figure 6.9 (a) shows the time evolution of the purely imaginary part of the ZS eigenvalues. Note that the second purely imaginary eigenvalue, marked with the dotted

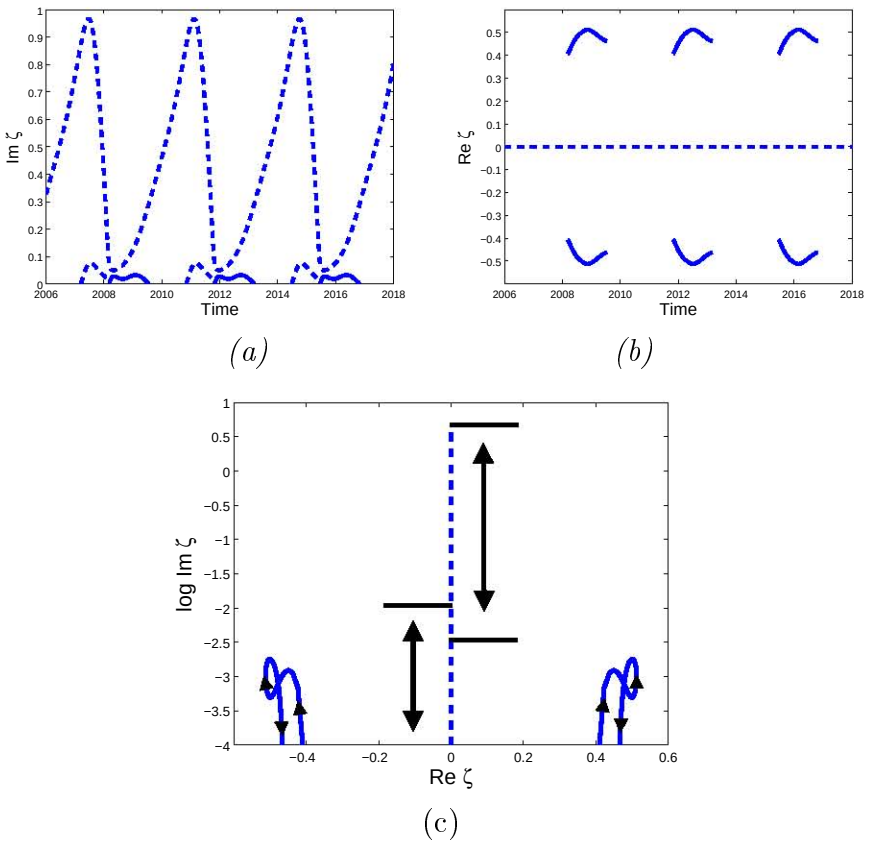

Figure 6.9: *Type III attractor, corresponding to* $\gamma = 0.3$, $h = 0.77$. *The time evolution of the imaginary parts and the real parts of the ZS eigenvalues are shown in (a) and (b) respectively. In (c) the image of the ZS eigenvalues on the complex plane is shown.*

line, appears when the original purely imaginary ZS eigenvalue approaches its maximum. In Figure 6.9 (b) the time evolution of the real part of the discrete eigenvalues are shown. Here we see the side eigenvalues appearing and disappearing periodically. In Figure 6.9 (c) we show the range of the ZS eigenvalues. Since the paths of the purely imaginary ZS eigenvalues overlap, we show the range of the larger (and permanent) purely imaginary ZS eigenvalue with the arrow on the right hand side. We use the arrow on the left to indicate the path of the smaller (and temporary) purely imaginary ZS eigenvalue. Once again we plotted the imaginary axis on the logarithmic scale to emphasize the behaviour of the smaller ZS eigenvalues.

The formation of a second purely imaginary ZS eigenvalue is an indication that the nature

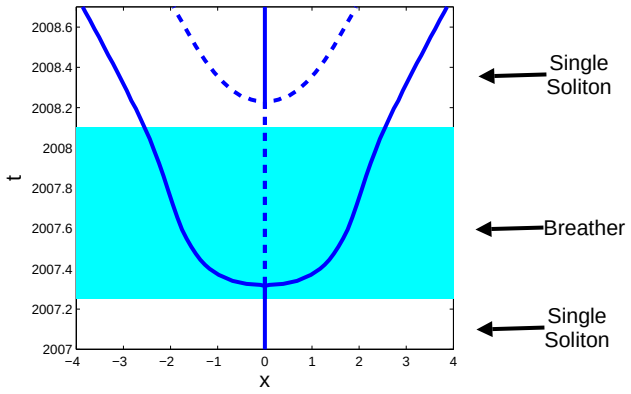

Figure 6.10: *Spatial profile of the imaginary part of the Type III attractor arising when* $\gamma = 0.3$ *and* $h = 0.77$.

of the soliton that arises in a Type III attractor is different to that of the Type I and Type II attractors. During the period where the soliton content consists of two purely imaginary ZS eigenvalues, the soliton and radiation interact to form the breather-like behaviour discussed in the previous section. In particular, during the period of co-existence of the two purely imaginary ZS eigenvalues, the velocity of the radiation waves decreases. This is illustrated in Figure 6.10, showing the spatial profile (as defined in equation (5.9) in Section 5.3) of the imaginary part of the Type III attractor that arises for a damping coefficient $\gamma = 0.3$ and a driving strength of $h = 0.77$. The convention of Chapter 5 is used, namely that solid lines represent valleys, while dotted lines represent hills. The shaded area indicates the period $2007.25 \leq t \leq 2008.1$ where the soliton content consists of two purely imaginary ZS eigenvalues. During this period two radiation waves form at $t = 2007.3$. These radiation waves decelerate on the period $2007.3 \leq t \leq 2007.65$, an indication that the radiation waves resemble the behaviour of the lateral waves that arises for breathers. For $t > 2007.65$ the velocities of the radiation waves grow, ending the breather structure of the soliton. This behaviour coincides with the disappearance of the second purely imaginary ZS eigenvalue.

It is important to note that, during the period where two purely imaginary ZS eigenvalues coexist, it is difficult to distinguish between lateral waves that forms part of a breather and radiation waves that move away from the soliton. For this reason we use the term

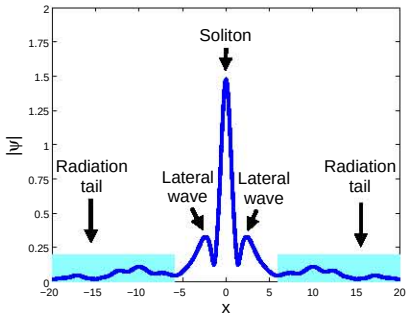

Figure 6.11: *Illustration of the difference between lateral waves and radiation tails. The solution of the attractor are shown for* $\gamma = 0.3$, $h = 0.77$ *and* $t = 2008$.

lateral waves of the attractor to describe these waves during the transition from breathers to radiation waves. These waves are isolated waves situated on opposite sides of the central soliton, clearly discernable from the radiation tail. To illustrate the difference between the lateral waves and the radiation tail we show the solution of the attractor arising for $\gamma = 0.3$ and $h = 0.77$ at $t = 2008$ in Figure 6.11. At the time, the soliton content consists of two purely imaginary ZS eigenvalues. The lateral waves are situated next to the soliton, while the radiation tail is shown in the shaded area. The second purely imaginary ZS eigenvalue describes the behaviour of the lateral waves of the attractor.

The effect of increased driving strength on the soliton content of Type III attractors is that the lifetime of the second purely imaginary ZS eigenvalue increases, as well as its maximum value. As a result, the two purely imaginary ZS eigenvalues move closer to each other when the driving strength is increased. In other words the distance between the two purely imaginary ZS eigenvalues decreases. To demonstrate this, we define $\zeta_1(t)$ as the larger of the two purely imaginary ZS eigenvalues, and $\zeta_2(t)$ as the smaller of the two. Let $d_{min}(\gamma, h)$ represent the minimum distance between the two purely imaginary ZS eigenvalues associated with the soliton attractor that arises when the damping and driving is given by γ and h respectively. In other words we let

$$d(\gamma, h) = \min \{\text{Im } \zeta_1(t) - \text{Im } \zeta_2(t)\}. \tag{6.3}$$

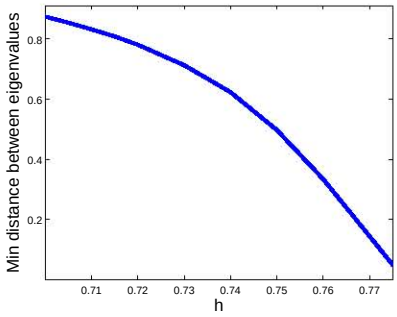

Figure 6.12: *Minimum distance between the two purely imaginary ZS eigenvalues associated with Type III attractors that arises for* $\gamma = 0.3$ *and* $0.7 \leq h \leq 0.775$.

In Figure 6.12 we show the minimum distance $d\,(0.3, h)$ as a function of the driving strength h. Here we see that the distance decreases when the driving strength is increased. As the driving strength approaches $h = 0.78$, the distance between the purely imaginary eigenvalues $d\,(0.3, h)$ decreases. This marks the transition from Type III attractors to Type IV attractors.

Type IV attractor

For $0.775 < h \leq 0.875$, a Type IV attractor arises. The soliton content differs from that of a Type III attractor in the behaviour of the purely imaginary ZS eigenvalues. In this case, the second purely imaginary ZS eigenvalue does not disappear at the origin. Instead, the two imaginary ZS eigenvalues collide. After the collision, the two eigenvalues move into the complex plane, symmetric about the imaginary axis, and disappear into the real line, in a similar way that the side eigenvalues disappear. We refer to these eigenvalues as *splitting eigenvalues*. While this happens, a purely imaginary ZS eigenvalue forms at the origin. In Figure 6.13 the soliton content is shown for $h = 0.87$. The time evolution of the imaginary parts of the ZS eigenvalues is shown in Figure 6.13 (a). In Figure 6.13 (b) we show the time evolution of the real parts of the ZS eigenvalues. Here we see how the splitting eigenvalues move symmetrically in the complex plane. In Figure 6.13 (c) the behaviour of the splitting eigenvalues is shown for $2007 < t < 2008$. Here we see how the two purely imaginary ZS eigenvalues collide on the imaginary axis, and how they move into the complex plane before

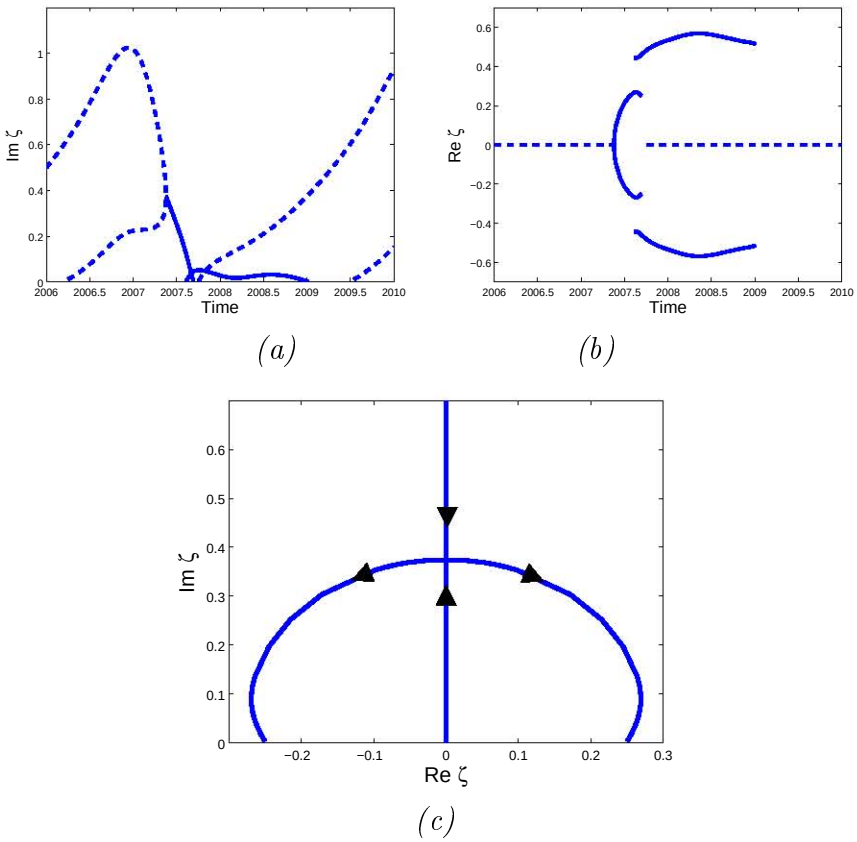

Figure 6.13: *Type IV attractor, corresponding to* $\gamma = 0.3$, $h = 0.87$. *The time evolution of the imaginary parts and the real parts of the ZS eigenvalues are shown in (a) and (b) respectively. In (c) the image of the splitting eigenvalues on the complex plane is shown.*

disappearing into the real line.

From Section 6.1 we know that symmetric ZS eigenvalues with a large amplitude/velocity ratio describe the lateral waves of the oscillating soliton attractor, while symmetric ZS eigenvalues with a small amplitude/velocity ratio describe the radiation tail of the oscillating soliton attractor attractor. The amplitude/velocity ratio changes significantly during the lifetime of the splitting eigenvalues. The amlitude/velocity ratio is very large initially, due to the small real parts at the formation of the splitting eigenvalues. At this time the splitting eigenvalues describe breather-like lateral waves of the Type IV attractor. As the splitting eigenvalues approach the real line, the amplitude/velocity approahes zero. A small amplitude/velocity ratio shows that the splitting eigenvalues describe an entire radiation tail with

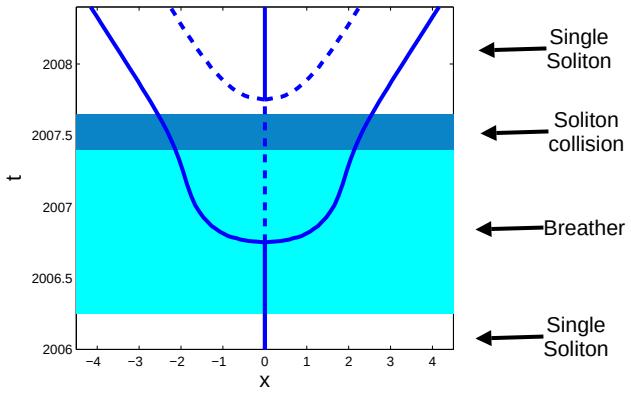

Figure 6.14: *Spatial profile of the imaginary part of the Type IV attractor arising when* $\gamma = 0.3$ *and* $h = 0.87$.

large total mass, and not only the lateral waves. Therefore the splitting eigenvalues describe the transition of the newly-emitted radiation waves from solitary breather-like lateral waves initially to the stage where they are difficult to distinguish from the rest of the radiation tail.

The velocity of the radiation waves indicate the transition described above. This is illustrated in Figure 6.14 where we show the spatial profile (as defined in equation (5.9) in Section 5.3) of the Type IV attractor that arises for $\gamma = 0.3$ and $h = 0.87$. The light shading corresponds to the period where the soliton content consists of two purely imaginary ZS eigenvalues. The dark shading corresponds to the period where the soliton content consists of two symmetric ZS eigenvalues, after the ZS eigenvalues split into the complex plane. During the period where the soliton content consists of two purely imaginary ZS eigenvalues, the behaviour of the radiation waves are similar to that of Type III attractors. This illustrates that the velocity of the lateral waves decreases during the formation of two purely imaginary ZS eigenvalues. However during the formation of the splitting eigenvalues $2007.4 \leq t \leq 2007.6$ the radiation waves accelerate away from the soliton. After the splitting eigenvalues disappear, the radiation waves maintain a constant velocity.

In terms of the scattering data of Type IV attractors, an increase in driving strength h causes the collision of purely imaginary ZS eigenvalues to occur higher on the imaginary axis. The point of collision is an indication of the size of the breather. Collision points situated

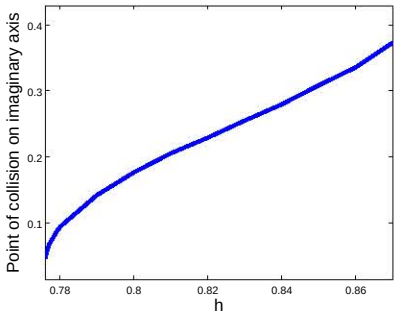

Figure 6.15: *Point of collision of two purely imaginary ZS eigenvalues for different driving strengths.*

higher on the imaginary axis correspond to breathers with larger amplitudes and smaller widths. Figure 6.15 shows the point on the imaginary axis where the collision occurs as a function of the driving strength. We can clearly see that larger driving strength leads to a gigher collision point, corresponding to larger breathers.

General case:

In general, the soliton content of any oscillating soliton attractor exhibits the characteristics of one of the types of attractors described above. We use this fact to categorize all oscillating soliton attractors by the behaviour of their soliton content. Therefore a Type I attractor is an oscillating soliton attractor whose soliton content consists of a single purely imaginary ZS eigenvalue that oscillates on the imaginary axis. A typical example of the behaviour of the soliton content of a Type I attractor is shown in Figure 6.4. The soliton content of a Type II attractor consists of a purely imaginary ZS eigenvalue that oscillates on the imaginary axis along with side eigenvalues that appear and disappear periodically. A typical example of the behaviour of the soliton content of a Type II attractor is shown in Figure 6.6. The soliton content of a Type III attractor consists of an oscillating purely imaginary ZS eigenvalue, side eigenvalues, and a second purely imaginary ZS eigenvalue that appears and disappears periodically. A typical example of the behaviour of the soliton content of a Type III attractor is shown in Figure 6.9. The soliton content of a Type IV attractor consists of splitting

Attractor type	Oscillating imaginary ZS eigenvalue	Side eigenvalues	Second purely imaginary ZS eigenvalue	Splitting eigenvalues
I	✓			
II	✓	✓		
III	✓	✓	✓	
IV		✓	✓	✓

Table 6.1: *Characteristics of the soliton content of the different types of attractors.*

eigenvalues and side eigenvalues. An example is shown in Figure 6.13.

The characteristics of the soliton content of each type of attractor are summarized in Table 6.1. It is important to note the hierarchy of the types of attractor, namely that the complexity of the soliton content increases with the type number. For example the soliton content of a Type II attractor is more complicated than a Type I attractor, since the latter consists of three ZS eigenvalues, while the former consists of only one ZS eigenvalue.

We calculated the type of attractors within the oscillating soliton attractor region. In Figure 6.16 we show the regions of the four different types of attractors. Here II marks Type II attractor region etc. In terms of this attractor chart we can define three damping regimes, namely a small damping regime ($\gamma < 0.27$), an intermediate damping regime ($0.27 \leq \gamma < 0.33$) and a large damping regime ($0.33 \leq \gamma \leq 0.378$). The small damping regime coincides with the zero attractor region. The zero attractor region is bounded below by Type I or Type II attractors. In this regime not all types of attractors arise. The second regime of interest is the intermediate damping regime. For any fixed damping coefficient in this regime we see that all four types of attractors arise. The $\gamma = 0.3$ case study is an example of the behaviour of attractors in this regime. In the large damping regime no Type IV attractors exists. Here the spatio-temporally chaotic region is bounded below by a Type I, Type II or Type III attractor. Below we give a brief description of each regime.

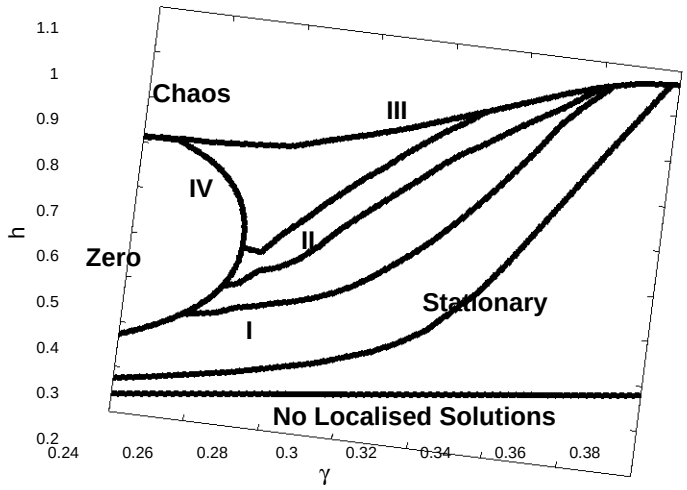

Figure 6.16: *Attractor chart of the* (γ, h) *plane. We see the regions on which the Type I - IV attractors exist.*

Small damping regime $(\gamma < 0.27)$:

In the small damping regime we see that the zero attractor region is bounded below by Type I or Type II attractors. From Chapter 5 we know that the oscillating soliton attractors undergo a period-doubling route to chaos. From the attractor chart it is clear that the period-doubling route to chaos does not change the soliton structure of the oscillating soliton attractors. This raises the question: do the period-doubling bifurcations that lead to chaos affect the behaviour of the soliton content? In Section 6.3 this question is addressed.

Another noteworthy observation is that, for damping coefficients $0.25 \leq \gamma < 0.27$ the zero attractor region is bounded below by Type I or Type II attractors, while it is bounded above by Type IV attractors. This suggests that, in the zero attractor region, unstable oscillating soliton solutions exist. Since we use direct simulation to generate the attractors, we are restricted to the study of stable solutions. However solitons arise as transients in the zero attractor region. In Section 6.4 we apply the direct scattering study to investigate the restabilization of the oscillating soliton attractors in the regime $0.25 \leq \gamma < 0.27$.

Intermediate damping regime $(0.27 \leq \gamma \leq 0.33)$**:**

In this regime we see the hierarchy of the types of attractors, namely that larger driving strength leads to more complicated soliton structures. The Type I attractor region is bounded below by the stable attractor region. The Type I attractor region is bounded above by the Type II attractor region. This reflects the fact that radiation emissions increase for larger driving strengths, resulting in the formation of larger radiation tails. Type II region is bounded above by the Type III attractor region. This indicates the fact that the larger lateral waves is formed. It also indicates that the behaviour of the lateral waves change, resulting in breather-like behaviour during the period when the soliton increases in amplitude. Type III region is bounded above by Type IV attractor region. This shows that, for larger driving strengths, large lateral waves form, resulting in the excitation of splitting eigenvalues. The effect of driving strength on the soliton content of the oscillating soliton attractors were demonstrated in the $\gamma = 0.3$ case study above.

Large damping regime $(0.23 \leq \gamma \leq 0.378)$**:**

In the large damping regime there exists no Type IV attractors. Therefore the spatio-temporally chaotic attractor region is bounded below by Type I, Type II or Type III attractors. This suggests that there may be a different mechanisms involved in the transition from soliton attractors to spatio-temporally chaotic attractors. This is investigated in Section 6.5.

6.3 The effect of period-doubling bifurcations on the soliton content of attractors

The relationship between the temporally chaotic attractors and the zero attractor region are investigated in this section. In Chapter 5 we showed that, for any fixed damping $\gamma < 0.27$, an incremental increase in driving strength h leads to a period-doubling route to temporally

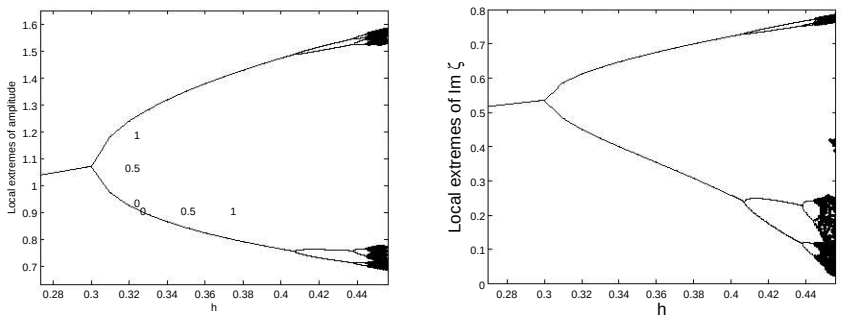

(a) (b)

Figure 6.17: *Period-doubling route to chaos of the oscillating soliton attractors for fixed damping* $\gamma = 0.26$. *In (a) the local extremes of the amplitudes are shown. In (b) the local extremes of the purely imaginary ZS eigenvalues are shown.*

chaotic soliton attractors. If the driving is increased further, the zero attractor arises. The period-doubling route to chaos was studied in detail by Barashenkov and coworkers [20] who showed that the chaos is caused by a homoclinic explosion. The aim of this section is to study the effect that the period-doubling route to chaos has on the soliton content of the oscillating soliton attractors. The purpose of this analysis is to study the transition from temporally chaotic attractors to the zero attractor.

The time evolution of the soliton content of the period-doubling attractors undergoes the same period-doubling route to chaos as the attractors themselves. To illustrate this we calculated the time evolution of the ZS eigenvalues for different driving strengths when the damping is fixed at $\gamma = 0.26$. The results are shown in Figure 6.17. In Figure 6.17 (a) we show the local extremes of the amplitudes of oscillating soliton attractors for different driving strengths. In Figure 6.17 (b) we show the local extremes of the purely imaginary ZS eigenvalues of the same oscillating soliton attractors. At $h = 0.3$ the Hopf bifurcation results in the formation of 1-period oscillating soliton attractors. At $h = 0.407$ the first period-doubling bifurcation occurs. The effect of the bifurcations and the resulting temporal chaos are observed in the behaviour of both the amplitude and the soliton content of the oscillating soliton attractor.

In the integrable NLS case, the total mass of the solitons within a solution is conserved,

and is given by

$$m_{sol} = 4\sum_{n=1}^{N} \eta_n,$$

where $\eta_1, \cdots, \eta_N$ are the imaginary parts of the N associated ZS eigenvalues. In the perturbed case, the integrability is broken, and the mass of the soliton part of the solution becomes time dependent, i.e.

$$m_{sol}(t) = 4\sum_{n=1}^{N} \eta_n(t). \tag{6.4}$$

The attractors that bound the zero attractor region from below are Type I or Type II attractors. In each case, the oscillating soliton attractor consists of a quiescent soliton and radiation. For Type II attractors, we know that the side eigenvalues describe the radiation tail, and not the soliton itself. Therefore, in order to measure the energy of the soliton, we modify equation (6.4) to only take the purely imaginary ZS eigenvalue into account, giving

$$m_{TII}(t) = 4\eta_{im}, \tag{6.5}$$

where η_{im} is the imaginary part of the purely imaginary ZS eigenvalue $\zeta = i\eta_{im}$. The subscript in (6.5) indicates that the modified mass equation applies to Type II attractors. For Type I attractors equations (6.4) and (6.5) are equivalent. In order to study the formation of the zero attractor region, we analyze the minimum soliton mass, defined as

$$m_{min}(\gamma, h) = \min\{m_{TII}(t)\}.$$

This represents the minimum energy of the soliton part of the attractor that arises when the damping and driving strengths are given by γ and h respectively. In other words the minimum soliton mass of an oscillating soliton attractor represents the point when the soliton is at its weakest.

For any fixed damping $\gamma = \gamma_0$, the function $m_{min}(\gamma_0, h)$ becomes a function of the driving

strength h only. In this case an increase in the driving strength leads to a smaller minimum soliton mass, provided that the driving strength remains in the Type I or Type II attractor region. In other words the derivative

$$\frac{dm_{min}(\gamma_0, h)}{dh} < 0 \tag{6.6}$$

For $\gamma < 0.27$, we argue that this relationship is responsible for the formation of the zero attractor region as follows: Oscillating soliton attractors exist as the result of a balance between energy fed by the driver and energy lost due to dissipation [20]. The energy is fed into the solution through the soliton. This is obvious from the fact the radiation waves are both dispersive and dissipative. We argue that, for the driver to pump enough energy to balance the energy lost through dissipation, the energy of the soliton (i.e. its total mass) should exceed a critical mass throughout the propagation of the attractor. This critical mass depends on the damping coefficient γ. From Chapter 5 we know that the minimum energy of an attractor decreases when the driving strength is increased. If the driving strength is increased beyond a critical point, the minimum soliton mass decreases below the critical mass. The result is that the driver loses its ability to feed enough energy into the system to compensate for the energy loss through dissipation, leading to the zero solution to act as the attractor. This critical driving strength represents the lower boundary of the zero attractor region.

The period-doubling bifurcations influence the relationship between the minimum soliton mass and driving strength. For any fixed $\gamma_0 < 0.27$ let h_{pd} represent the critical driving strength where the first period-doubling bifurcation occurs. Let h_1 and h_2 be driving strengths within the oscillating soliton attractor region satisfying

$$h_1 < h_{pd} < h_2. \tag{6.7}$$

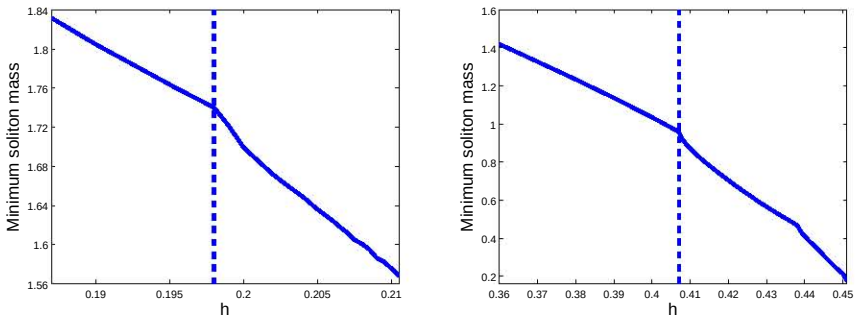

(a) *(b)*

Figure 6.18: *The minimum soliton mass for different driving strengths when the damping is fixed at (a)* $\gamma = 0.15$ *and (b)* $\gamma = 0.26$.

Then the following inequality holds:

$$\left.\frac{dm_{min}\left(\gamma_0, h\right)}{dh}\right|_{h=h_2} < \left.\frac{dm_{min}\left(\gamma_0, h\right)}{dh}\right|_{h=h_1}. \tag{6.8}$$

Since both derivatives are negative, this inequality implies that the function $m_{min}\left(\gamma_0, h\right)$ decreases faster after the period-doubling bifurcation occurs. We illustrate the inequality (6.8) in Figure 6.18. In Figure 6.18 (a) and (b) we show the minimum soliton mass that arises for different driving strengths when the damping is fixed at $\gamma = 0.15$ and $\gamma = 0.26$ respectively. Note that, in both cases, the minimum soliton mass has a negative slope. The vertical lines indicate the critical driving strength h_{pd} where the attractor undergoes the first period-doubling bifurcation. We can see that, in both cases, the function m_{min} decreases faster, confirming the validity of inequality (6.8).

The inequality (6.8) shows that the minimum soliton mass decreases faster after the period-doubling bifurcations occur. Earlier we argued that the destabilization of the oscillating soliton attractors is related to the minimum soliton mass. In particular, we argued that the oscillating soliton attractor is destabilized when the minimum soliton energy decreases beyond a critical mass. Within this argument the faster rate of decrease associated with the inequality (6.8) means that the minimum soliton energy required to destabilize the oscillating soliton attractor is obtained faster. That is, as a result of the period-doubling bifurcations,

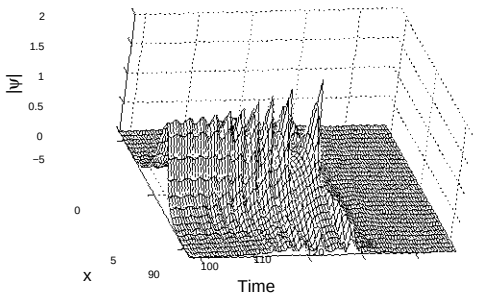

Figure 6.19: *A typical heteroclinic orbit that arises in the zero attractor region. Here* $\gamma = 0.2$ *and* $h = 0.75$.

a smaller driving strength is required to destabilize the oscillating soliton attractor. One can therefore think of the period-doubling route to chaos as a catalyst for the formation of the zero attractor region associated with increased driving strength. ‘

6.4 Soliton transients of the zero attractor

The study of soliton transients in the zero attractor region is motivated by the attractor chart Figure 6.16 that shows the different types of oscillating soliton attractors. Firstly, the chart shows that, in the regime $0.25 \leq \gamma \leq 0.27$, the zero attractor region is bounded below by Type I or Type II attractors and is bounded above by Type IV attractors. The soliton transients give insight into the transition from a Type I or Type II to a Type IV attractor. Another reason for studying the soliton transients is the fact that, for $\gamma \leq 0.25$, the spatio-temporally chaotic region is bounded below by the zero attractor region. Soliton transients arise in both these cases. These transients may give insight into the transition from the zero attractor region to the spatio-temporally chaotic attractor. This transition is investigated in Section 6.5.

We start the discussion of the soliton transients with a typical example of a soliton transient that forms in the heteroclinic orbit in the zero attractor region. In the zero attractor region the heteroclinic orbit, defined in equations (5.5) - (5.6) approaches the zero solution

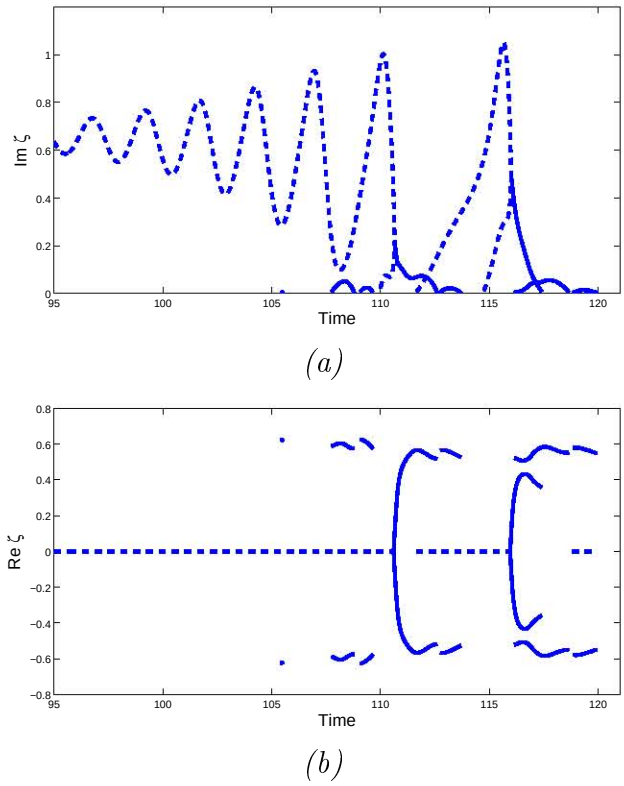

Figure 6.20: *The soliton content of the heteroclinic orbit that arises when* $\gamma = 0.2$ *and* $h = 0.75$. *The imaginary and real parts of the soliton content is shown in (a) and (b) respectively.*

as $t \to \infty$. Figure 6.19 shows the heteroclinic orbit that arises when the damping and driving strengths are given by $\gamma = 0.2$ and $h = 0.75$ respectively. In this case the soliton transient is defined for $t \leq 117$. The soliton transient consists of an oscillating soliton. The amplitudes of the hills increase and the amplitudes of the valleys decreases as time approaches $t = 117$, resulting in an increase in the magnitude of oscillations. After $t = 117$ the heteroclinic orbit rapidly decays to the zero attractor.

In order to study the soliton transients, we applied the direct scattering study to the soliton transients. This allows us to compare the behaviour of the soliton transients to those of the oscillating soliton attractors. Since the magnitude of oscillations of the soliton transients increases until the solution decays to zero, we applied the scattering data by calculating the soliton content during the final oscillation of the soliton transient. This is where the

soliton content is most complex. To illustrate our application of the direct scattering study we continue the example of the soliton transient that arises when the damping and driving is $\gamma = 0.2$ and $h = 0.75$ respectively. In Figure 6.20 we show the soliton content of the heteroclinic orbit. On the interval $t < 105$, the orbit behaves like a Type I attractor. For $105 < t < 110$, the orbit behaves like a Type II attractor, due to the formation of the side eigenvalues. This is followed by a brief period $110 < t < 117$ where the orbit behaves like a Type IV attractor. During the period where the heteroclinic orbit decays to zero $117 < t < 120$ the soliton content also decays until it consists of the empty set for $t > 120$. For our application of the direct scattering study, we only look at the behaviour of the soliton content during the final (and largest) oscillation that occurs, in this example the interval $114 < t < 117$. Therefore, since the soliton content behaves like that of a Type IV attractor during the final oscillation, the soliton transient is classified as a Type IV transient.

Calculations show that soliton transients exhibit the behaviour of the oscillating soliton attractors. Figure 6.21 shows the transient chart of the zero attractor region. Here II indicates the Type II transient region etc. The transient chart shows that larger driving strengths lead to more complicated soliton structures. The soliton content during the final oscillation represents the state of the soliton that is required to destabilize the soliton transient. The radiation emissions of a Type I transient are small relative to the radiation emissions of a Type II transient. This is due to the fact that the side eigenvalues are excited by a large radiation tails. Likewise, the radiation emissions of a Type IV attractor are large relative to those of a Type II transient. This is due to the formation of large lateral waves that excite the splitting eigenvalues. It is interesting to note that the spatio-temporally chaotic region is bounded below by Type IV transients in the small damping regime ($\gamma < 0.25$).

The transient chart presents an intuitive understanding of the behaviour of heteroclinic orbits in the zero attractor region. Oscillating soliton attractors consist of solitons that balance the energy pumped into the soliton through driving with the energy leaked through radiation emissions. For the soliton transients in the zero attractor region there are always an

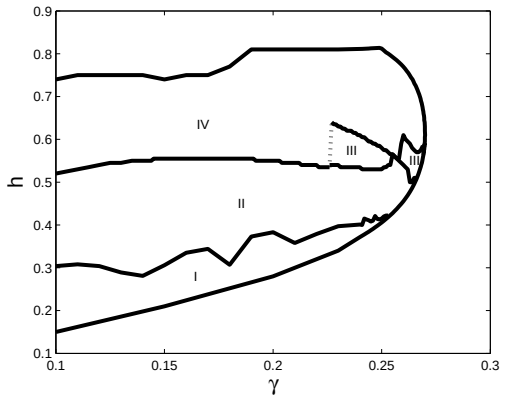

Figure 6.21: *The four types of soliton behaviour observed before the soliton decays to the zero solution.*

imbalance between these energies. Initially the energy pumped into the soliton exceeds the energy leaked through radiation. The result of this imbalance is the growth of the magnitude of oscillations. This growth leads to an increase in the energy of the radiation emissions. This continues until the soliton transient reaches a point where the energy leaked through radiation exceeds the energy pumped into the system, resulting in the decay of the solution to zero. Therefore the transient chart shows that, for larger driving strengths, larger radiation emissions are required to initiate the decay of the heteroclinic orbit to the zero attractor.

The argument above provides some insight into the restabilization of the oscillating soliton attractor in the regime $0.25 \leq \gamma \leq 0.27$. An increase in driving strength has two effects on the soliton transient. Firstly it increases the magnitude of oscillations, resulting in a smaller minimum soliton mass. From the previous section we know that this decrease in minimum soliton mass acts as a destabilizing agent, resulting in the decay to zero that is associated with the zero attractor region. Secondly, the zero attractor chart Figure 6.21 shows that larger driving strengths leads to larger radiation emissions of the soliton transients. This means that larger radiation emissions are required to destabilize the soliton transient. In other words larger energy losses through radiation are required to unbalance the energy pumped into the system. The restabilization occurs when the increase in energy lost through radiation is no longer sufficiently large to exceed the energy gained through the driving.

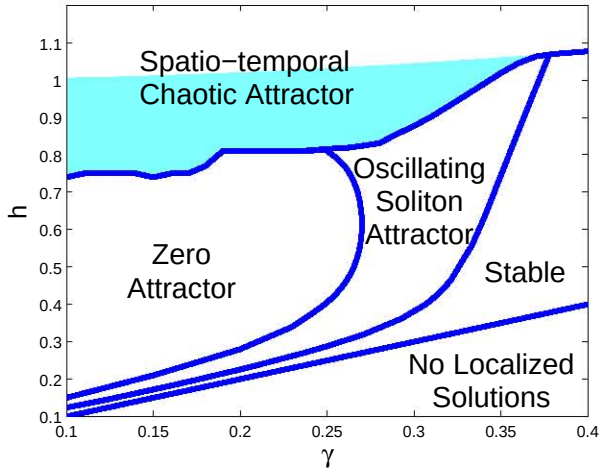

Figure 6.22: *Attractor chart. The shaded area is where the stable zero attractor region and the spatio-temporally chaotic attractor region overlap.*

6.5 Soliton transients of spatio-temporally chaotic attractors

Spatio-temporally chaotic attractors arise when the driving strength h is large relative to the damping coefficient γ. In this case the energy of the soliton gained through the parametric pumping exceeds the energy lost through dissipation. The resulting increase in energy leads to the formation of multiple solitons, leading to the solution to spread across the spatial domain.

A related problem is the stability of the zero solution. The zero solution is unstable whenever the driving strength exceeds the critical driving strength $h_c = \sqrt{1+\gamma^2}$. A consequence of this instability is that any localized solution in the region $h > h_c$ is unstable. This instability is also responsible for the formation of spatio-temporally chaotic attractors. However, the criterion $h > h_c$ is not a necessary condition for the formation of spatio-temporally chaotic attractors. In particular, for damping coefficients $\gamma < 0.378$ there exist a region where the spatio-temporally chaotic attractors coexists with stable zero solutions. This is shown in the attractor chart in Figure 6.22. The shaded area shows the region where the spatio-temporally

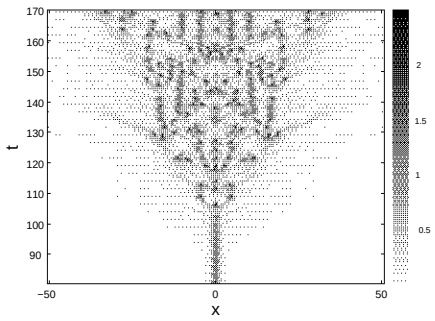

Figure 6.23: *An example of the onset of spatio-temporal chaos for the heteroclinic orbit that arises for damping coefficient* $\gamma = 0.2$ *driving strength* $h = 0.85$.

chaotic attractors arise in spite of a stable zero solution, i.e. where $h < h_c$. Note that, in the regime $\gamma < 0.378$, the spatio-temporally chaotic attractor is bounded by the oscillating soliton attractor region or the zero attractor region.

The purpose of this section is to apply the direct scattering study to the heteroclinic orbits that give rise to the spatio-temporally chaotic attractors. The direct scattering study investigates the role of the soliton and radiation in the formation of chaos. The heteroclinic orbits in the spatio-temporal chaotic region have soliton transients, similar to the case of the zero attractor region discussed in the previous section. Therefore our application of the direct scattering study is identical to the latter analysis, namely the calculation of the soliton content of the transient that arises at the onset of chaos. In particular, we study the heteroclinic orbits that form near the lower boundary of the spatio-temporally chaotic region. An example of a typical heteroclinic orbit that arises in the spatio-temporally chaotic region is shown in Figure 6.23 for the case of damping coefficient $\gamma = 0.2$ and driving strength $h = 0.85$. Here we see that a soliton transient arises for $t < 108$. At this point, spatio-temporal chaos is formed through the formation of multiple solitons. For our application of the direct scattering study, we calculate the soliton content during the final oscillation of the soliton transient $105 \leq t \leq 108$ to investigate the behaviour of soliton and radiation at the onset of chaos.

The numerical results reveal five different types of transient regimes, based on the be-

haviour of their corresponding soliton content. These regimes are classified as the small damping regime, the single-split regime, the double-split regime, the no-split regime and the large damping regime. It is appropriate to describe each regime through an example. Once the characteristics of each regime are described, we proceed to describe the role of the soliton and radiation in the formation of spatio-temporal chaotic attractors.

Small damping regime ($\gamma \leq 0.21$)

The behaviour of the soliton content of the transients in the small damping regime differs from that of the oscillating soliton attractors. In Figure 6.24 we show the results for the heteroclinic orbit that arises for damping coefficient $\gamma = 0.2$ and driving strength $h = 0.802$. In Figure 6.24 (a) and (b) we show the time evolution of the real and imaginary parts of the ZS eigenvalues respectively. At $t \approx 114$ we see the splitting of two purely imaginary ZS eigenvalues into the complex plane in a similar way that Type IV attractors split into the complex plane. However, instead of disappearing into the real axis, the eigenvalues remain in the complex plane, and move towards the imaginary axis. This is followed by the formation of multiple purely imaginary ZS eigenvalues when $t > 116$. The motion of the splitting eigenvalues in the complex plane is shown in Figure 6.24 (c). Here we can clearly see the unusual behaviour of the splitting eigenvalues. In Figure 6.24 (d) we show the solution at the onset of chaos $t = 116$. Note that the amplitude of the soliton is small in comparison to that of the lateral waves.

The soliton content shows that the lateral waves are instrumental in the formation of chaos. The fact that the ZS eigenvalues split into the complex plane is an indication that the lateral waves move away from the original soliton during this period. The return of the ZS eigenvalues to the imaginary axis indicates the fact that, during this time, the velocities of the lateral waves decrease until they becomes quiescent. The fact that the ZS eigenvalues remain in the complex plane indicates that the lateral waves of the transient solitons in this regime are larger than the lateral waves of Type IV attractors.

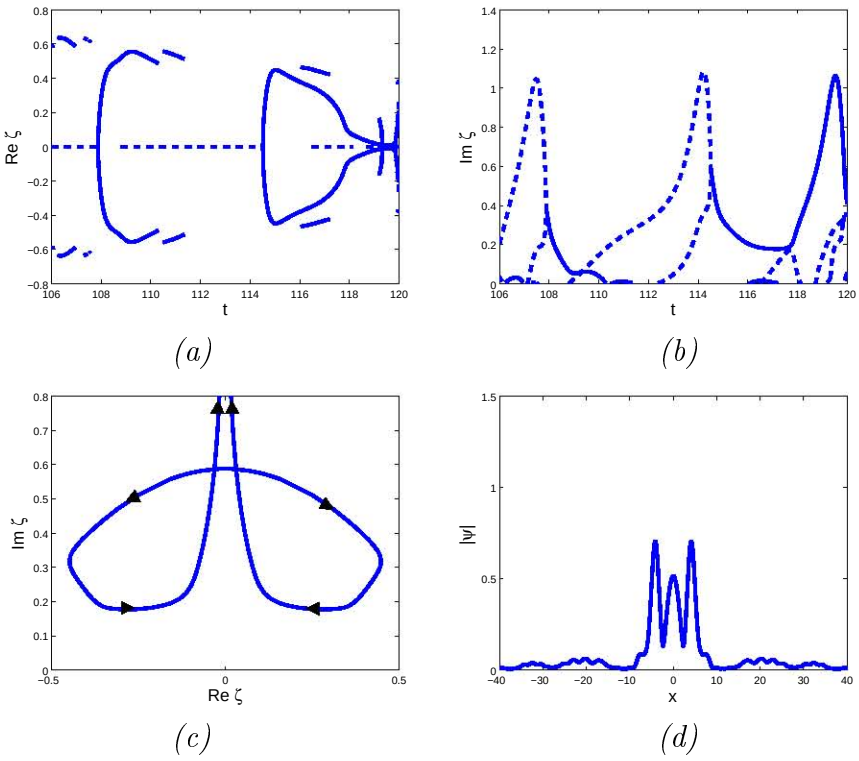

Figure 6.24: *Onset of chaos for the heteroclinic orbit for* $\gamma = 0.2$ *and* $h = 0.802$. *We show the time evolution of the real (a) and imaginary (b) parts of the ZS eigenvalues, the behaviour of the splitting eigenvalues (c) and the solution at the onset of chaos* $t = 116$ *(d).*

Single splitting regime $(0.21 \leq \gamma \leq 0.292)$

In the single-splitting regime, the soliton content of the transients behaves like a Type IV attractor. As an example, we consider the transient that arises in the case when the damping coefficient is $\gamma = 0.24$ and the driving strength is $h = 0.812$. The results are shown in Figure 6.25. In Figure 6.25 (a) and (b) the time evolution of the real and imaginary parts of the soliton content are shown respectively. At $t \approx 158$ the eigenvalues split and disappear into the real line at $t \approx 160$. Thereafter the formation of multiple ZS eigenvalues marks the onset of spatio-temporal chaos. In Figure 6.25 (c) we show the motion of the splitting eigenvalues in the complex plane. It is clear that the splitting eigenvalues are similar to that of a Type IV attractor. In Figure 6.25 (d) we show the solution at $t = 160$. As was the case in the small damping regime example, the soliton is small in comparison to the lateral waves

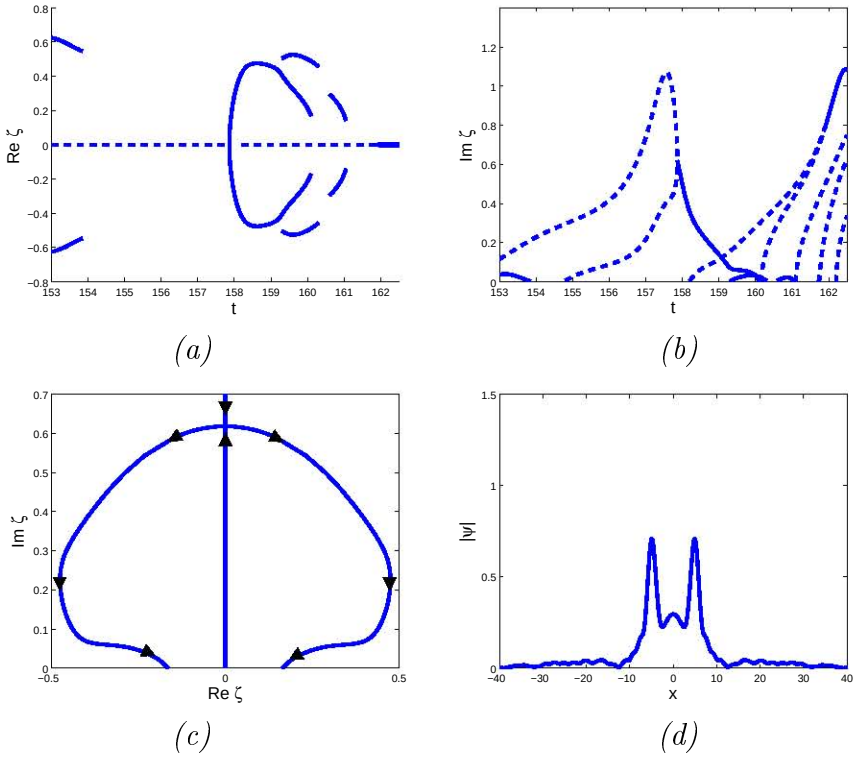

Figure 6.25: *Onset of chaos for the heteroclinic orbit for* $\gamma = 0.24$ *and* $h = 0.812$. *We show the time evolution of the real (a) and imaginary (b) parts of the ZS eigenvalues, the behaviour of the splitting eigenvalues (c) and the solution at the onset of chaos* $t = 160$ *(d).*

at the onset of chaos.

The behaviour of the soliton content shows that, in the single-splitting regime, the lateral waves resemble the lateral waves of Type IV attractors. In other words they are sufficiently large to excite the splitting eigenvalues, and they move away from the soliton with increased velocity during this process. The fact that the ZS eigenvalues disappear into the real line is an indication that the lateral waves are weaker than those of the small damping regime. Even so, their role is still crucial in the formation of chaos. This is illustrated by the fact that the central soliton is very small at the onset of chaos, as is shown in Figure (6.25) (d).

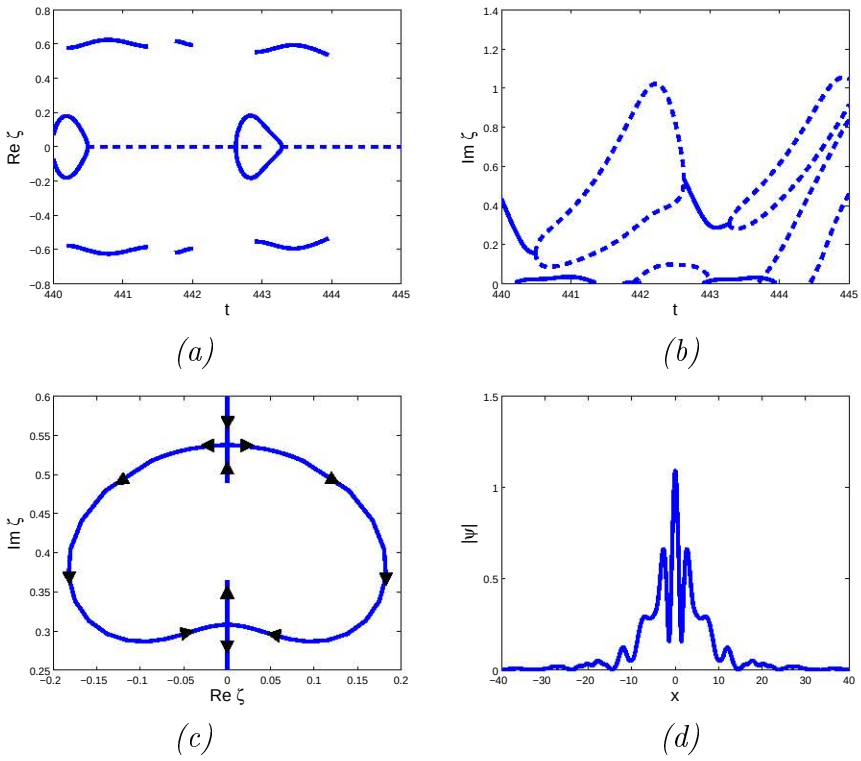

Figure 6.26: *Onset of chaos for the heteroclinic orbit for* $\gamma = 0.32$ *and* $h = 0.93$. *We show the time evolution of the real (a) and imaginary (b) parts of the ZS eigenvalues, the behaviour of the splitting eigenvalues (c) and the solution at the onset of chaos* $t = 443$ *(d).*

Double splitting regime $(0.292 < \gamma \leq 0.347)$

The soliton content of transients in the double-splitting regime is characterized by a double-split of the splitting eigenvalues. An example is given by the transient that arises for the damping coefficient $\gamma = 0.32$ and driving strength $h = 0.93$. The results are shown in Figure 6.26. In Figure 6.26 (a) and (b) the time evolution of the real and imaginary parts of the soliton are shown respectively. Here we see that, at $t \approx 442.5$ the ZS eigenvalues split into the complex plane. However, instead of disappearing into the real axis, they return to the imaginary axis. At $t \approx 443.1$ the ZS eigenvalues collide on the imaginary axis. After the collision they split onto the imaginary axis to form two purely imaginary ZS eigenvalues (hence the name double splitting). In Figure 6.26 (c) we show the motion of the splitting ZS eigenvalues in the complex plane. Notice that, after splitting, the real parts of the ZS

eigenvalues remain relatively close to the imaginary axis (as compared to the previous two examples). In Figure 6.26 (d) we show the solution at $t = 443$ at the onset of chaos. Notice that, in contrast to the previous examples, the amplitude of the soliton is large in comparison to the amplitudes of the lateral waves.

The soliton content reveals that the lateral waves are weaker than those of the smaller damping regimes. During the splitting of the ZS eigenvalues, the amplitude/velocity ratio remains large. In this sense the double-splitting eigenvalues are the opposite of side eigenvalues, since side eigenvalues always maintain a small amplitude/velocity ratio. The double-splitting eigenvalues indicate the fact that the lateral waves remains near the central soliton, in contrast to the smaller damping cases where the lateral waves move away from the central soliton with increasing velocities. As the role of the lateral waves becomes smaller, the role of the central soliton becomes bigger.

No-splitting regime $(0.347 < \gamma \leq 0.378)$

In the no-split regime, purely imaginary eigenvalues remain on the imaginary axis. In Figure 6.27 we show the results for the transient that arises when $\gamma = 0.35$ and $h = 1.019$. In (a) and (b) we show the time evolution of the real and imaginary parts of the soliton content respectively. At $t = 870$ we see two purely imaginary ZS eigenvalues. The smaller of these eigenvalues does not disappear or collide, but remains on the imaginary axis until the onset of chaos at $t = 873.5$. In Figure 6.27 (c) we show the solution at the onset of chaos $t = 873.5$. Here we see that the amplitude of the soliton is large in comparison to the amplitudes of the radiation waves. Note also that the lateral waves are not isolated, but form part of a radiation wave train consisting of three large radiation waves each.

The soliton content reveals that the role of the lateral waves is much smaller than in the smaller damping regimes. The fact that the ZS eigenvalues do not split indicates that the radiation waves do not move away from the central soliton. The result is the formation of a number of smaller quiescent radiation waves. This is in stark contrast to the formation of

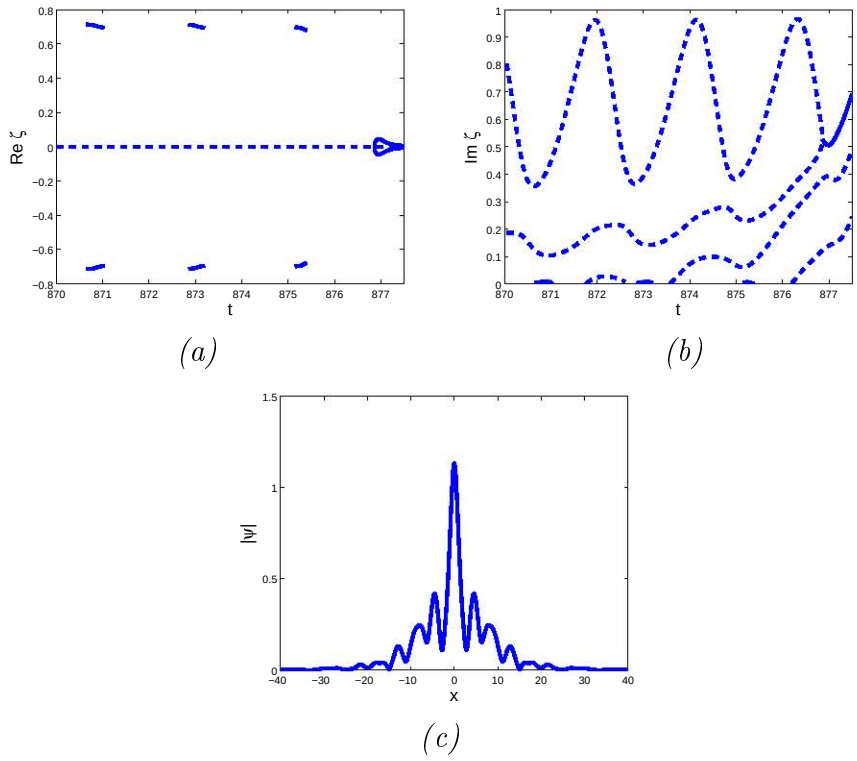

Figure 6.27: *Onset of chaos for the heteroclinic orbit for* $\gamma = 0.35$ *and* $h = 1.019$. *We show the time evolution of the real (a) and imaginary (b) parts of the ZS eigenvalues and the solution at the onset of chaos* $t = 873.5$ *(d).*

large isolated lateral waves in the small and single-splitting regimes.

Large damping regime ($\gamma > 0.378$)

In the large damping regime, the zero attractor is unstable, resulting in the formation of chaos. In Figure 6.28 we show the results for the spatio-temporal attractor that arises in the case where the damping coefficient is $\gamma = 0.4$ and the driving strength is $h = 1.1$. In Figure 6.28 (a) we show the solution on the interval $350 \leq t \leq 450$. It is important to note that, in this case, the soliton does not oscillate during the transient. This is due to the fact that, in the large damping regime, the spatio-temporal chaotic region is bounded below by the stable ψ^+ soliton. Therefore no radiation is emitted. At $t \approx 430$ the additional solitons have spread across the spatial interval. In particular, the two lateral wave trains approach the

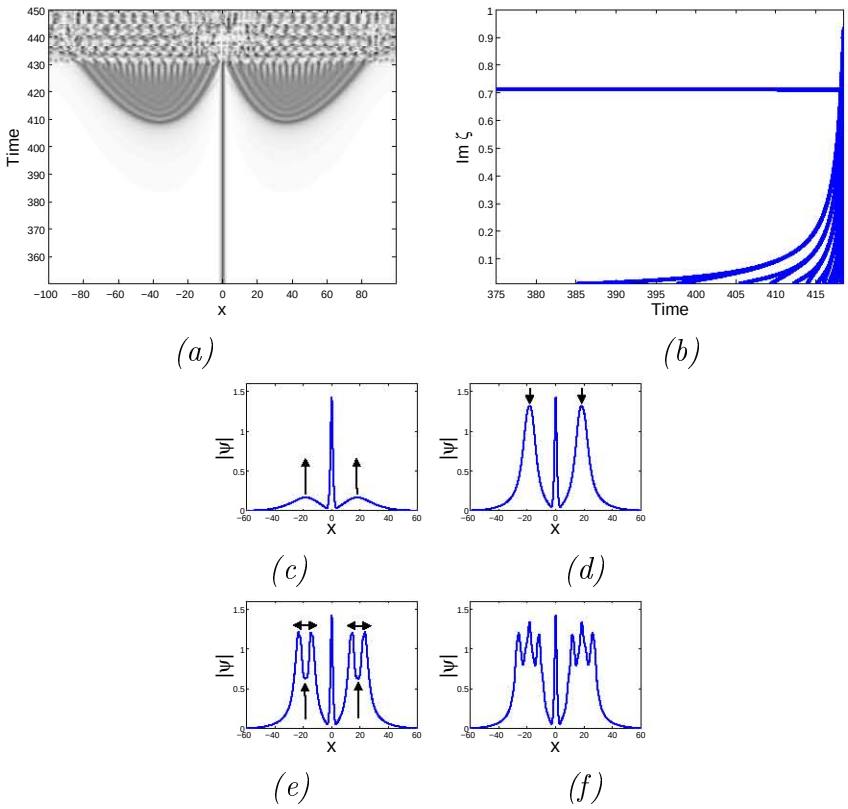

Figure 6.28: *The heteroclinic orbit that arises for* $\gamma = 0.4$ *and* $h = 1.1$ *is shown in (a). In (b) the time evolution of the imaginary parts of the ZS eigenvalues are shown. In (c) - (f) the solution is shown for* $t = 404$, $t = 407$, $t = 407.65$ and $t = 407.78$ *respectively.*

origin. The result is the formation of a solution that satisfies periodic boundary conditions instead of the decaying boundaries on the infinite line, and is therefore irrelevant to our study. In Figure 6.28 (b) we show the time evolution of the imaginary part of the soliton content. In this case all ZS eigenvalues are purely imaginary. The eigenvalue $\zeta \approx 0.7i$ remains constant, reflecting the fact that the soliton transient is non-oscillating, and emits no radiation. At $t = 385$ we see the formation of a second purely imaginary ZS eigenvalue. This eigenvalue increases monotonically with time, and is followed by the formation of numerous other ZS eigenvalues with similar behaviour. In Figure 6.28 (c) – (e) we show the solution at different times to illustrate the formation of additional solitons. In Figure 6.28 (c) we show the solution at $t = 404$. Here we see two lateral waves forming in the tail of the soliton. The amplitudes of these lateral waves grow until $t = 407$, shown in (d). As time evolves beyond this point

the amplitudes of the large lateral waves decrease, leading to the formation of two additional solitons at $t = 407.65$ shown in (e). As time evolves beyond this point the amplitudes of the original lateral waves increase, while the newly-formed solitons move in opposite directions until $t = 407.78$, where three solitons are formed on each side of the original soliton transient.

Discussion

The soliton content of the transients reveal the role of radiation in the formation of chaos. Splitting eigenvalues indicate the emission of large lateral waves. In the small damping regime the ZS eigenvalues remain in the complex plane after splitting. This reflects the fact that the lateral waves are so large that the energy pumped into the system offsets the effect of dissipation, resulting in the formation of solitons. In contrast, ZS eigenvalues remain on the imaginary axis for transients in the no-splitting regime, a regime where the damping coefficient is much larger. This shows that the radiation emitted is much smaller. In this case, instead of single waves changing from lateral waves to solitons, a quiescent radiation tail forms. During each temporal oscillation of the soliton, a small amount of radiation is emitted. Instead of dissipating, the energy of these small radiation waves is added to the radiation tail, resulting in an increase in the energy of the tail. As time evolves, the radiation tail gradually grows until the energy pumped into the system excites the formation of solitons from within these tails. This represents two different mechanisms for the formation of additional solitons that leads to chaos, namely *1)* soliton formation from lateral waves (in the small and single-splitting regimes) and *2)* soliton formation from radiation wave train (double-splitting, no-splitting and large damping regimes).

This leads to the question: what causes these different mechanisms of soliton formation? To answer this question, consider the attractor chart Figure 6.23. There are three boundaries that affect the mechanism of the formation of chaos, namely the Hopf bifurcation boundary that forms the lower boundary of the oscillating soliton attractor region and the upper and lower boundaries of the shaded area. The upper boundary corresponds to the boundary

where the zero solution loses its stability. We refer to this as the unstable zero boundary. The lower boundary of the shaded area represents the onset of the spatio-temporally chaotic regime. That is, for a fixed damping coefficient, the boundary is the smallest driving strength from which the spatio-temporally chaotic attractor emerges. We refer to this as the spatio-temporally chaotic boundary.

From the attractor chart we can see that the spatio-temporally chaotic boundary is sandwiched between the unstable zero boundary and the Hopf bifurcation boundary, provided that $\gamma < 0.378$. From Chapter 5 we know that larger driving strength leads to larger radiation emissions of oscillating soliton attractors. In the previous section we showed that the same applies to soliton transients in the zero attractor region. Therefore a large distance between the Hopf bifurcation boundary and the spatio-temporally chaotic boundary indicates that the transient near the latter boundary emits large radiation, and vice versa. For $\gamma < 0.3$ we see that this distance is large, corresponding to large radiation emissions. This is reflected in the soliton content of the small and single-splitting damping regimes. At $\gamma = 0.3$ the slope of the Hopf bifurcation boundary increases. Although the slope of the spatio-temporally chaotic boundary also increases, it is much smaller than the Hopf bifurcation boundary. However, this increased slope means that the distance between the spatio-temporally chaotic boundary and the zero instability boundary decreases. As this distance becomes smaller, the rate of decay of the harmonics decreases, resulting in a slower rate of dissipation. This accounts for the formation of large radiation tails that are unaffected by dissipation. Therefore the radiation waves that are emitted do not dissipate. The result is that these waves, together with previously emitted radiation waves, form a radiation wave train. Since the radiation waves remain in the tail, smaller radiation waves are required to lead to the formation of spatio-temporal chaos. The fact that smaller radiation waves are emitted is reflected by the fact that no splitting eigenvalues arise in the regime $\gamma > 0.347$.

6.6 Conclusion

The application of the direct scattering study showed that there are four different types of soliton attractors, each with a distinct behaviour of the soliton content. In particular, we showed that side eigenvalues are used to describe a large radiation train, while splitting eigenvalues indicate the formation of large lateral waves. These results were used to reinforce the fact that larger driving strengths lead to larger radiation emissions of the associated oscillating soliton attractor.

We used the direct scattering study to show that the period-doubling bifurcations lead to a faster decrease of the minimum soliton energy associated with an increase in driving strength. The decrease of the minimum soliton energy is associated with the formation of the zero attractor. Therefore the period-doubling bifurcations act as a catalyst for the formation of the zero attractor region.

We showed that oscillating solitons arise as transients in the zero attractor region. Our analysis of the oscillating soliton attractors were used to identify the fact that larger radiation emissions are required to destabilize the solitons when larger driving strengths are applied. This showed that additional energy pumped into the system by means of larger driving strengths counteracts the energy leaked through radiation. Therefore larger radiation emissions are required to destabilize when larger driving strengths are applied. This explains the restabilization of the oscillating soliton attractors in the regime $0.25 \leq \gamma \leq 0.27$.

We also studied the formation of chaos in the spatio-temporally chaotic region. The direct scattering study was used to show the lateral waves play an important role in the formation of chaos in the smaller damping regime, while the radiation tails play an important role in the formation of chaos in the larger damping regime.

Chapter 7

Conclusion

The direct scattering study is a numerical tool for the analysis of soliton dynamics in non-integrable equations. The direct scattering study amounts to the calculation and analysis of the soliton content, defined as the time-dependent discrete spectrum of the associated Zakharov-Shabat (ZS) eigenvalue problem. In particular, our study concentrated on solitons that decay sufficiently fast when $|x| \to \infty$. The effectiveness of the direct scattering study depends on a fast and accurate numerical scheme for the calculation of the soliton content. To develop a fast and accurate numerical scheme, we analyzed the Hill's method, proposed by Deconinck and Kutz [38]. Since Hill's method is developed for periodic boundaries, we analyzed the method for the limit $L \to \infty$. Numerical results show that the solutions can be ambiguous, particularly in the case when discrete eigenvalues are situated near the continuous spectrum. While the results can be improved by increasing the interval length L, the computational cost of this approach is expensive. Our analysis showed that unambiguous solutions can be obtained by choosing an optimal Floquet exponent. The optimal Floquet exponent was obtained numerically, and was shown to converge faster than other choices of the Floquet exponent when the interval length L is increased. Another advantage of the use of the optimal Floquet exponent is that the Hill's method is reduced to a single matrix eigenvalue problem, resulting in a significant improvement in computation cost.

The aim of the thesis is the application of the direct scattering study to analyze solitons of the parametrically driven nonlinear Schrödinger (PDNLS) equation. In order to apply the direct scattering study, one has to generate solitons numerically. We used a fourth-order split-step method to obtain these solutions through direct simulation. We showed that the method is faster than the fourth-order pseudospectral Runge-Kutta method. The basic properties of the numerically-generated attractors were obtained through inspection. In particular, we showed that increased driving strengths lead to solitons with larger magnitudes of oscillations accompanied by emission of larger radiation waves while increased damping coefficients has the opposite effect. We also showed that an increase in driving strength and an increase in damping coefficient results in a decrease of the temporal period of the soliton attractor.

Once these basic properties had been established, we applied the direct scattering study to analyze the oscillating soliton solutions. The purpose of this study was to gain more insight into the behaviour of the soliton and the radiation waves. We classified four different types of attractors, each with a unique behaviour set of the soliton content. These results reflect the characteristics that were reported above. A particularly important result is the so-called *side eigenvalues*, a symmetric set of eigenvalues that appears and disappears on the real line. We demonstrated that these eigenvalues describe wave trains of radiation. We note that this type of eigenvalues was not reported in previous studies of related perturbed NLS equations. These eigenvalues are likely to be overlooked when a shooting method is used. Another important result is that we showed that multiple ZS eigenvalues are formed in the majority of the region of the parameter space where oscillating solitons appear. This limits the use of adiabatic and perturbed inverse scattering studies that assume only a single purely imaginary ZS eigenvalue. This result is in good agreement with the perturbed inverse scattering study performed by Shchesnovich and Barashenkov [91]. Their results accurately described the region where only a single ZS eigenvalue exists. However, in the region where multiple ZS eigenvalues coexist, their analysis was inaccurate.

For smaller damping coefficients, the zero attractor occupies a large area of the attractor

chart. It is well known [25] that an increase in driving strength in this regime results in a period-doubling route to temporally chaotic oscillating soliton attractors. A further increase in driving strength leads to the destabilization of the soliton, resulting in the zero solution to emerge as the only attractor. The direct scattering study showed that, in the oscillating soliton attractor region, an increase in driving strength weakens the minimum soliton energy of the resulting attractor. We analyzed the impact of the period-doubling route to chaos on the minimum soliton energy of oscillating soliton attractors. We showed that the minimum energy of the soliton decreases faster as a result of the period-doubling bifurcations. In other words, the effect of period-doubling is that solitons weakens faster when driving is increased. The result is that the soliton becomes more susceptible to dissipation, leading to the destabilization of the soliton and the zero attractor to arise.

An important result was to show that the oscillating solitons arise as transients in regions of the parameter space where they do not arise as attractors. We analyzed the transient solitons by means of the direct scattering study. The results show that an increase of driving strength in the zero attractor region causes the transient soliton to emit larger radiation waves. The energy lost through radiation destabilizes the soliton, causing it decay to zero. Therefore the emission of larger radiation waves indicates that more radiation energy are required to destabilize the soliton. This implies that increased driving strengths stabilize the transient soliton. Therefore the weakening effect associated with increased driving strengths on solitons (described in the previous paragraph) is counteracted by the stabilizing effect responsible for larger radiation emissions. These results explain the existance of a damping regime where the oscillating soliton attractor *restabilizes* when the driving strength is increased sufficiently.

We also studied the soliton transients that arise in the spatio-temporally chaotic attractor regime. Spatio-temporal chaos is the result of the formation of multiple additional solitons. The direct scattering study showed that radiation plays a vital role in the formation of these additional solitons. We showed that there are different mechanisms involved in the

formation of the chaos. For smaller damping coefficients the additional solitons arises from single radiation waves that are emitted. For large damping coefficients fat radiation tails are formed. These radiation tails are made up of numerous radiation waves that are emitted over a long period of time. The tails are formed due to the fact that the radiation waves no longer decay due to dissipation and the fact that they become quiescent. In this regime the solitons are formed from radiation tails rather than isolated radiation waves.

Future work

The thesis presents two different branches of open questions. The first branch relates to the rigorous analysis of the numerical methods used in the thesis, namely the Hill's method and the split-step method. The second branch is further studies in the PDNLS and related equations. Let's look at each one separately.

The Hill's method is a topic of current research. The problem of convergence is still an open question. While some progress has been made to show convergence for self-adjoint [37] and some classes of nonselfadjoint eigenvalue problems [56], proof of the convergence of the ZS eigenvalue problem related to the NLS equation is still outstanding. We tested our scheme with numerous problems, and the evidence is overwhelmingly in favour of convergence of this problem. A proof of convergence for this problem may lead to more general conditions that ensure convergence of Hill's method. Another line of research is to investigate whether the concept of an optimal Floquet exponent can be extended to more general eigenvalue problems. In terms of the direct scattering study, a useful extension of the Hill's method would be a study of the convergence of the associated eigenfunctions in the $L \to \infty$ limit. If convergence is proven, one can extend the direct scattering study to include the calculation of the normalization coefficients. The normalization coefficients can be used to determine the position of solitons, and also the exact state of the breather. This would be particularly useful for cases where the soliton content consists of more than one ZS eigenvalue. Another

outstanding issue is that of the stability of the split-step method for the PDNLS equation. Our results suggest that the damping may have a stabilizing effect on the split-step scheme.

There are also many open questions in terms of the dynamics of the PDNLS equation. The direct scattering study can be extended to the study of the soliton complexes that were reported. It would be interesting to compare the role of radiation of these complexes with the results we obtained for the oscillating soliton attractors. Another interesting line of research is to study the effect of perturbations, such as higher-order nonlinearities and nonlocal effects, on the oscillating solitons attractors. For perturbations that preserve the stability of the oscillating soliton attractors, it would be interesting to establish the effect of these perturbations on the strength of the soliton and radiation. If perturbations destabilize the oscillating soliton attractors, it would be interesting to test whether oscillating solitons arise as long-term transients. The direct scattering study of these transients may provide some insight into the mechanisms of instability, and the role of radiation in this process.

Bibliography

[1] F.Kh. ABDULLAEV and E.N. TSOY, *The evolution of optical beams in self-focusing media*, Physica D **161**, pp 67-78 (2002)

[2] M.J. ABLOWITZ, B.M. HERBST, C. SCHOBER, *The nonlinear Schrödinger equation: Asymmetric perturbations, travelling waves and chaotic structures*, Journal of Computational Physics **131**, pp 3-12 (1997).

[3] M.J. ABLOWITZ, D.J. KAUP, A.C. NEWELL and H. SEGUR, *Method for solving the sine-Gordon equation*, Physical Review Letters **30**, pp 1262-1264 (1973)

[4] M.J. ABLOWITZ, D.J. KAUP, A.C. NEWELL and H. SEGUR, *The Inverse Scattering Transform-Fourier Analysis for Nonlinear Problems*, Studies in Applied Mathematics **53**, pp 249-315 (1974)

[5] M.J. ABLOWITZ and J.F. LADIK, *Nonlinear differential-difference equations*, Journal of Mathematical Physics **16**, pp 598–603 (1975)

[6] M.J. ABLOWITZ and J.F. LADIK, *On the solution of a class of nonlinear partial difference equations*, Studies in Applied Mathematics **57,** pp 1-12 (1977)

[7] M.J. ABLOWITZ, B. PRINARI and A.D. TRUBATCH, *Discrete and Continuous Nonlinear Schrödinger Systems*, London Mathematical Society Lecture Note Series (2004)

[8] M.J. ABLOWITZ and H. SEGUR, *Solitons and the inverse scattering transform*, SIAM Studies in Applied Mathematics **4**, Philadelphia (1981)

[9] G.P. AGRAWAL, *Nonlinear Fiber Optics*, 3rd Edition, Academic Press, San Diego (2001)

[10] G.B. AIRY, *Tides and waves*, Encyclopedia Metropolitana **5**, pp 241-396 (1845)

[11] N. AKHMEDIEV and A. ANKIEWICZ, *Solitons - Nonlinear pulses and beams*, Optical Quantum Electronics **5**, Chapman & Hall (1997)

[12] N. AKHMEDIEV, J.M. SOTO-CRESPO and G. TOWN, *Pulsating solitons, chaotic solitons, period doubling, and pulse coexistence in mode-locked lasers: CGLE approach*, Physical Review E **63**, 056602 (2001).

[13] N.V. ALEXEEVA and E.V. ZEMLYANAYA, *Breathers in a damped-driven nonlinear Schrödinger equation*, Theoretical and Mathematical Physics **168**, , pp 858-864 (2011)

[14] D. ARTIGAS, L. TORNER, J.P. TORRES and N.N. AKHMEDIEV, *Asymmetrical splitting of higher-order optical solitons induced by quintic nonlinearity*, Optics Communications **143**, pp 322-328 (1997)

[15] I.V. BARASHENKOV, M.M. BOGDAN, and V.I. KOROBOV, *Stability Diagram for the Phase-locked Soliton of the Parametrically Driven, Damped Nonlinear Schrödinger Equation*. Europhysics Letters 1991 **15**, pp 113-118 (1991)

[16] I.V. BARASHENKOV and E.V. ZEMLYANAYA, *Stable Complexes of Parametrically Driven, Damped Nonlinear Schrödinger Solitons*. Physical Review Letters **83**, pp 2568–2571 (1999)

[17] I.V. BARASHENKOV and E.V. ZEMLYANAYA, *Travelling solitons in the damped driven nonlinear Schrödinger equation*, SIAM Journal of Applied Mathematics **64**, pp 800-818 (2004)

[18] I.V. BARASHENKOV and E.V. ZEMLYANAYA, *Soliton complexity in the damped-driven nonlinear Schrödinger equation: Stationary to periodic to quasiperiodic complexes*, Physical Review E **83**, 056610 (2011)

[19] I.V. BARASHENKOV, E.V. ZEMLYANAYA, and M. BÄR, *Travelling solitons in the parametrically driven nonlinear Schrödinger equation*, Physical Review E **64**, 016603 (2001)

[20] I.V. BARASHENKOV, E.V. ZEMLYANAYA and T.C. VAN HEERDEN, *Time-periodic solitons in a damped-driven nonlinear Schrödinger equation*, Physical Review E **83**, 056609 (2011)

[21] T.P. BILLAM, S.L. CORNISH and S.A. GARDINER, *Realizing bright-matter-wave-soliton collisions with controlled relative phase*, Physical Review A **83**, 041602(R) (2011)

[22] G. BOFFETTA and A.R. OSBORNE, *Computation of the Direct Scattering Transform for the Nonlinear Schrödinger Equation*, Journal of Computational Physics **102**, pp. 252-264 (1992)

[23] M. BÖHM and F. MITSCHKE, *Solitons in lossy fibers*, Physical Review A **76**, 063822 (2007)

[24] M BONDILA, *MSc Thesis*, University of Cape Town, unpublished

[25] M. BONDILA, I.V. BARASHENKOV and M.M. BOGDAN, *Topography of Attractors of the Parametrically Driven Nonlinear Schrödinger Equation*, Physica D **87,** pp 314-320 (1995)

[26] A. BÖTTCHER, *Infinite matrices and projection methods*, Lectures on Operator Theory and Its Applications, American Mathematical Society, Providence, RI pp 3-72 (1996)

[27] J. BOUSSINESQ, *Théorie de l'intumescence liquide, applelée onde solitaire ou de translation, se propageant dans un canal rectangulaire*, Comptes Rendus de l'Academie des Sciences **72**, pp 755–759 (1871)

[28] J.P. BOYD, *Chebyshev and Fourier Spectral Methods* (2nd Edition), Dover Publications (2001)

[29] D. BURAK and W. NASALSKI, *Gaussian beam to spatial soliton formation in Kerr media*, Applied Optics **33**, pp. 6393-6401 (1994)

[30] S. BURGER, K. BONGS, S. DETTMER, W. ERTMER, K. SENGSTOCK, A. SANPERA, G.V. SHLYAPNIKOV and M. LEWENSTEIN, *Dark solitons in Bose-Einstein condensates*, Physical Review Letters **85**, pp. 5198-5201 (1999)

[31] A. CALINI and T. IVEY, *Finite-gap solutions of the Vortex Filament Equation: Isoperiodic deformations*, Journal of Nonlinear Science **17**, pp 527-567 (2007)

[32] M.G. CLERC, S. COULIBALY and D LAROZE, *Nonvariational Ising-Bloch transition in parametrically driven systems*, International Journal of Bifurcation and Chaos **19**, pp 2717-2726 (2009)

[33] M.G. CLERC, S. COULIBALY and D LAROZE, *Localized states and non-variational Ising-Bloch transition of a parametrically driven easy-plane ferromagnetic wire*, Physica D **239**, pp 72-86 (2010)

[34] M.G. CLERC, S. COULIBALY and D LAROZE, *Interaction law of 2D localized precession states*, Europhysics Letters **90**, 38005 (2010)

[35] M.G. CLERC, S. COULIBALY and D LAROZE, *Localized waves in a parametrically driven magnetic nanowire*, Europhysics Letters **97**, 30006 (2012)

[36] J.W. COOLEY and J.W. TUKEY, *An algorithm for the machine calculation of complex Fourier series*, Mathematics of Computation **19**, pp 297-301 (1965)

[37] C. CURTIS and B. DECONINCK, *On the convergence of Hill's method*, Mathematics of Computation, **79**, pp 169-187 (2010)

[38] B. DECONINCK and J.N. KUTZ, *Computing spectra of linear operators using the Floquet-Fourier-Hill method*, Journal of Computational Physics **219**, pp 296-321 (2006)

[39] S. DEREVYANKO and E. SMALL, *Nonlinear propagation of an optical speckle field*, Physical Review A **85**, 053816 (2012)

[40] M. DESAIX, D. ANDERSON, L. HELCZYNSKI and M. LISAK, *Eigenvalues of the Zakharov-Shabat Scattering Problem for Real Symmetric Pulses*, Physical Review Letters **90**, 013901 (2003)

[41] I.H. DEUTSCH and I. ABRAM, *Reduction of quantum noise in soliton propagation by phase-sensitive amplification*, Journal of the Optical Society of America B **11**, pp 2303-2313 (1994)

[42] N. DROR and B.A. MALOMED, *Spontaneous symmetry breaking in coupled parametrically driven waveguides*, Physical Review E **79**, 016605 (2009)

[43] E. FERMI, J. PASTA and S. ULAM, *Studies of non linear problems*, Los Alamos, Document LA-1940 (1955)

[44] R. FLESCH, M.G. FOREST and A. SINHA, *Numerical inverse spectral transform for the periodic sine-Gordon equation - theta-function solutions and their linearized stability*, Physica D **48**, pp 169-231 (1991)

[45] E. FOREST and R. RUTH, *Fourth order symplectic integration*, Physica D **43**, pp 105-117 (1990)

[46] C.S. GARDNER, J.M. GREENE, M.D. KRUSKAL and R.M. MIURA, *Method for solving the Korteweg-de Vries equation,* Physical Review Letters **19**, pp 1905-1097 (1967)

[47] R.A. GARDNER, *Spectral analysis of long wavelength periodic waves and applications*, Journal fur die Reine und Angewandte Mathematik, **491**, pp 149-181 (1997)

[48] M. GÖLLES, I.M. UZUNOV and F. LEDERER, *Break up of N-soliton bound states due to intrapulse Raman scattering and third-order dispersion – an eigenvalue analysis*, Physics Letters A **231**, pp 195-200 (1997)

[49] R. H. HARDIN and F. D. TAPPERT, *Applications of the split-step Fourier method to the numerical solution of nonlinear and variable coefficient wave equations*, SIAM review **15**, pp 423. (1973)

[50] B.M. HERBST, M.J. ABLOWITZ and E. RYAN, *Numerical homoclinic instabilities and the complex modified Korteweg-de Vries equation*, Computer Physics Communications **65**, pp 137-142 (1991)

[51] R. HIROTA, *Exact solution of the Korteweg-de Vries equation for multiple collisions of solitons*, Physical Review Letters **27**, pp 1192-1194 (1971)

[52] R. HIROTA, *Exact solution of the modified Korteweg-de Vries equation for multiple collisions of solitons*, Journal of the Physical Society of Japan **33**, pp1456-1458 (1972)

[53] R. HIROTA, *Exact solution of the sine-Gordon equation for multiple collisions of solitons*, Journal of Physical Society of Japan **33**, pp 1459-1463 (1972)

[54] R. HIROTA, *Exact envelope-soliton solutions of a nonlinear wave equation*, Journal of Mathematical Physics **14**, pp 805-809 (1973)

[55] T. IVEY and S. LAFORTUNE, *Spectral stability analysis for periodic travelling wave solutions of NLS and CGL perturbations*, Physica D **237**, pp. 1750-1772 (2008)

[56] M. JOHNSON and K. ZUMBRUN, *Convergence of Hill's method for nonselfadjoint operators*, SIAM Journal of Numerical Analysis **50**, pp 64-78 (2012)

[57] D.J. KAUP, *A perturbation expansion for the Zakharov-Shabat inverse scattering transfrom*, SIAM Journal of Applied Mathematics **31**, pp121-133 (1976)

[58] D.J. KAUP and A.C. NEWELL, *Theory of nonlinear oscillating dipolar excitations in one-dimensional condensates*, Physical Review B **18**, pp. 5162-5167 (1978)

[59] E. KENIG, B.A. MALOMED, M.C. CROSS and R. LIFSHITZ, *Intrinsic localized modes in parametrically driven arrays of nonlinear resonators*, Physical Review E **80**, 046202 (2009)

[60] Y.S. KIVSHAR and B.A. MALOMED, *Dynamics of solitons in nearly integrable systems*, Review of Modern Physics **61**, pp 763-915 (1989)

[61] M. KLAUS and J.K. SHAW, *Influence of pulse shape and frequency chirp on stability of optical solitons*, Optics Communications **197**, pp 491-500 (2001)

[62] M. KLAUS and J.K. SHAW, *Purely imaginary eigenvalues of Zakharov-Shabat systems*, Physical Review E **65**, 036607 (2002)

[63] D.J. KORTEWEG and G. DE VRIES, *On the change of form of long waves advancing in a rectangular channel, and on a new type of long stationary waves*, Philosophical Magazine (Series 5) **39**, pp 442-443 (1895)

[64] P.D. LAX, *Periodic solutions of the KdV equation*, Communications on Pure and Applied Mathematics **28**, pp. 141-188 (1975)

[65] P.D. LAX, *Integrals of nonlinear equations of evolution and solitary waves*, Communications in Pure and Applied Mathematics **21**, pp 467-490 (1968)

[66] S. LONGHI, *Ultrashort-pulse generation in degenerate optical parametric oscillators*, Optics Letters **20**, pp 695-697 (1995)

[67] Y.C. MA and M.J. ABLOWITZ, *The periodic cubic Schrödinger equation*, Studies in Applied Mathematics **65**, pp113-158 (1981)

[68] W. MAGNUS, and S. WINKLER, *Hill's equation*, Corrected republication of the 1966 Edition, New York: Dover, (1979)

[69] B.A. MALOMED, *Emission from, quasi-classical quantization, and stochastic decay of sine-Gordon solitons in external fields*, Physica D **27**, pp 113-157 (1987)

[70] S.V. MANAKOV, *On the theory of two-dimensional stationary self-focussing of electromagnetic waves*, Soviet Physics JETP **38**, pp 248-253 (1974)

[71] V.B. MATVEEV and M.A. SALLE, *Darboux Transformations and Solitons*, Springer Series in Nonlinear Dynamics (Springer, 1990).

[72] A. MECOZZI, W.L. KATH, P. KUMAR and C.G. GOEDDE, *Long-term storage of a soliton bit stream by use of phase-sensitive amplification*, Optics Letters **19**, pp 2050-2052 (1994)

[73] M. MIDRIO, M. ROMAGNOLI, S. WABNITZ and P. FRANCO, *Relaxation of guiding center solitons in optical fibers*, Optics Letters **21**, pp. 1351-1353 (1996)

[74] J.W. MILES, *Nonlinear Faraday resonance*, Journal of Fluid Mechanics **146**, pp 285-302 (1984)

[75] J.W. MILES, *Parametrically excited solitary waves*, Journal of Fluid Mechanics **148**, pp. 451-460 (1984)

[76] R.O. MOORE and K. PROMISLOW, *Renormalization group reduction of pulse dynamics in thermally loaded optical parametric oscillators*, Physica D **206**, pp 62-81 (2005)

[77] G.M. MUSLU and H.A. ERBAY, *Higher-order split-step Fourier schemes for the generalized nonlinear Schrödinger equation*, Mathematics and Computers in Simulation **67**, pp 581-595 (2005)

[78] F. NERI, *Lie algebras and canonical integration*, Preprint, Department of Physics, University of Maryland (1988)

[79] G. NEUGEBAUER and R. MEINEL, *General N-soliton solution of the AKNS class on arbitrary backgrounds*, Physics Letters A **100**, pp 467-470 (1984)

[80] S.P. NOVIKOV, S.V. MANAKOV, L.P. PITAEVSKII, V.E. ZAKHAROV, Theory of Solitons: The Inverse Scattering Method, Springer-Verlag (1984), ISBN 0-306-10977-8

[81] C.P. OLIVIER, B.M. HERBST and M.A. MOLCHAN, *A numerical study of the large-period limit of a Zakharov-Shabat eigenvalue problem with periodic potentials*, Journal of Physics A: Mathematical and Theoretical **45**, pp 255205 (2012)

[82] E.A. OVERMAN, D.W. MCLAUGHLIN, and A.R. BISHOP, *Coherence and chaos in the driven damped sine-Gordon equation: Measurement of the soliton spectrum*, Physica D **19**, pp 1-41 (1986)

[83] N.-C PANOIU, I.V. MEL'NIKOV, D. MIHALACHE and F. LEDERER, *Soliton generation from a multi-frequency optical signal*, Journal of Optics B-Quantum and Semiclassical Optics **4**, R53-R68 (2002)

[84] N.-C PANOIU, D. MIHALACHE, D. MAZILU, I.V. MEL'NIKOV, J.S. AITCHISON, F. LEDERER and R.M. OSGOOD JR., *Dynamics of dual-frequency solitons under the influence of frequency-sliding filters, third-order dispersion, and intrapulse Raman scattering*, IEEE Journal of Selected Topics in Quantum Electronics **10**, pp 885-892 (2004)

[85] J.E. PRILEPSKY and S.A. DEREVYANKO, *Breakup of a multisoliton state of the linearly damped nonlinear Schrödinger equation*, Physical Review E **75**, 036616 (2007)

[86] K. PROMISLOW and J.N. KUTZ, *Bifurcation and asymptotic stability in the large detuning limit of the optical parametric oscillator*, Nonlinearity **13**, pp 675-698 (2000)

[87] LORD RAYLEIGH, *On waves*, Philosophical Magazine (Series 5) **1**, pp 257-279 (1876)

[88] J.S. RUSSELL, *Report on waves*, Report of the 14th Meeting of the British Association for the Advancement in Science, pp 311-390 (1844)

[89] V.J. SÁNCHEZ-MORCILLO, I. PÉREZ-ARJONA, F. SILVA, G.J. DE VALCÁRCEL and E ROLDÁN, *Vectorial Kerr-cavity solitons*, Optics Letters **25**, pp 957-959 (2000)

[90] J. SATSUMA and N. YAJIMA, *Initial value problems of one-dimensional self-modulation of nonlinear waves in dispersive media*, Supplement of the Progress of Theoretical Physics **55**, pp 284-306 (1974)

[91] V.S. SHCHESNOVICH and I.V. BARASHENKOV, *Soliton-Radiation Coupling in the Parametrically Driven Damped Nonlinear Schrödinger Solitons*, Physica D **164**, pp 83-109 (2002)

[92] K. STALIUNAS, *Transverse pattern formation in optical parametric oscillators*, Journal of Modern Optics **42**, pp 1261-1269 (1995)

[93] G.G. STOKES, *On the theory of oscillatory waves*, Transactions of the Cambridge Philosophical Society **8**, pp 441-455 (1847)

[94] A. SURYANTO and E. VAN GROESEN, *Self-splitting of multisoliton bound states in planar Kerr waveguides*, Optics Communications **258**, pp 264-274 (2006)

[95] M. SYAFWAN, H. SUSANTO and S.M. COX, *Discrete solitons in electromechanical resonators*, Physical Review E **81**, 026207 (2010)

[96] T.R. TAHA and M.J. ABLOWITZ, *Analytical and numerical aspects of certain nonlinear evolution equations. I. Analytical*, Journal of Computational Physics **55**, pp 192–202 (1984)

[97] LLOYD N. TREFETHEN, *Spectral methods in MatLab*, Society for Industrial and Applied Mathematics, Philadelphia, PA, (2000)

[98] E.N. TSOY and C.M. DE STERKE, *Oscillations of the soliton parameters in nonlinear interference phenomena*, Physics Letters A **372**, pp 1856-1861 (2008)

[99] D. URZAGASTI, D. LAROZE, M.G. CLERC, S. COULIBALY and H. PLEINER, *Two-soliton precession state in a parametrically driven magnetic wire*, Journal of Applied Physics **111**, 07D111

[100] S. WABNITZ and E. WESTIN, *Optical fiber soliton bound states and interaction suppression with high-order filtering*, Optics Letters **21**, pp 1235-1237 (1996)

[101] M. WADATI, *The exact solution of the modified Korteweg-de Vries equation*, Journal of the Physical Society in Japan **32**, pp 1681–1687 (1972)

[102] X. WANG, *Boundary effect on a parametrically excited soliton*, Journal of the Accoustical Society of America **104**, pp 715-721 (1998)

[103] X. WANG, *Internal dynamics of the parametrically excited bound state of double solitary-waves*, Physica D **127**, pp 13-32 (1999)

[104] W. WANG, X. WANG, J. WANG and R WEI, *Dynamical behavior of parametrically excited solitary waves in Faraday's water trough experiment*, Physics Letters A **219**, pp 74-78 (1996)

[105] X. WANG and R. WEI, *Synchronous spatiotemporal oscillation between two parametrically excited bound states*, Chinese Physics Letters **15**, pp 275-277 (1998)

[106] X. WANG and R. WEI, *Oscillatory patterns composed of the parametrically excited surface-wave solitons*, Physical Review E **57**, pp 2405-2410 (1998)

[107] J.A.C. WEIDEMAN and B.M. HERBST, *Split-step methods for the solution of the nonlinear Schrödinger equation*, SIAM Journal of Numerical Analysis **23**, pp 485-507 (1986)

[108] J. WU, R. KEOLIAN and I. RUDNICK, *Observation of a nonpropagating hydrodynamic soliton*, Physical Review Letters **52**, pp. 1421-1424 (1984)

[109] J. YANG, *Nonlinear Waves in Integrable and Nonintegrable Systems*, SIAM Mathematical Modeling and Computation, (2010)

[110] H. YOSHIDA, *Construction of higher order symplectic integrators*, Physical Letters A **150**, pp 262-268 (1990)

[111] N.J. ZABUSKY and M.D. KRUSKAL, *Interaction of solitons in a collisionless plasma and the recurrence of initial states*, Physical Review Letters **15**, pp 240-243 (1965)

[112] V.E. ZAKHAROV, V.S. L'VOV and S.S. STAROBINETS, *Spin-wave turbulence beyond the parametric excitation threshold*, Uspekhi Fizicheskikh Nauk **114**, pp 609-654 (1974)

[113] V.E. ZAKHAROV and A.B. SHABAT, *Exact theory of two-dimensional self-focusing and one-dimensional self modulation of waves in nonlinear media*, Soviet Physics Journal of Experimental and Theoretical Physics **34**, pp 62-69 (1972)

[114] E.V. ZEMLYANAYA and N.V. ALEXEEVA, *Oscillating solitons of the driven, damped nonlinear Schrödinger equation*, Theoretical and Mathematical Physics **159**, pp 870-876 (2009)

[115] L. ZHANG, X. WANG and Z. TAO, *Spatiotemporal bifurcations of a parametrically excited solitary wave*, Physical Review E **75**, 036602 (2007)